STUDY ON PROPERTIES OF SILVER NIOBATES AND TANTALATES PREPARED BY SOFT CHEMICAL PROCESSES

A Dissertation

Submitted to

Interdisiplinary Graduate School of Medical, Engineering and Agricultural Sciences

University of Yamanashi

In Partial Fulfillment

of the Requirements for the Degree of

DOCTOR OF PHILOSOPHY

---

by

W. Isuru Udakara Withanage

March 2021

Approved by supervising committee:

Supervisor: Professor Nobuhiro Kumada

ABSTRACT

In the modern information age, material science has become a major field for probing, processing and synthesizing novel materials, utilizing limited resources available on earth. In the next century demand for materials will only continue to rise and the need to transition towards environmental friendly, earth abundant, cheap sources would be of paramount importance. This thesis work was primarily focused on design, adaptation and understanding of the crystal structures of the niobate and tantalate compounds, particularly silver ion-exchanged pyrochlore-type niobate and tantalate compounds as photocatalytic materials for the conversion of renewable energy in water purification. This investigation was accomplished by combining hydrothermal synthesis, state of the art characterization and exploring the application of the newly synthesized materials. We hypothesized that it would be possible to improve the photocatalytic activity by engineering K_2O-Nb_2O_5/Ta_2O_5-H_2O hydrothermal systems. We also hypothesized that the pyrochlore-structure would serve as an applicable material in the fields of photocatalysis, antibacterial activity and ionic conductivity.

Initially the crystal structures of K_2O-Nb_2O_5-H_2O hydrothermal system was investigated by adjusting the ratio of the starting materials, pH of the reaction system, time and temperature of the reaction. Experimental results showed successful synthesis of pyrochlore-, perovskite- and layered-type structures. However, the pyrochlore-type compound did not exhibit good photocatalytic activity.

In order to improve the photocatalytic activity of the pyrochlore structure, we used an ion-exchange technique to synthesize pyrochlore–type silver tantalate and fluorite-type silver niobate structures. Their crystal structures were refined by the Rietveld method using synchrotron X-ray powder diffraction and pyrochlore-type silver tantalate showed photocatalytic activity towards phenol degradation under UV light irradiation. The silver incorporated compounds were good ionic conductors. Thus, ionic conductivity of pyrochlore–type silver tantalate and fluorite-type silver niobates were evaluated from 25 to 240 °C. At 240 °C, the total conductivities (ionic + electric) of silver tantalate and niobate reached 4.00×10^{13} and 9.03×10^{14} S/cm, respectively. The activation energy of silver tantalate was 0.61 eV and silver niobate showed non-linear

behavior with activation energies of 0.52 eV at temperatures less than 120 °C and 0.33 eV at temperatures greater than 120 °C.

In a third study, the tunnel structure of the pyrochlore phase, silver ions were engineered by ion-exchange with different molar ratios to evaluate the antibacterial activity. The antibacterial efficacy of these samples were investigated by colony count method and relative antibacterial activity was compared based on the diameter of the inhibition zone. The results indicate that silver ion exchanged samples with molar ratios of Ag/Nb = 0.05 [KAN1], 0.44 [KAN2], 0.67 [KAN3] and Ag/Ta = 0.07 [KAT1], 0.44 [KAT2], 0.64 [KAT3] irrespectively exhibited complete (100%) antibacterial activity against *Staphylococcus aureus* (*S. aureus*, gram-positive) and *Escherichia coli* (*E. coli*, gram-negative). Among these, KAN1 and KAT1 exhibited the highest antibacterial activities due to the control release of the Ag^+ ion through their tunnel structures. In this study we established that the tunable antibacterial properties of pyrochlore-type niobate and tantalate compounds enabled the optimal discharge of Ag^+, which inhibitted the bacterial efficacy in different capacities leading to various biomedical applications.

In this thesis work, we evaluated the photocatalytic, antibacterial and electrical properties of niobate and tantalate compounds. We observed very good photocatalytic activity for silver tantalate towards phenol degradation. Antibacterial activity tests suggest that an enhancement of controllable antibacterial properties from three different ion-exchanged compounds. Vast applications and energy efficient synthesis of these niobate and tantalate materials is an attractive solution for the realization of functional materials in future green technologies.

DEDICATION

This dissertation is wholeheartedly dedicated to loving parents.

For without your vision, none of my success would be possible.

ACKNOWLEDGMENTS

First and foremost, I would like to extend my sincere gratitude to the most amazing PhD supervisor, Prof. Nobuhiro Kumada. His unwavering support during the last five years at graduate school made this arduous journey pleasant and motivation that kept me moving towards research goals. The constant guidance and discussions with Prof. Kumada are what made this thesis work of quality and candor. I would also like to extend my heartfelt gratitude to my close collaborators: Prof. Takahiro Takei and Dr. Sayaka Yanagida for their invaluable guidance during the research work.

I make this the opportunity to thank collaborators at Kiyoharu Tadanaga group in Hokkaido University, Masaki Azuma group in Tokyo institute of Technology and Aizawa Mamoru group in Meiji University for providing experimental facilities and their precious advices. And also special thanks goes to Prof. Yoshihiro Kuroiwa and Prof. Chikako Moriyoshi form the Hiroshima University for their great help during the SPring-8 experiments.

I thank past Kumada-Takei group members: Dr. Md Saiduzzaman, Dr. Goushen Yang, Dr. Puthri Rizka Lestari and my tutor Mr. Yo Yamamoto for their

support in training me in instrumentation, laboratory practices and moreover providing me with a great friendly atmosphere to work in. I should also thank all student who studied in my group and our research center since 2016 to the present for engaging in great intellectual discussions to make my research productive.

I would also like to thank for my family, living thousands of miles away, they always made time to lookout for me through thick and thin times during my time at graduate school. My parents (W. Danapala and G.I. Janaranjani) and younger brothers (W.G. Darshana and W.D. Kavishalya) have always been the cheer leaders. I am especially grateful to my wife Sulasa Ariyapala for her enthusiastic support and inspiration. I also really want to thanks my colleagues, friends and especially my best friend Dr. Nuwan Harsha Attanayake.

I would like to express my sincere gratitude all professors and researchers at Center for Crystal Science and Technology (CCST) and Green Energy Program. Finally, I would like to acknowledge special doctoral program for green energy conversation science and technology at University of Yamanashi and Power Energy Professionals (PEP) at Waseda University for the financial support, without funding none of this would have been possible.

TABLE OF CONTENTS

Page

ABSTRACT.....iii

DEDICATION.....vii

ACKNOWLEDGMENTS.....viii

LIST OF TABLES.....xv

LIST OF FIGURES.....xvi

CHAPTERS

1. INTRODUCTION.....1

1.1 Overview.....1

1.2 Hydrothermal synthesis.....5

1.3 Hydrothermal synthesis of niobate and tantalate compounds

.....10

1.4 Thesis Goals and Outline.....12

1.5 References.....18

2. EXPERIMENTAL TECHNIQUES.....25

2.1 Materials and product characterization techniques.....25

2.1.1 Synchrotron radiation X- ray Diffraction (SXRD) 25

2.1.2 X-ray Diffraction (XRD) 28

2.1.3 Scanning Electron Microscopy (SEM) 29

2.1.4 X-Ray Photoelectron Spectroscopy (XPS) 30

2.1.5 High Performance Liquid Chromatography (HPLC) 32

2.2 Photocatalytic, Antibacterial and Ionic conductivity test 33

2.2.1 Photocatalytic activity analysis by phenol degradation 33

2.2.2 Antibacterial tests 34

2.2.3 Ionic conductivity test 38

2.3 References 39

3. HYDROTHERMAL DOPING OF Ag INTO THREE TYPES OF POTASSIUM NIOBATES. 41

3.1 Introduction 41

3.2 Experimental Section 42

3.2.1 Materials and Methods 42

3.2.2 Morphological and composition Characterization 43

3.3 Results and Discussion 44

3.3.1 Hydrothermal synthesis 44

3.3.2 EXAFS analysis 46

3.3.3 Photocatalytic activity 49

3.4 Conclusions 51

3.5 References 52

4. SYNTHESIS, CRYSTAL STRUCTURE AND ELECTRICAL PROPERTIES OF PYROCHLORE-TYPE SILVER TANTALATE AND FLUORITE-TYPE SILVER NIOBATE 55

4.1 Introduction 55

4.2 Experimental Section 57

4.2.1 Materials and Methods 57

4.2.2 Morphological and composition Characterization 58

4.3 Results and Discussion 59

4.3.1 Material characterization 59

4.3.2 Photocatalytic activity 63

4.4 Total conductivity of silver tanatalate (AT) and silver niobate (AN) 65

4.4 Conclusion 69

4.5 References 70

5. ANTIBACTERIAL PROPERTIESE OF SILVER NIOBATES AND TANTALATES 73

5.1 Introduction 73

5.2 Experimental Section 75

5.3.1 Materials characterization 75

5.3 Results and Discussion 77

5.3.1 Structure 77

5.3.2 UV –vis spectra and XPS analysis 79

5.3.3 Antimicrobial properties 82

5.4 Conclusion 89

5.5 References 90

6. ANTIMICROBIAL PROPERTIES OF PEROVSKITE TYPE $Ag/KNbO_3$ COMPOUND PREPARED BY ONE-POT HYDROTHERMAL PROCESS 94

6.1 Introduction 94

6.2 Experimental Section 96

6.2.1 Materials and characterization 96

6.3 Results and Discussion 98

6.3.1 Antibacterial properties 102

6.4 Conclusion 105

6.5 References 105

7. BRIEF SUMMARY AND RESEARCH IMPACT 109

8. BUSINESS SENSE AND SOCIAL AWARENESS 113

8.1 References 119

LIST OF PUBLICATIONS 121

LIST OF TABLES

Table Page

4.1 Crystallographic data and atomic parameters of $Ag_{0.41}Nb_{0.59}O_{1.68}$. 63

4.2 Crystallographic data and atomic parameters of $Ag_{0.93}TaO_{2.96}\cdot 0.94H_2O$. 63

5.1 Colony forming units of antibacterial test on niobate and tantalate. 83

LIST OF FIGURES

Figure Page

1.1 Synthesis method of ceramic materials from liquid phase. 4

1.2 Schematic diagram of hydrothermal method equipment. 7

1.3 General steps of hydrothermal preparation. 7

1.4 Phase diagram of water 8

1.5 Variation of dielectric constant of water with temperature and pressure.. 9

1.6 Crystal structure of various niobate and tantalates (a) $A_2B_2O_7$ with pyrochlore-type (b) ABO_3 with perovskite type and (c) $A_4B_6O_{17}.xH_2O$ with layered-type.. 11

1.7 Schematic description of material science.. 12

1.8 Schematic diagram of organic compounds degradation.. 14

1.9 Schematic mechanisms for antibacterial behaviors of silver nanoparticles.. 16

2.1 The Spring -8 third generation synchrotron radiation source. 26

2.2 Schematic describing of Braggs Law..... 28

2.3 Illustration of the different types of signals used in SEM, and their origins in the specimen. 29

2.4 Schematic diagram showing the X-ray source, specimen and the electron energy analyzer in a X-ray photoelectron spectrophotometer.. 30

2.5 Schematic diagram showing the pump, sample inject, column, detector and data system in HPLC instrument. 32

2.6 Schematic diagram showing the photocatalytic phenol degradation. 33

2.7 Schematic representation of colony counting method 35

2.8 Schematic representation of Inhibition zone method..... 37

2.9 Schematic representation of impedance measurement 38

3.1 K_2O-Nb_2O_5-H_2O hydrothermal system..... 43

3.2 XRD patterns of (a) layered-type $K_4Nb_6O_{17}\cdot nH_2O$:Ag (b) pyrochlore-type $(K_{0.73}H_{0.27})NbO_3\cdot 1.72H_2O$: Ag (c) perovskite-type, $KNbO_3$:Ag..... 45

3.3 SEM images of (a) layered $K_4Nb_6O_{17}\cdot nH_2O$:Ag (b) pyrochlore-type $(K_{0.73}H_{0.27})NbO_3\cdot 1.72H_2O$: Ag (c) perovskite-type, $KNbO_3$:Ag.. . 46

3.4 Ag K-edge XANE spectra of layered-, pyrochlore-, perovskite samples with reference Ag_2O and Ag-foil.. 47

3.5 Radial distribution function of layered, pyrochlore, and perovskite samples with reference Ag_2O and Ag-foil. 47

3.6 (I) Uv-vis absorption spectra and (II) Tauc plot of (a) layered, (b) pyrochlore and (c) perovskite samples..... 50

3.7 Photocatalytic activity of (a, pink) layered, (b, black) pyrochlore and (c, red) perovskite samples. Solid and dash line denoted Ag doped and undoped samples respectively. 50

4.1 K_2O-Nb_2O_5-H_2O hydrothermal system. 55

4.2 SEM photograph of (a) $(K_{0.73}H_{0.27})NbO_3 \cdot 0.83H_2O$, (b)$Ag_{0.41}Nb_{0.59}O_{1.68}$ (c) $(K_{0.56}H_{0.44})TaO_3 \cdot 1.14H_2O$ and (d) $Ag_{0.93}TaO_{2.97} \cdot 0.94H_2O$. 60

4.3 Rietveld refinement pattern of the synchrotron powder diffraction data for (a) $Ag_{0.41}Nb_{0.59}O_{1.68}$ and (b) $Ag_{0.93}TaO_{2.97} \cdot 0.94H_2O$ 61

4.4 Uv-vis absorption spectra (a) and Tauc plot for the estimation (b) for $(K_{0.73}\ H_{0.27})\ NbO_3 \cdot 0.83H_2O$, $(K_{0.56}H_{0.44})TaO_3 \cdot 1.14H_2O$, $Ag_{0.41}Nb_{0.59}O_{1.68}$, and $(K_{0.73}\ H_{0.27})\ NbO_3 \cdot 0.83H_2O$. 64

4.5 Photocatalytic activity of $(K_{0.73}H_{0.27})NbO_3 \cdot 1.72H_2O$, $(K_{0.56}H_{0.44})TaO_3 \cdot 1.14H_2O$, $Ag_{0.41}Nb_{0.59}O_{1.68}$, and $Ag_{0.93}TaO_{2.97} \cdot 0.94H_2O$. 65

4.6 Nyquist plot of (a) AT (b) AN. 66

4.7 Arrhenius plot of (a) AT (b) AN (c) Rb^+ in pyrochlore structure and (d) K^+ in pyrochlore structure. 68

5.1 Schematic diagram of the bacterial cell 74

5.2 XRD pattern of parent and silver ion-exchange niobate and tantalate compounds 77

5.3 SEM image of (a)KN, (b)KAN1, (c)KAN2, (d)KAN3, (e)KT, (f) KAT1, (g)KAT2 and (h)KAT3. 79

5.4 Tauc plot of (a) KN and its ion exchanged products and (b) KT and its ion exchanged products. 80

5.5 XPS spectra of the silver ion-exchanged niobate and tantalate (a-f) Ag 3d region 81

5.6 Qualitative antibacterial evaluation of control, KN, KT and silver ion-exchange samples against (a) *Escherichia coli* (b) *Staphylococcus aureus* after 24 h incubation..... 82

5.7 Comparison of the inhibition zone between KN, KT silver ion-exchange samples against (a) *Escherichia coli* (b) *Staphylococcus aureus* after 48 h incubation. 84

5.8 (a) The relative inhibition zone of each samples against *Escherichia coli* and *Staphylococcus aureus* after 48 h incubation (b) Release Ag^+ and K^+ ion from niobate and tantalate samples pellet after 48 hours. 85

5.9 Schematic representation of antibacterial mechanism by pyrochlore-type structure. 86

5.10 (a) UV-Vis absorbance spectra of Ag^+ released solution after 48 hours and (b) magnified graph.. 88

6.1 K_2O-Nb_2O_5-H_2O hydrothermal system. 94

6.2 XRD pattern of parent and silver loaded samples..... 98

6.3 Rietveld refinement pattern and structure of the $KNbO_3$..... 99

6.4 SEM image of (a)KN, (b) AKN1, (c) AKN2, (d) AKN3. 100

6.5 (a) Uv-Vis DR spectra of KN, KAN1, KAN2 and KAN3; the insert is band gap calculation by (b) Tauc plot. 100

6.6 XPS spectra of the KAN3 Ag 3d region. 102

6.7 Comparison of the inhibition zone between perovskite-type Ag@$KNbO_3$ samples against (a) *Escherichia coli* (b) *Staphylococcus aureus* after 48 h incubation..... 103

6.8 (a) Release Ag^+ ion from Ag@$KNbO_3$ samples after 48 hours and (b) relative inhibition zone of the samples against *Escherichia coli* and *Staphylococcus aureus*.. 104

8.1 Crystal structure of $KHSi_2O_5$ and its ion-exchanged product $AgHSi_2O_5$. 114

8.2 Schematic illustration of $AgHSi_2O_5$ / CF filter paper preparation. 115

8.3 Schematic illustration of structure and filtration process of the prepared $AgHSi_2O_5$ / CF filter paper. 118

8.4 Schematic illustration of home-made filtration device. 119

CHAPTER 1

INTRODUCTION

1.1 Overview

One of the greatest challenges facing humanity in the 21st century is the realization of novel energy harvesting solid materials which are environmental friendly, low cost as well as applicable for various essential applications[1,2]. The fast growth in advance technology and the quality of life have create an urgent to produce new materials with the limited resources available on the earth. The first materials utilized and synthesized by mankind begins with the Stone Age. The typically materials used included flint, stone along with animal materials, shells, bone, clay and wood[3]. The next development of civilization with Bronze Age, Iron Age expanded and conquered more advance material processing techniques[4]. Then the Romans were discovered that mixture of volcanic ash and powder limestone reacts with water to form a hard solid cement paste which was the first low temperature inorganic technology[5]. This cement, ceramic, rock and metal technology were dominated until the early years of this century. The material science became a major field in silicon age after the discovery of X-ray crystallography (Bragg diffraction) by William Henry Bragg and his son William Lawrence Bragg in 1913[6]. The Bragg

law demonstrate the existence of real atomic arrangement and this new tool allowed the investigation of crystal as well as solid materials for the Information Age. The information age correlated with the invention of the transistors, particularly MOSFET (metal-oxide-semiconductors field-effect transistor) which became a building block for transformation of modern technology[7]. This led to revolutionize the modern computers and mobile phones which helped the development of laser technology, light emitting diodes and fiber optic communications.

In a global perspective the material demand will only continue to rise into the next century, and the need transition towards environmental friendly, earth abandoned, cheap sources are of paramount importance. To meet this challenge the scientific community has been active in identifying, developing, designing and synthesizing novel inorganic and organic materials concerning current material science and solid state chemistry[8]. The materials science and solid-state chemistry is the study of the relation between the coordination, atomic level microstructure and the applications of the materials. Also, material scientist must consider developing other criteria such as high yield efficient processes with low energy consumption as well as pure products from inexpensive, environmental friendly starting materials.

The current global raw and process material requirement is predicted to reach an unprecedented place with the rapid growth of population and expanding industrialization. Moreover, new material synthesis as well as processing need large quantity of carbon based energy and it releases large quantities of the greenhouse gas CO_2, which is one of the major atmospheric gases that is related to climate change[9]. The most practical solution is to shift towards environmentally benevolent synthesis methods and harvesting energy from renewable sources such as wind, hydroelectricity, and solar to create carbon neutral economies[10,11].

Nowadays various solid, liquid and gas process have been used in sample synthesis such as sol-gel, chemical vapor deposition, hydrothermal, co-precipitation, electrochemical, ball milling, solid state method, physical vapor deposition, and lithography[12–16]. Even though solid phase synthesis provide high yield and large scale production, it is difficult to control morphology, particle size and impurity levels. In the case of gas phase method, it generally involves the chemical vapor reaction and evaporation and condensation method. These methods yield small particle with high purity and high surface activity, but this reaction process needs large amount of solvents and high technological equipment, as well as it is difficult to produce at a large scale[17]. The liquid phase synthesis mostly involve with

solvothermal, sol-gel, colloidal, and precipitation methods[18–21]. Among these various synthesis processes (solid, liquid, gas), hydrothermal method is easy, low energy consumption, environmentally friendly process and moreover, this method can control particle size, shape and impurities. The Figure 1.1 presents the summary of the most important liquid phase method and ceramic materials that have been prepared. Thus, hydrothermal method can be used to synthesize oxides, hydroxides, carbonates and silicates materials which lead to various potential application in daily life. In this research we focused to the synthesis of new pyrochlore-type alkali niobates and tantalates by hydrothermal reactions.

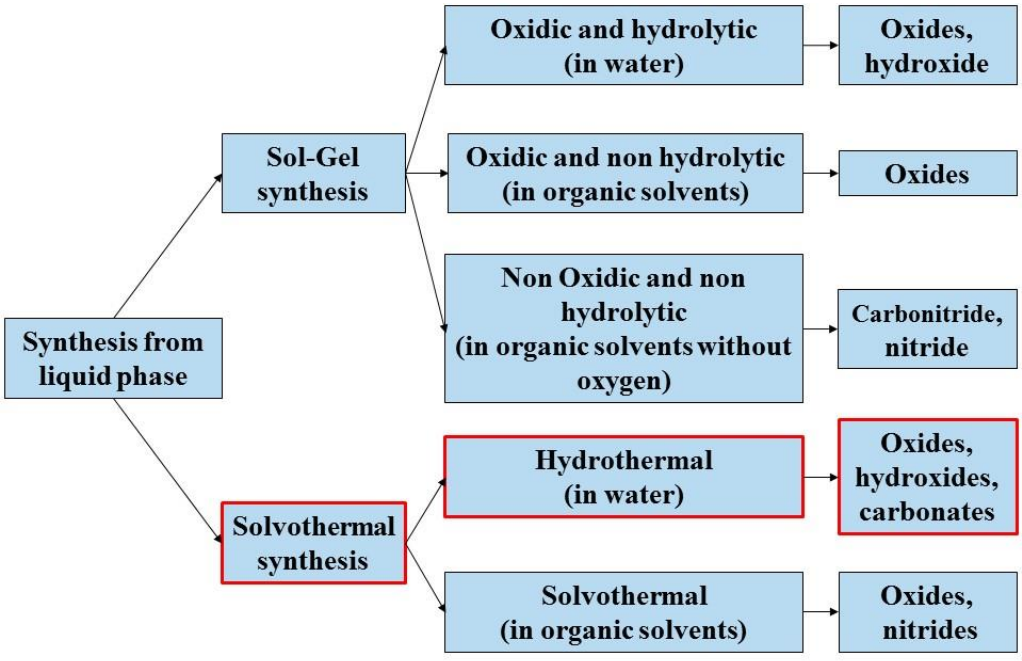

Figure 1.1: Synthesis method of ceramic materials from liquid phase

1.2 Hydrothermal synthesis

The term of "hydrothermal" purely originates from earth science, during the mid -19th century which implied an action of water at elevated temperature and pressure. This term was originally used by British geologist, Sir Rodrick Murchinson (1792-1871) to describe the various rock and mineral formation in the earth crust. Among the different definitions proposed by the various scientists, Byrappa and Yoshimura (2001) recently proposed definition for hydrothermal reaction as "any heterogeneous chemical reaction in the presence of a solvent above room temperature and at pressure greater than 1 atm in closed systems"[22].

Hydrothermal technique is an important synthesis method to prepare novel inorganic materials which have various properties such as photocatalytic[23], dielectric[24], superconducting[25], thermoelectric[26], conducting[27], magnetic[28] and antibacterial[29]. Since, this method can control the agglomeration of the metal oxide, morphology, crystal size and crystal structure by adjusting the pH of the reaction system, ratio of starting materials, temperature and reaction time it make this method a vital one[30–33]. The control of particle morphology can produce crystallites having well-developed shapes corresponding to particular crystallographic directions, such as whiskers, plates, or cubes. Moreover, hydrothermal system tends to reject

impurities with the crystallizing solution during the synthesis route which means this process is a self-purifying process. This kind of self-purifying process does not take place in other synthesis routes, such as high temperature calcination.

In the hydrothermal method, usually a special closed reaction vessel (Figure 1.2) is used to create high-temperature, high-pressure reaction environment with aqueous solutions. The reaction system can be pressurized by the vapor pressure generated by itself during the heating. This process dissolves and recrystallizes a compounds that are insoluble and poorly soluble under normal condition[34]. Such a closed reaction system has some advantages such as low air pollution, low energy consumption, high reactivity of reactance, easy to control the solution, formation of metastable phase and unique condensed phase[35]. Figure 1.3 shows the general preparation steps of the hydrothermal method. First, the raw materials (reactants) are dissolved in aqueous solution and transferred into a Teflon-lined steel autoclave. Then in the hydrothermal treatment, seed crystals are grown in the supersaturated solution and crystallizes at the bottom of the autoclave. Finally, crystalline product could be washed, centrifuge and dried for further characterization.

In the hydrothermal reaction water is one of most important solvent which is present naturally in abundant amounts. The major advantages of using water are

cheaper than other solvent, environmental friendly, nontoxic, nonflammable, noncarcinogenic, nonmutagenic thermodynamically stable, volatile, and it can act as a catalyst for the formation of desired material by tuning the pressure, and

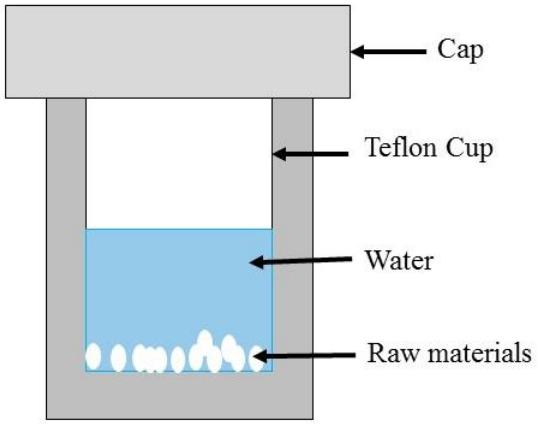

Figure 1.2: Schematic diagram of hydrothermal method equipment.

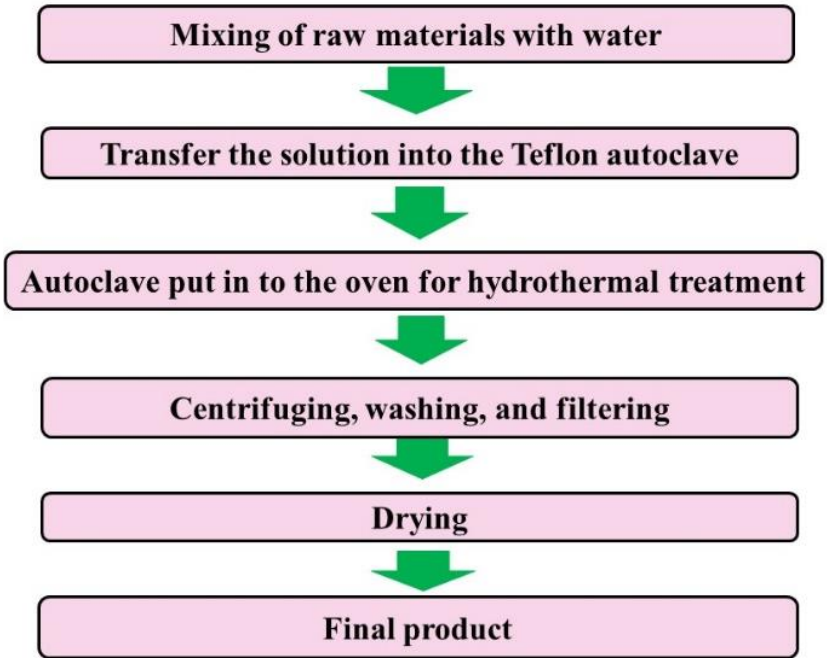

Figure 1.3: General steps of hydrothermal preparation.

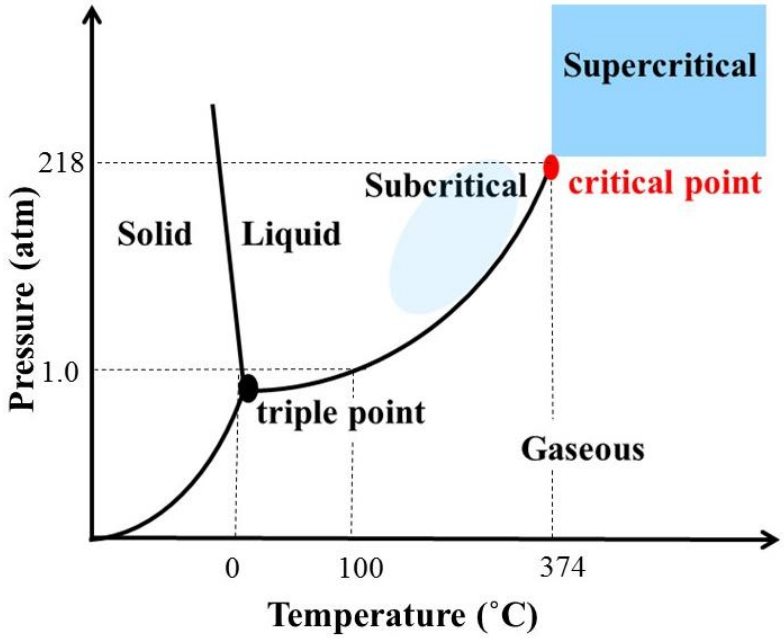

Figure 1.4: Phase diagram of water.

temperature. Based on a reaction temperature, hydrothermal synthesis is classified into subcritical and supercritical synthetic reactions. The subcritical synthesis (Figure 1.4) involves a temperature in the range of 100–240 °C, while in supercritical synthesis, the temperature could reach up to 400 °C, and the pressure is up to 3000 bar[36]. The water temperature and pressure at 374 °C and 218 atm known as critical point and which change the normal condition of water such as dielectric constant and solubility. As shown in, above this critical point it is known as a supercritical fluid and it exhibits unique properties[37]. Water at supercritical conditions behave very different from those of ambient liquid water. The water does not form neither a liquid nor gas above its critical point and both phases become indistinguishable having

properties between a gas and liquid[38]. In this condition dielectric constant is much lower, water exhibits very high specific heat capacities and water can appear as a reactive component as well as a catalyst[39]. The variation of dielectric constant of water with temperature increase and pressure decrease are shown in Figure 1.5. The high relative static dielectric constant of water 78.5 at room temperature drops to value of about 6 at critical point, so the addition of the dielectric constant to the reaction rate become remarkable in terms of the electrostatic theory. Therefore, hydrothermal synthesis and supercritical form of water not only affords great advantages by comparison with conventional solvents form the point of view of economy, ecology, and safety but it is also a suitable reaction medium particularly on account of its solvent parameters, which can be varied by adjusting the temperature and pressure.

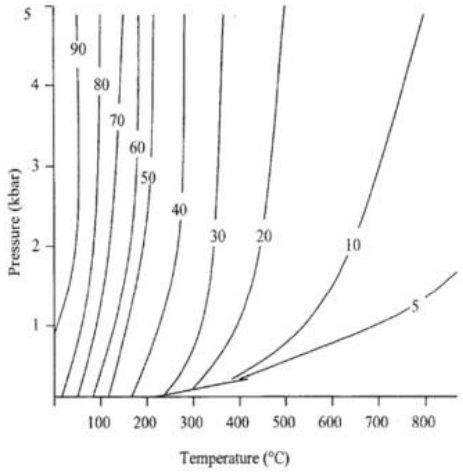

Figure 1.5 Variation of dielectric constant of water with temperature and pressure.

1.3 Hydrothermal synthesis of niobate and tantalate compounds

For recent development in telecommunications, electero-optics, piezoelectric materials, solid electrolytic capacitors and photochromic devices in Information Age alkali metal niobate and tantalate have been placed on a short list of functional materials in future technologies[40,41]. These compounds can be easily synthesized by the hydrothermal reaction and which produce various crystal structures such as pyrochlore-, perovskite-, layered-, or tunnel-type structures depending on the reaction condition[42–44]. Moreover, these niobate and tantalate structures are promising candidate for various applications such as photocatalyst[45], ferroelectricity[46], lead free piezomaterials[47], optical devices and ion-exchangers[48].

The discovery of photocatalytic activity in layered $K_4Nb_6O_{17}\cdot nH_2O$ initiated the research into photocatalytic water splitting using niobates[49,50]. So far, there have been a number of investigations on the applications of photocatalysis, including water splitting and degradation of organic contaminants in water[51,52]. The highest photocatalytic activity among the tantalates were reported by Kato *et al*[53]., using $NiO/NaTaO_3$:La photocatalyst with a 56% quantum yield with 270 nm cutoff filter. Moreover, perovskite-type alkali niobates, such as $LiNbO_3$, $LiTaO_3$, $NaNbO_3$ and $KNbO_3$ have been reported for many interesting properties such as

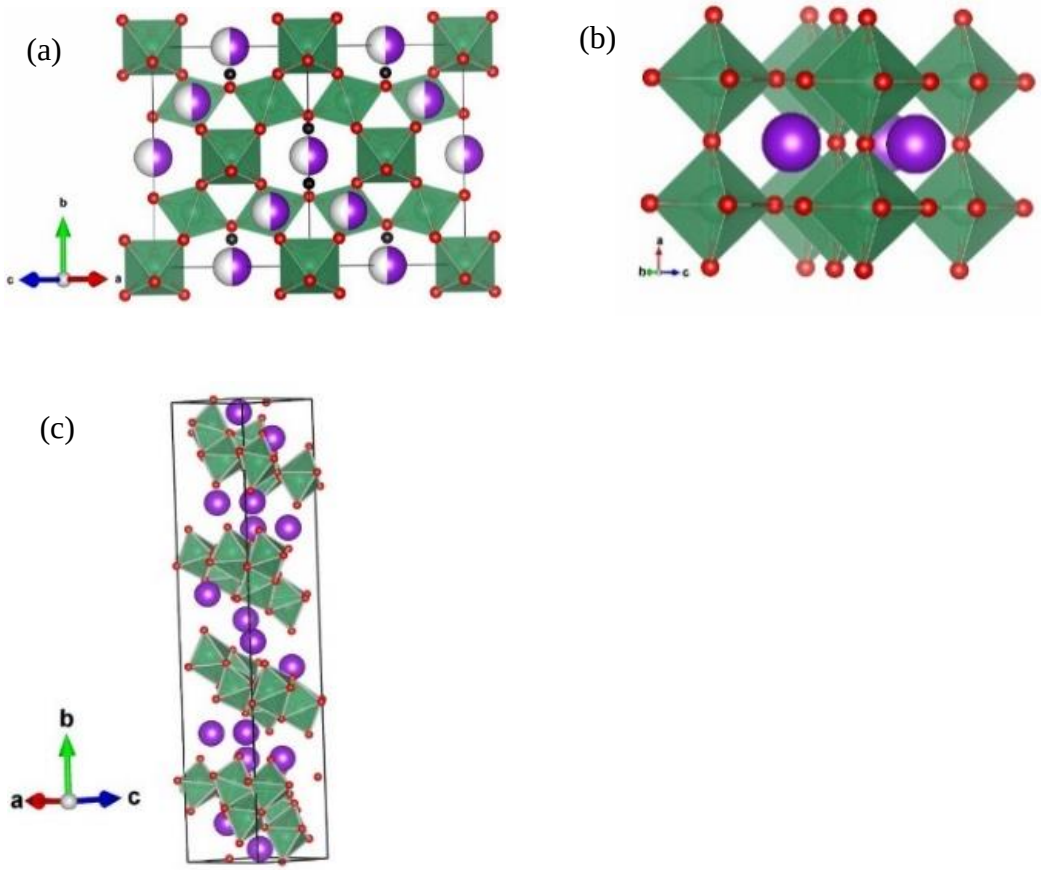

Figure 1.6: Crystal structure of various niobate and tantalates (a) $A_2B_2O_7$ with pyrochlore-type (b) ABO_3 with perovskite type and (c) $A_4B_6O_{17}\cdot nH_2O$ with layered-type.

piezoelectricity, ion conductivity, pyroelectricity, electro-optic and nonlinear optical behavior[54,55]. Thus, it is evident that these materials are employed in large scale in energy conversion application.

Previously, hydrothermally synthesis of pyrochlore-type tantalate was first reported by Kumada et al. in 1985[56]. So far, modification of hydrothermal treatment have been carried out to prepare pyrochlore-type $K_{0.88}H_{1.12}Nb_2O_6\cdot 1.58H_2O$, $Ca_2Nb_2O_7$, $Ca_2Ta_2O_7$ and $KLnTa_2O_7$[57–59]. Other than the pyrochlore-type

compounds K_2O-Nb_2O_5 /Ta_2O_5-H_2O hydrothermal system produce various crystal structure such as perovskite and layered-type[60,61] (Figure 1.6). In our research we were synthesized pyrochlore-, perovskite- and layered-type alkaline niobate and tantalate compounds by hydrothermal reaction and designed their applicable capability by transition metal incorporation.

1.4 Thesis Goals and Outline

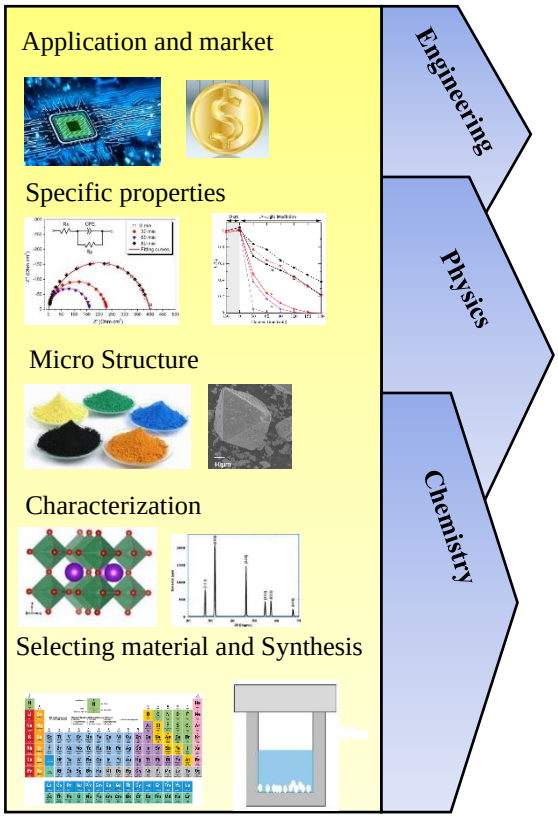

Figure 1.7: Schematic description of material science

The primary goals of this thesis research were to understand the crystal chemistry and applicable properties of alkali niobate and tantalate by hydrothermal

reaction. Design of the inorganic materials using environmental friendly low temperature reaction to check various day-to-day application. As shown in Figure 1.7 potential value of my thesis is evaluated by synthesis and processing, chemical and physical characterization, micro structure analysis, specific properties, applications and market. The chemistry, physics and engineering knowledge is equally involved to complete characterization in the entire length of the process. In the synthesis process we focus not only the material synthesis and process but also on the methods to being viable in real world applications. Thus, synthesis of materials involving hydrothermal methods shows great promise. Therefore, we opted to synthesize pyrochlore, perovskite and layered type niobate and tantalate structures by hydrothermal reactions, to evaluate the photocatalytic activity for the organic compounds degradations and the other applications such as ionic conductivity and antibacterial activities.

This dissertation is comprised of eight chapters. Chapter 2 will be dedicated to providing a useful background to the reader about the basic science underlying the photocatalytic, antibacterial and ionic conductivity experiments. Chapters 3 through 6 will cover the bulk of the thesis research focused on the hydrothermal synthesis and application of niobate and tantalate compounds.

Chapter 3 will describe the synthesis and Ag incorporation of pyrochlore, perovskite and layered structure by hydrothermal reaction. Thereafter, will compare the photocatalytic activity of silver incorporated and parent compounds towards phenol degradation. The photocatalytic phenomena discovered by Fujishima and Honda in 1972, which has been opened up a wide range of applications in areas such as hydrogen generation, self-cleaning applications, organic pollutant degradation

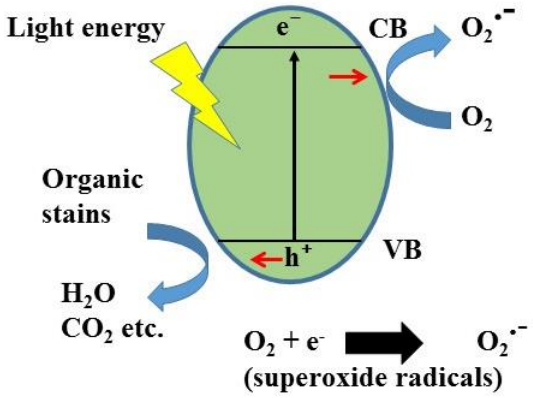

Figure 1.8: Schematic diagram of organic compounds degradation

and antibacterial activity for waste water treatment. One application of advance oxidation process in these photocatalytic materials play an important role in the waste water treatment. As shown in Figure 1.8, once the photocatalyst is irradiated with light, photogenerated electrons are exited from valance band of the photocatalyst to the conduction band. This photogenerated electrons can be used for the reduction reaction and at the same time oxidation reaction takes place at the

valance band. The oxidation reaction can decompose organic compounds to harmless product of CO_2 and H_2O, which could be a promising method for environmental friendly waste water treatment.

However, the limitation of most photocatalysts is the photoexcitation which occurs only with wavelengths near or shorter than 385 nm, and hence there is a need to realize photocatalytic materials which could actively utilize the solar radiation at visible or near ultra violet (UV) light. To obtained visible light active photocatalysts, various modification have been proposed such as cation doping, loading, anion doping and ion exchange. In chapter three we try to obtain silver loaded and doped samples to increase the photocatalytic activity of the pyrochlore, perovskite and layered structures.

Chapter four is the extended study of chapter three and it will describes the further modification of pyrochlore type potassium niobate and tantalate compounds by silver ion exchanged reaction. The K^+ ions in these compounds were reacted with Ag^+ ions in excess molten $AgNO_3$ and produce fluorite-type silver niobate and pyrochlore-type silver tantalate compounds. This reaction decreased the band gap of both samples in the UV region to visible region due to the Ag d orbital association in the hybridized energy levels and show remarkable photocatalytic activities in

silver tantalate. Moreover, these silver based compounds are not only known for visible light driven photocatalyst, but also they show very good ionic conductivitiese. After the discovery of superionic conductivity of silver iodide containing solid electrolytes, Ag based compounds ionic conductivity have been extensively studied[62,63]. Moreover, ionic condouctiviy of solid electrolytes have gained a lot of attention recently due to their aplications in solid oxides fuel cell (SOFC), gas sensors, oxygen separation membrane, batteries and catalyst[64–66]. Therefore we investigated the ionic conductivity of silver ion-exchanged niobate and tantalate samples.

In chapter five pyrochlore-type potassium niobate (KN) and tantalate (KT) were synthesized by a hydrothermal reaction according to a method described in

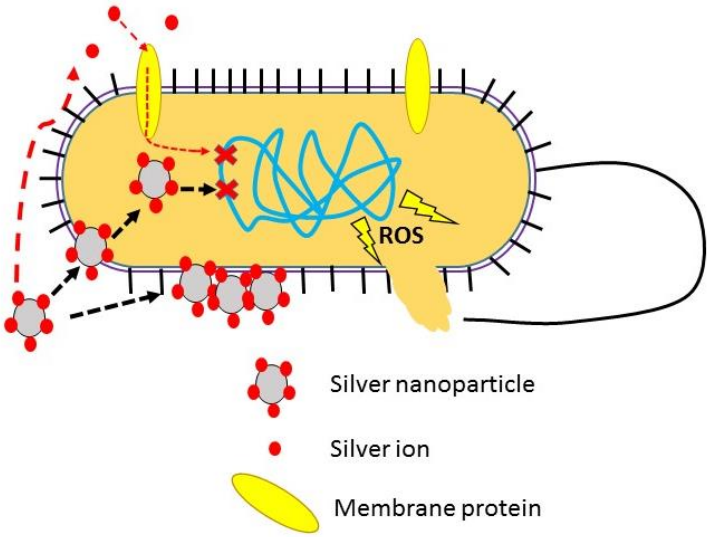

Figure 1.9: Schematic mechanisms for antibacterial behaviors of silver nanoparticles.

chapter four and ion exchanged reaction carried out at different molar ratios of $AgNO_3$. The three different ion exchanged molar ratios of niobate and tantalate were used to prepare the six samples with silver doped as well as complete ion exchanged samples. In this study, antibacterial activity of Ag ion-exchanged and parent samples were evaluated by colony count method and further compared by area of inhibition zone in disk diffusion tests. Other than the water splitting and organic compounds degradations these ceramic materials, have ability to control the bacterial growth and it can lead to a variety of other applications such as, implantable orthopedic biomaterials, bone replacements, building materials, cosmetics and treatment of burn wounds. Among the antibacterial materials silver containing materials have gain great attention due to their strong antibacterial activity and low toxicity against mammalian cells. As shown in Figure 1.9, when silver ion released, it can attach to the negatively charged bacteria cell wall by coulombic interactions and this will cause an imbalance on the surface charge around the cell. This electrostatic force and unstable surface charge lead to a disruption of the cell wall and plasma membrane, causing cell lysis and death. Moreover, metal ions uptake into cell by channels of the bacterial cell membrane can cause intracellular depletion and disruption of DNA replication. As well as, the metal cation, these photocatalytic materials can introduce

a special antimicrobial mechanism by generating reactive oxygen species (ROS) such as superoxide anion ($.O^{2-}$), hydroxyl radical (.OH) and H_2O_2[67,68]. The ROS with strong oxidation power can oxidize organics (including the cell membrane of microbes) eventually into CO_2 and H_2O. This thesis was to obtain controllable antibacterial properties from silver ion-exchanged niobate and tantalate structures. Chapters six is the extended study of chapter five and it will describe the further investigation of antibacterial activity of silver loaded perovskite-type niobate compounds.

Finally, chapter 7 summarizes the main findings of the thesis research and chapter 8 discusses the potential future impact, social awareness, business creation of the research.

1.5 References

(1) Priya, S.; Song, H.; Zhou, Y.; Varghese, R.; Chopra, A. A Review on Piezoelectric Energy Harvesting : Materials , Methods , and Circuits. *Energ. Harve. and Sys.*, **2017**, *4* (1), 3–39.

(2) Wei, C.; Jing, X. A Comprehensive Review on Vibration Energy Harvesting: Modelling and Realization. *Renew. Sust. Energ. Rev.*, **2017**, *74*, 1–18.

(3) Key, A.; Proffitt, T.; Torre, I. De; Key, A. Raw Material Optimization and Stone Tool Engineering in the Early Stone Age of Olduvai Gorge (Tanzania). *J. R. Soc. Interface.*, **2019,** 17.

(4) Miller, D. Smelter and Smith : Iron Age Metal Fabrication Technology in Southern Africa, *J. Arch. sci.,* **2002**, 29, 1083–1131.

(5) Hughes, D. C.; Sugden, D.B.; Jaglin, D.; Mucha, D, Calcination of Roman Cement : A Pilot Study Using Cement-Stones from Whitby, *Con. Buil. Mater.*, **2007**, *22*, 1446–1455.

(6) Bragg, P. W. H.; W. L. Bragg.; The reflection of X-ray by crystals, *Nature*, **1913**, 428–438.

(7) Łukasiak, L.; Jakubowski, A, History of Semiconductors. *J. Tele. Info. Tec.*, **1929**, 1-9.

(8) Takizawa, H.; Survey of new material by solid state synthesis under external field: high-pressure synthesis and microwave processing of inorganic materials. *J. Ceram. Soc. Jpn.*, **2018**, 126 (6), 424-433.

(9) Martínez-zarzoso, I.; Maruotti, A, The Impact of Urbanization on CO_2 Emissions : Evidence from Developing Countries. *Ecol. Econ.*, **2011**, *70* (7), 1344–1353.

(10) Moriarty, P.; Honnery, D. What Energy Levels Can the Earth Sustain, *Energy Policy*, **2009**, *37*, 2469–2474.

(11) Chu, S.; Majumdar, A. Opportunities and Challenges for a Sustainable Energy Future. *Nature*, **2012,** 488.

(12) Akpan, U. G.; Hameed, B. H.: General The Advancements in Sol–Gel Method of Doped-TiO_2 Photocatalysts. *Appl. Catal.*, **2010**, *375*, 1–11.

(13) Jasinski, M. S.; Meyerson, B. S.; Scott, B. A.; Mechanistic Studies of Chemical Vapor Deposition, *Ann. Rev. Phys. Chem*, **1987**, 38, 109-140.

(14) Kumada, N. Preparation and Crystal Structure of New Inorganic Compounds by Hydrothermal Reaction., *J. Ceram. Soc. Jpn.* **2013**, 121(2), 135–141.

(15) Figueiredo, J. L.; Órfão, J. J. M.; Pereira, M. F. R., Environmental Highly Active N-Doped Carbon Nanotubes Prepared by an Easy Ball Milling Method for Advanced Oxidation Processes., *Appl. Catal.***, 2016**, *192*, 296–303.

(16) Ã, L. W.; Xu, X.; Yuan, X. Preparation and Photoluminescent Properties of Doped Nanoparticles of ZnS by Solid-State Reaction. *J. lumin*, **2010**, *130*, 137–140.

(17) Guijun, Y.; Soo-jin, P.;Review, A. Conventional and Microwave Hydrothermal Synthesis and Application of Functional Materials: A Review., *materials*, **2019**,12, 1177.

(18) Kappis, K.; Papadopoulos, C.; Papavasiliou, J.; Vakros, J.; Georgiou, Y.; Deligiannakis, Y.; Avgouropoulos, G. Tuning the Catalytic Properties of Copper-Promoted Nanoceria via a Hydrothermal Method., *catalysts*, **2019**, 9, 138.

(19) Method, A. C. Fluorescence and EPR Characteristics of Mn^{2+} -Doped ZnS Nanocrystals Prepared by Aqueous Colloidal Method. *J. Phys. Chem. B,* **1999**, 103, 754–760.

(20) Li, C.; Sun, Z.; Xue, Y.; Yao, G.; Zheng, S. A Facile Synthesis of G-C_3N_4/TiO_2 Hybrid Photocatalysts by Sol–Gel Method and Its Enhanced Photodegradation towards Methylene Blue under Visible Light. *Adv. Powder Technol.,* **2016**, *27* (2), 330–337.

(21) Ghorbani, H. R.; Mehr, F. P.; Pazoki, H.; Rahmani, B. M., Synthesis of ZnO Nanoparticles by Precipitation Method., *Orient.J.Chem.*, **2015**, 32(2) 1219–1221.

(22) Byrappa, K.; Yoshimura, M. Handbook of Hydrothermal Technology, Noyes Publications, New Jersey, USA, **2001**.

(23) Liu, J. W.; Chen, G.; Li, Z. H.; Zhang, Z. G. Hydrothermal Synthesis and Photocatalytic Properties of $ATaO_3$ and $ANbO_3$ (A = Na and K). *Int. J. Hydrog. Energy*, **2007**, *32*, 2269–2272.

(24) Dutta, P. K.; Asiaie, R.; Akbar, S. A.; Zhug, W. Hydrothermal Synthesis and Dielectric Properties of Tetragonal $BaTiO_3$. *Chem. Mater.*, **1994**, 6, 1542–1548.

(25) Saiduzzaman, M.; Yoshida, H.; Takei, T.; Yanagida, S.; Kumada, N.;Nagano, M.; Hisanori, Y.; Azuma, M.; Rubel, M. H. K.; Chikako, M.; Kuroiwa, Y., Hydrothermal Synthesis and Crystal Structure of a $(B_{0.54}K_{0.46})_4Bi_4O_{12}$ Double-Perovskite Superconductore with Oneset of the Transition T_c ~30 K., *Inorg.Chem.*, 2019, 58, 11997-12001.

(26) Tai, G.; Guo, W.; Zhang, Z., Hydrothermal Synthesis and Thermoelectric Transport Properties of Uniform Single-Crystal Pearl-Neckllace-Shaped PbTe Nanowires., *Cryst. Growth. Des.*, 2008, 8, 2906-2911.

(27) Rong, A.; Gao, X. P.; Li, G. R.; Yan, T. Y.; Zhu, H. Y.; Qu, J. Q.; Song, D. Y. Hydrothermal Synthesis of Zn_2SnO_4 as Anode Materials for Li-Ion Battery. *J. Phys. Chem. B*, **2006**, 110, 14754–14760.

(28) Peng, J.; Hojamberdiev, M.; Xu, Y.; Cao, B.; Wang, J.; Wu, H., Hydrothermal Synthesis and Magnetic Properties of Gadolinium-Doped. *J. Magn. Magn. Mater.*, **2011**, *323*, 133–137.

(29) Yang, G.; Xie, J.; Deng, Y.; Bian, Y.; Hong, F. Hydrothermal Synthesis of Bacterial Cellulose / AgNPs Composite : A " Green " Route for Antibacterial Application. *Carbohydr. Polym.*, **2012**, *87* (4), 2482–2487.

(30) Yan, Y.; Wu, Y.; Yan, Y.; Guan, W.; Shi, W. Inorganic-Salt-Assisted Morphological Evolution and Visible-Light-Driven Photocatalytic Performance of Bi_2WO_6 Nanostructures., *J. Phys. Chem. C*., **2013**, 117, 20017-20028.

(31) Ruan, Q.; Zhang, W. Tunable Morphology of $Bi_2Fe_4O_9$ Crystals for Photocatalytic Oxidation.,*J. Phys. Chem. C*., **2009**, 113, 4168–4173.

(32) Obregón, S.; Caballero, A.; Colón, G. Hydrothermal Synthesis of $BiVO_4$: Structural and Morphological Influence on the Photocatalytic Activity. *Appl. Catal. B.*, **2012**, *117–118*, 59–66.

(33) Zhang, A.; Zhang, J.; Cui, N.; Tie, X.; An, Y.; Li, L. Effects of pH on Hydrothermal Synthesis and Characterization of Visible-Light-Driven $BiVO_4$ Photocatalyst. *J. Mole. Catal-Chem.*, **2009**, *304*, 28–32.

(34) Morey, G. W.; Niggli, P. The Hydrothermal Formation of Silicates, A Review.,*Geographycal laboratory,* **1913,** 1086-1030.

(35) Johnson, E. B. G.; Arshad, S. E. Applied Clay Science Hydrothermally Synthesized Zeolites Based on Kaolinite : A Review. *Appl. Clay Sci.*, **2014**, *97–98*, 215–221.

(36) Quitain, A. T.; Herng, C. Y.; Yusup, S. Conversion of Biomass to Bio-Oil in Sub- and Supercritical Water., *Biofuel-status and perspective,* **2015,** 459-476.

(37) Lester, E.; Blood, P.; Denyer, J.; Giddings, D.; Azzopardi, B.; Poliakoff, M. Reaction Engineering : The Supercritical Water Hydrothermal Synthesis of Nano-Particles., *J. Supercrit. fluids.*, **2006**, *37*, 209–214.

(38) Savage, P. E.; Rearrangements, C. Organic Chemical Reactions in Supercritical Water. *Chem. Rev*, **1999**, 99, 603-621.

(39) Bröll, D.; Kaul, C.; Krämer, A.; Krammer, P.; Richter, T.; Jung, M.; Vogel, H.; Zehner, P. Chemistry in Supercritical Water., *Angew. Chem. Int. Ed. Engl*., 1999, 38 (20), 2998-3014.

(40) Maeder, M. D.; Damjanovic, D.; Setter, N. Lead Free Piezoelectric Materials., *J. Electroceramics*, **2004**, 13, 385–392.

(41) Domaradzki, J.; Wojcieszak, D.; Kotwica, T.; Mańkowska, E. Memristors : A Short Review on Fundamentals , Structures , Materials and Applications. *Intl. J. Electro. Teleco*., **2020**, *66* (2), 373–381.

(42) Magrez, A.; Vasco, E.; Seo, J. W.; Dicker, C.; Setter, N.; Forró, L. Growth of Single-Crystalline $KNbO_3$ Nanostructures. *J. Phy. Chem. B* **2006**, *110* (1), 58–61.

(43) Hu, Y.; Gu, H.; Hu, Z.; Di, W.; Yuan, Y.; You, J.; Cao, W.; Wang, Y.; Chan, H. L. W. Controllable Hydrothermal Synthesis of $KTa_{1-x}Nb_xO_3$ Nanostructures with Various Morphologies and Their Growth Mechanisms. *Cryst. Growth Des.,* **2008**, *8* (3), 832–837.

(44) Wu, J.; Zhou, C.; Zhao, Y.; Shang, L.; Bian, T.; Shao, L.; Shi, F.; Wu, L. Z.; Tung, C. H.; Zhang, T. One-Pot Hydrothermal Synthesis and Photocatalytic Hydrogen Evolution of Pyrochlore Type $K_2Nb_2O_6$. *Chin. J. Chem.,* **2014**, *32* (6), 485–490.

(45) Ding, Q.-P.; Yuan, Y.-P.; Xiong, X.; Li, R.-P.; Huang, H.-B.; Li, Z.-S.; Yu, T.; Zou, Z.-G.; Yang, S.-G. Enhanced Photocatalytic Water Splitting Properties of $KNbO_3$ Nanowires Synthesized through Hydrothermal Method. *J. Phys. Chem. C,* **2008**, *112* (48), 18846–18848.

(46) Pattanayak, S.; Choudhary, R. N. P.; Das, P. R. Effect of Sm-Substitution on Structural, Electrical and Magnetic Properties of $BiFeO_3$. *Electron. Mater. Lett.,* **2014**, *10* (1), 165–172.

(47) Joung, M.; Xu, H.; Seo, I.; Kim, D.; Hur, J.; Nahm, S.; Kang, C.; Yoon, S.; Park, H. Piezoelectric Nanogenerators Synthesized Using $KNbO_3$ Nanowires with Various Crystal Structures. *J. Mater. Chem.,* **2014**, *2*, 18547–18553.

(48) Waroquet, A.; Demange, V.; Hakmeh, N.; Perriere, J.; Freslon, S.; Deputier, S.; Guilloux-viry, M. Epitaxial Growth and Cationic Exchange Propertiese of Layered KNb_3O_8 thin film, *RSC Adv*., **2017**, 7, 15482–15491.

(49) Zhang, G.; He, F.; Zou, X.; Gong, J.; Zhang, H. Hydrothermal Preparation and Photocatalytic Properties of Sheet-like Nanometer Niobate $K_4Nb_6O_{17}$. *J. Phys. Chem. Solids.*, **2008**, *69* (5–6), 1471–1474.

(50) Lin, H. Y.; Lee, T. H.; Sie, C. Y. Photocatalytic Hydrogen Production with Nickel Oxide Intercalated $K_4Nb_6O_{17}$ under Visible Light Irradiation. *Int. J. Hydrog. Energy.*, **2008**, *33* (15), 4055–4063.

(51) Ahmed, S.; Rasul, M. G.; Martens, W. N.; Brown, R.; Hashib, M. A. Heterogeneous Photocatalytic Degradation of Phenols in Wastewater: A Review on Current Status and Developments. *Desalination.*, **2010**, *261* (1–2), 3–18.

(52) Wang, Z.; Cai, W.; Hong, X.; Zhao, X.; Xu, F.; Cai, C. Photocatalytic Degradation of Phenol in Aqueous Nitrogen-Doped TiO_2 suspensions with Various Light Sources. *Appl. Catal. B.*, **2005**, *57* (3), 223–231.

(53) Kato, H.; Asakura, K.; Kudo, A. Highly Efficient Water Splitting into H_2 and O_2 over Lanthanum-Doped $NaTaO_3$ Photocatalysts with High Crystallinity and Surface Nanostructure., *J. Am. Chem.Soc.* **2003**,125, 3082–3089.

(54) Wang, K.; Li, J. (K,Na)NbO_3 -Based Lead-Free Piezoceramics : Phase Transition , Sintering and Property Enhancement. *J. Adv. Ceram*, **2012**, *1* (1), 24–37.

(55) Lou, X.; Li, R.; Zhu, X.; Luo, L.; Chen, Y.; Lin, C.; Li, H.; Zhao, X. S. New Anode Material for Lithium-Ion Batteries: Aluminum Niobate ($AlNb_{11}O_{29}$), *ACS. Appl. Mater. Interfaces.* **2019**, 11,6 6089–6096.

(56) Kumada, N.; Ozawa, N.; Kinomura, N.; Muto, F., Preparation of Pyrochlores.$A_{1-x}H_xTaO_3$. nH_2O (A = Na, K), *Mat.Res.Bull.* **1985**, *20*, 583–589.

(57) Smirnova, O.; Kumada, N.; Yonesaki, Y.; Kinomura, N. A New Solid Electrolyte to Fill the Gap between Low Temperatures and High Temperatures SOFC Materials? *Electrochem. Commun.*, **2008**, *10* (3), 485–487.

(58) Atuchin, V. V; Kalabin, I. E.; Kesler, V. G.; Pervukhina, N. V. Nb 3d and O 1s Core Levels and Chemical Bonding in Niobates. *J. Elect. Spect. Rel. Phenom.*, **2005**, *142*, 129–134.

(59) Nyman, M.; Rodriguez, M. A.; Shea-rohwer, L. E.; Martin, J. E.; Provencio, P. P. Highly Versatile Rare Earth Tantalate Pyrochlore Nanophosphors. *J. Am.Chem. Soc.*, **2009**, 131, 33, 11652–11653.

(60) Kumada, N.; Dong, Q.; Yonesaki, Y.; Takei, T.; Kinomura, N. Hydrothermal Synthesis of $NaNbO_3$ morphology Change by Starting Compounds. *J. Ceram. Soc. Jpn.* **2011**, *119* (1), 483–485.

(61) Uchida, S.; Inoue, Y.; Fujishiro, Y.; Sato, T., hydrothermal synthesi of $K_4Nb_6O_{17}$., *J. Mate. Sci*., 1998, 33, 5125-5129.

(62) Ida, T. Ionic Conductivity of Small-Grain Polycrystals of Silver Iodide. *Solid State Ion.*, **1998**, *107* (3–4), 313–318.

(63) Arof, A. K.; Seman, K. C.; Hashim, A. N.; Yahya, R.; Maah, M. J.; Radhakrishna, S. A New Silver Ion Conductor for Battery Applications. *Mater. Sci. Eng. B.*, **1995**, *31* (3), 249–254.

(64) Stambouli, A. B.; Traversa, E. Solid Oxide Fuel Cells (SOFCs): A Review of an Environmentally Clean and Efficient Source of Energy. *Renew. Sust. Energ. Rev.*, **2002**, *6* (5), 433–455.

(65) Yamamoto, O.; Arachi, Y.; Sakai, H.; Takeda, Y.; Imanishi, N.; Mizutani, Y.; Kawai, M.; Nakamura, Y. Zirconia Based Oxide Ion Conductors for Solid Oxide Fuel Cells. *Ionics.*, **1998**, *4* (5–6), 403–408.

(66) Kharton, V. V.; Marques, F. M. B.; Atkinson, A. Transport Properties of Solid Oxide Electrolyte Ceramics: A Brief Review. *Solid State Ion.*, **2004**, *174* (1–4), 135–149.

(67) Song, B.; Zhang, C.; Zeng, G.; Gong, J.; Chang, Y. Antibacterial Properties and Mechanism of Graphene Oxide-Silver Nanocomposites as Bactericidal Agents for Water Disinfection. *Arch. Bioche. Biophys.* **2016**, *604*, 167–176.

(68) Honda, M.; Kawanobe, Y.; Ishii, K.; Konishi, T.; Mizumoto, M.; Kanzawa, N.; Matsumoto, M.; Aizawa, M. In Vitro and in Vivo Antimicrobial Properties of Silver-Containing Hydroxyapatite Prepared via Ultrasonic Spray Pyrolysis Route. *Mater. Sci. Eng. C.*, **2013**, *33* (8), 5008–5018.

CHAPTER 2

EXPERIMENTAL TECHNIQUES

Each chapter contains an experimental section detailing the specifics of this work while this chapter is dedicated to providing insight into the basic experimental and analytical techniques with an emphasis on the analytical instrumentation used for the characterization of the synthesized photocatalysts, and the instrumentation used for the product analysis of the organic compounds degradations, antibacterial activity and ionic conductivities.

2.1 Materials and product characterization techniques

2.1.1 Synchrotron radiation X- ray diffraction (SXRD)

SXRD is a powerful technique that was used to characterize, identify and refine the crystal structure of samples investigated in this thesis work. Here, we have obtained the data from SPring-8 synchrotron radiation facility. SPring-8 is the world's largest third-generation synchrotron facility which consist of linear accelerator, a booster synchrotron and storage ring as shown in Figure 2.1. This high energy synchrotron radiation facility provides huge opportunities to researchers for conducting researches in material science, earth science, life science, environmental science, spectroscopic analysis and industrial applications. Synchrotron Radiation

(SR) is an electro-magnetic wave emitted from electrons which are accelerating almost speed of light in booster synchrotron. The booster synchrotron can accelerate electrons total energy up to 8 GeV and thus, it has named as "**S**uper **P**hoton **ring-8** GeV" or **SPring-8**. The diameter of the storage ring is approximately 396 m and it has 44 straight sections connected to the bend section[1,2]. The section that utilize in this facility depend on the experimental type and here we used the BL02B2 and BL14B2 beamlines for our research.

BL02B2 beamlines. The BL02B2 beamline could be a powder diffraction line which designed for charge density study by powder specimens within the area of material science. This experimental hatch is equipped with imaging plate as a detector and multi modular system constructed by six MYTHEN detectors. The

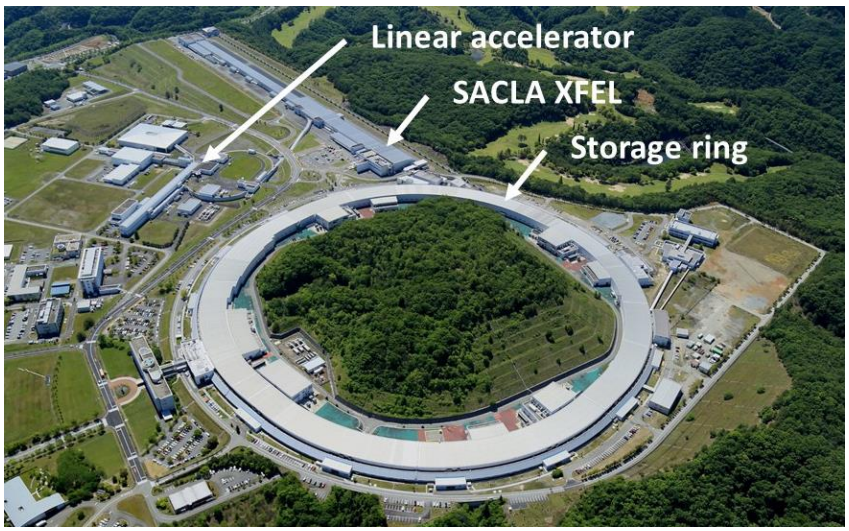

Figure 2.1: The Spring -8 third generation synchrotron radiation source. (Image from www. Spring8.or.jp).

beamline energy range is 12 to 37 keV, make it possible to collect powder diffraction data with high-counting statics and high-angular resolution. Moreover, this beamline sample temperature also can be changed in a wide range from 20 K to 1073 K using low temperature and high temperature nitrogen injection system[3]. Therefore, this high-energy powder diffraction system used in various research fields such as charge density studies of functional materials, structural aspect of phase transition, *Ab*-initio structure determination using powder diffraction data, structural refinement by Rietveld method and In-situ powder diffraction experiment under gas and vapor adsorption or desorption.

BL14B2 beamlines. Theis is a medium-length hard X-ray bending magnet beamline which is aim for engineering science research. This synchrotron radiation beamline promote to use industrial users and main technique on this is X-ray absorption. The energy range is 3.8 to 72 keV and X-ray imaging device and X-ray absorption fine structure (XAFS) equipment are prepared in the experimental hutch[4]. This synchrotron radiation system used in various research fields such as X-ray imaging, XAFS in wide energy region, XAFS of dilute systems and thin films and time resolved XAFS by quick scan.

2.2.2 X-ray Diffraction (XRD)

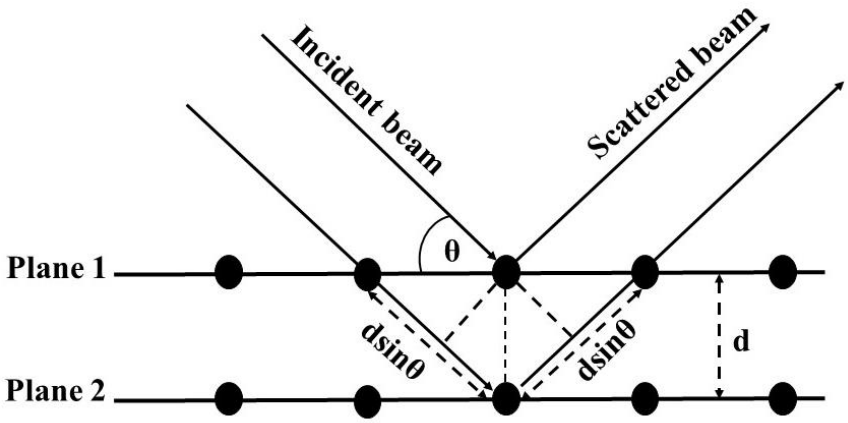

Figure 2.2: Schematic describing of Braggs Law

Powder X-Ray diffraction is a impressive technique that was used to characterize and identify the physical properties of the materials in this thesis work. The concept used in XRD is the diffraction and interference of monochromatic X-rays as they are incident on a samples. The resulting scattered X-rays of a sample is created by the constructive and destructive interference as shown in Figure 2.2. The resulting diffraction pattern and path difference between X-rays scattered can be explained by considering the Bragg diffraction law: $n\lambda=2d\sin\theta$, where, *n* is a positive integral, λ is the wavelength of the incident monochromated X-ray source, θ is the scattering angle, and *d* is the interplanar distance of crystalline solid[5]. The XRD data presented in this thesis was obtained on a MiniFlex 600, X-ray Powder Diffractometer equipped with a 2 kW Cu Kα [λ= 0.15418 nm] radiation.

2.2.3 Scanning electron microscopy (SEM)

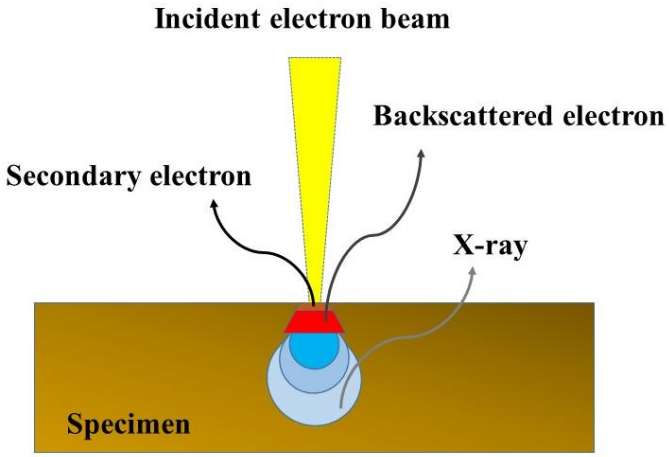

Figure 2.3: Illustration of the different types of signals used in SEM, and their origins in the specimen.

Scanning electron microscopy (SEM) is a type of electron microscope which uses electrons for imaging at a lower energy (0.4-40 keV). The electron beam interact with sample generates various signals containing surface morphology and composition of the samples[6]. The electron beam scanned the specimen by raster scan pattern and the position of the beam combining produce an image. Incident electron beam with the sample also produce characteristic X-rays and which is employed to obtain the elemental composition of the sample. The use of these X-ray emissions to gather semi-qualitative information on the sample is known as energy dispersive X-ray spectroscopy (EDS or EDX). All SEM micrographs presented in this thesis were obtained using JEOL F6500 and Miniscope TM3030 microscopes operating at 0.01-

30 kV and 5 -15 kV respectively. EDS spectroscopic analysis was performed by Miniscope TM3030 microscope and analysis using Quantax 70 analyzing software.

2.2.4 X-Ray Photoelectron Spectroscopy (XPS)

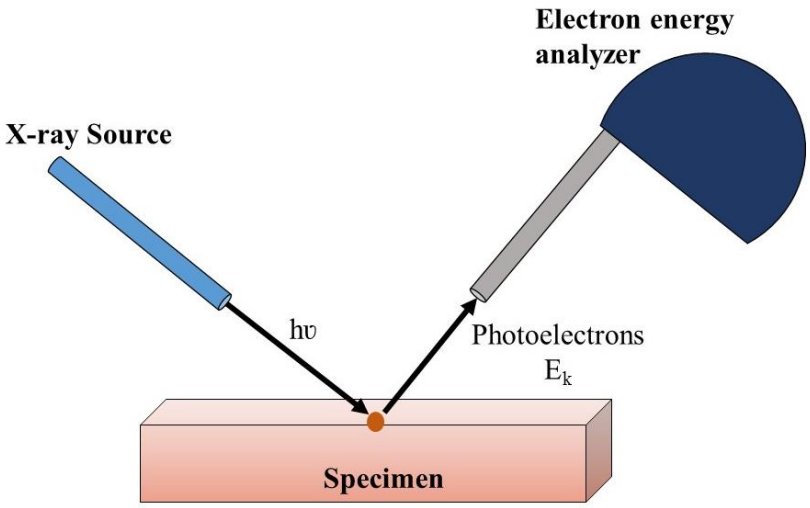

Figure 2.4: Schematic diagram showing the X-ray source, specimen and the electron energy analyzer in a X-ray photoelectron spectrophotometer.

X-ray photoelectron spectroscopy (XPS) is a powerful surface-sensitive analytical technique that can be identified useful qualitative and quantitative information in materials using Einstein's photoelectric effect. Under working environment, X-rays incident on a material surface emitted core level electrons which will be at a specific kinetic energy, and binding energy denoted by the following equation.

$$E_{binding} = h\upsilon - E_{kinetic} - \phi$$

$E_{binding}$ is the binding energy of the electron measured, equal to the difference in energy of the incident X-ray photon being used ($h\upsilon = h$ is Planck's constant, υ is the frequency), the kinetic energy of the ejected electron as measured by the instrument ($E_{kinetic}$), and work function of the specific surface(ϕ)[7,8].

The binding energy of an electron depends on the number of core level electrons, nuclear charge and bonding to nearby atoms, thus $E_{binding}$ can provide information on the elemental composition as well as their chemical state and the overall electronic structure in the materials. For example, the 284.8 eV energy required to eject a 1s electron from a carbon atom in a C-C bond as well as oxygen having a C-O bond, would require 286.8 eV to eject the same electron. This core level shifting denoted the different chemical environments of the carbon. In general, change in the chemical bonding of the element is shift the binding energy of a core electron.

XPS data obtained for this thesis work was primarily acquired on Axis-Ultra-DLD instrument 267 mm hemispherical analyzer operating in constant energy mode with an X-ray generator, Mg Kα with a power rating of 600 W. Related to the research outlined in the research Ag 3d region were evaluated using XPS. Ag $3d_{5/2}$ and $3d_{3/2}$ peaks appear range of 367.5-367.8 eV and 368.0-368.4 eV respectively.

These values are used to find the oxidation state of Ag (Ⅰ) and Ag (0), thus making XPS a useful technique to determine the chemical state of the silver.

2.2.5 High Performance Liquid Chromatography (HPLC)

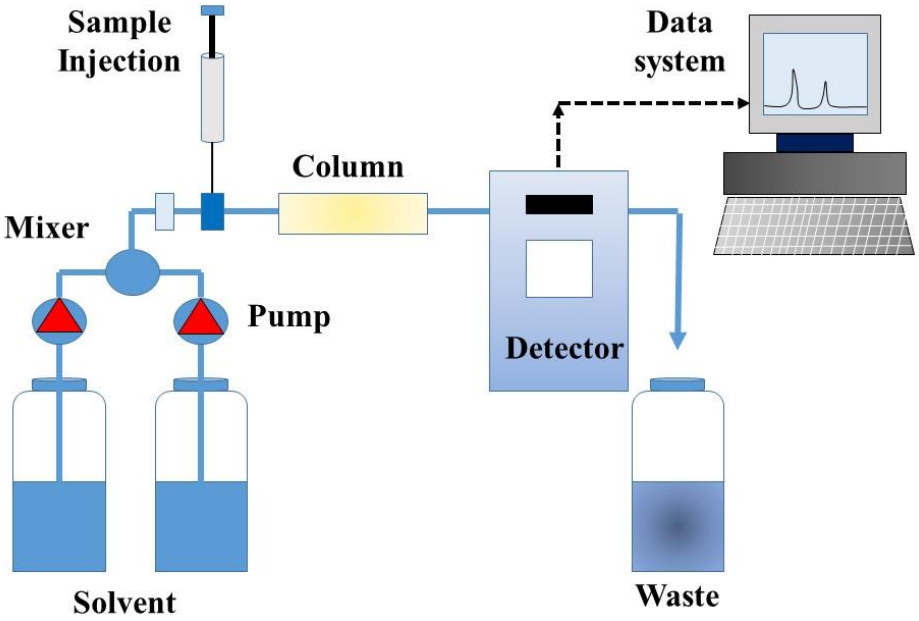

Figure 2.5: Schematic diagram showing the pump, sample inject, column, detector and data system in HPLC instrument.

HPLC is commonly used in analytical chemistry for separating, analyzing, identifying and quantify each components in a mixture. A sample in the pressurized liquid form is injected into chromatographic column filled with a solid adsorbent material. This absorbent lead to the separation of the sample and various components will elute at different times. This absorbent peak will be used to calculate the concentration of the particular solution[9]. The common mobile phase used in HPLC is acetonitrile and methanol combining with water. Most commonly Uv-vis

absorbance detectors are employed to detect physical or chemical properties of the solute. In this work a JASCO HPLC LC-2000 equipment was employed to check the phenol concentration after photocatalytic degradation. Ultrapure methanol, acetonitrile and water were used as the carrier liquids.

2.2 Photocatalytic, Antibacterial and Ionic conductivity tests

2.2.1 Photocatalytic activity analysis by phenol degradation

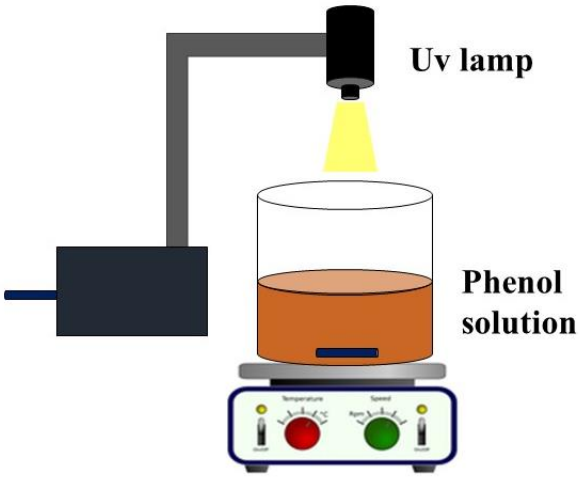

Figure 2.6: Schematic diagram showing the photocatalytic phenol degradation

The photocatalytic activity was analyzed by the decomposition of a 20 ppm phenol solution. Aqueous phenol solution was prepared by ultrapure water and sample catalyst was suspended at concentration of 3 g/L. Before the irradiation, the mixture was stirred in the dark for 30 min in order to check the absorption of phenol on the surface of the sample[10]. Then the mixture was irradiated using ultraviolet light

from a 300 W Xe lamp (UXR-300DU, Ushio Inc.), without any cutoff filter. The experiment was conducted for 210 min with continuous stirring. The time-depend phenol concentration was analyzed by high performance liquid chromatography. (JASCO HPLC LC-2000).

2.2.2 Antibacterial test

Colony count method: The antimicrobial tests were evaluated by colony count method using *E. coli* and *S. aureus* bacteria. The bacteria were cultivated in Soybean-Casein Digest Broth with Lecithin Polysorbate (SCDLP) medium overnight at 37 °C in a vibration incubator (150 rpm). To calibrate the initial concentration, bacterial solution was diluted to 5×10^5 CFU/ml (colony forming unit per ml). Then the 0.1 ml of bacterial solutions were pipetted into a centrifuge tube with 4.9 ml powder samples soaked SCDLP solution where solutions were filtered by 0.1 g of powder sample vibrating at 150 rpm overnight at 37 °C. After 24 hours 0.1 ml of solution was extracted, and bacteria were grown in the Standard Method Agar (SMA) medium overnight at 37 °C. The surviving colonies were recorded by counting the numbers of bacterial colonies on the petri dish (Petri dish 60 mm Ø; Iwaki, Japan) and multiplied by dilution factor to denote in CFU/ml.

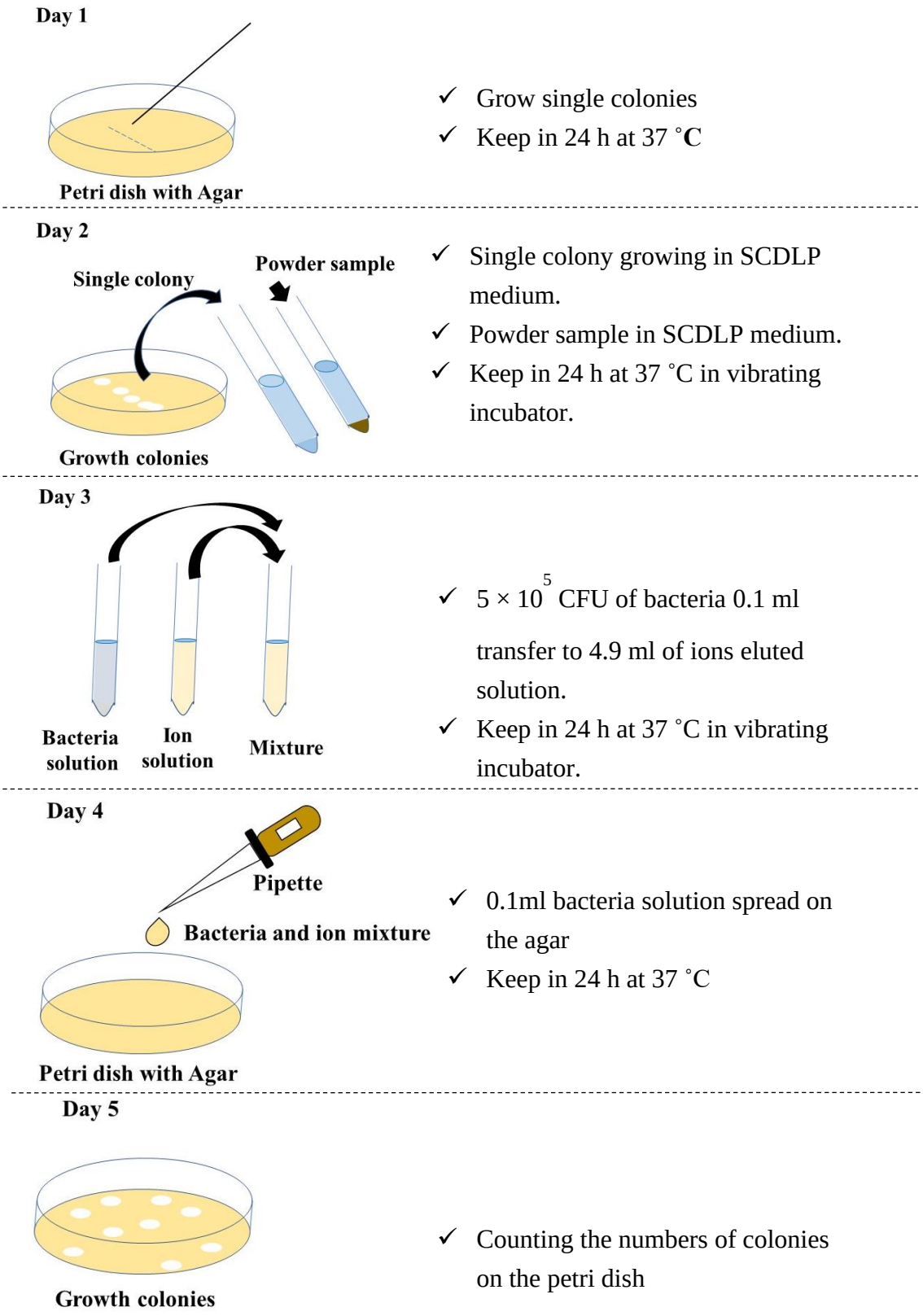

Figure 2.7: Schematic representation of colony counting method

The percentage of bacteria cell reduction (R(%)) was calculated using the following equation (Eq.1).

$$R(\%) = \frac{CFU_{control} - CFU_{sample}}{CFU_{control}} \times 100 \quad (1)$$

where $CFU_{control}$ is the number of viable colonies in the control plate (without sample) and CFU_{sample} is the number of viable colonies in the sample plate (with sample). The average value of antibacterial activity were determined by triplicate runs[11,12]. This complete experimental process will need 5 days and schematic representation of colony counting method is shown in Figure 2.7.

Inhibition zone method: The area of the inhibition zone was studied to calculate the antibacterial efficiency and to compare the activity among the different samples. In this method, the discs (specimen sized: 10 mm in diameter and 2.0 mm height) prepared by powder samples (0.3 g) were sterilized and placed over the solidified agar medium carefully. Then 1 ml of bacterial solution with initial concentration 10^6 CFU/ml was mixed with condense nutrient agar 9 ml and poured over the discs and evenly distributed. After that, solidified agar were transferred into an incubator and cultivated at 37 °C for 2 days. Then relative antibacterial activity was examined by the inhibition circle around the disk. The area of the circles were calculated using Image J software (National Institute of Health, MD) and relative inhibition zone was

calculated using the following equation (Eq. 2)

$$\text{Inhibition zone} = (A_1 - A_2)/A_2 \qquad (2)$$

Where, A_1 is area of the inhibition zone and A_2 is area of the testing disc[13]. This complete experimental process will need 5 days and 1st, 2nd days experimental method is same as in colony counting method. The 3rd and 5th day's experimental method is shown in Figure 2.8 schematic representation. The data presented in this thesis was obtained using this both experimental methods.

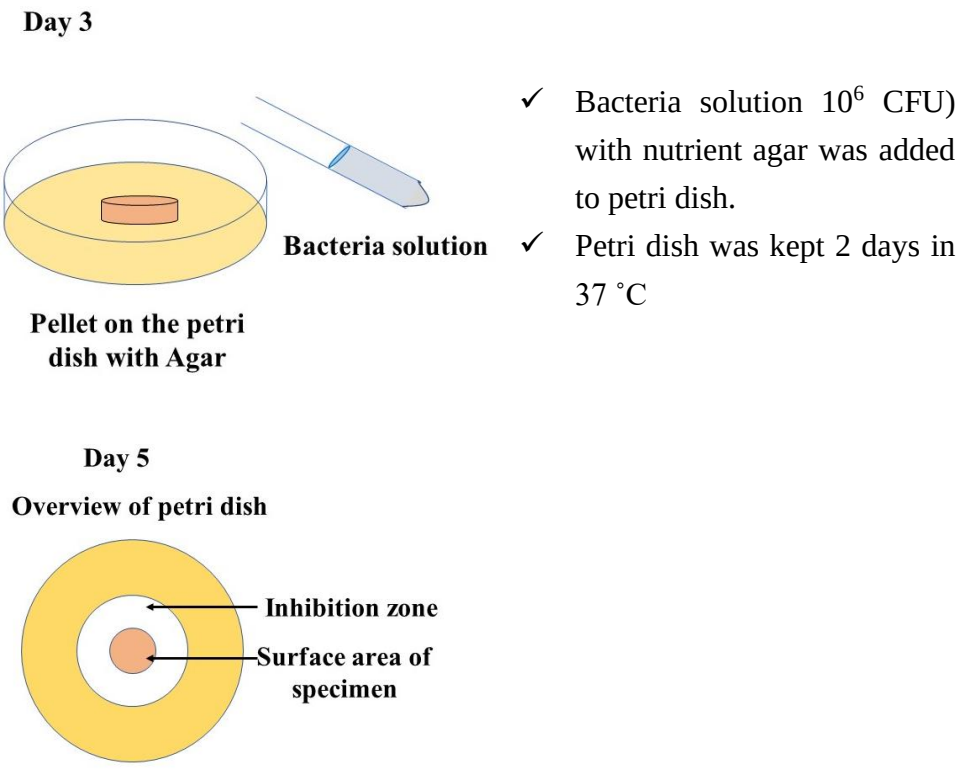

Figure 2.8: Schematic representation of Inhibition zone method

2.2.3 Ionic conductivity test

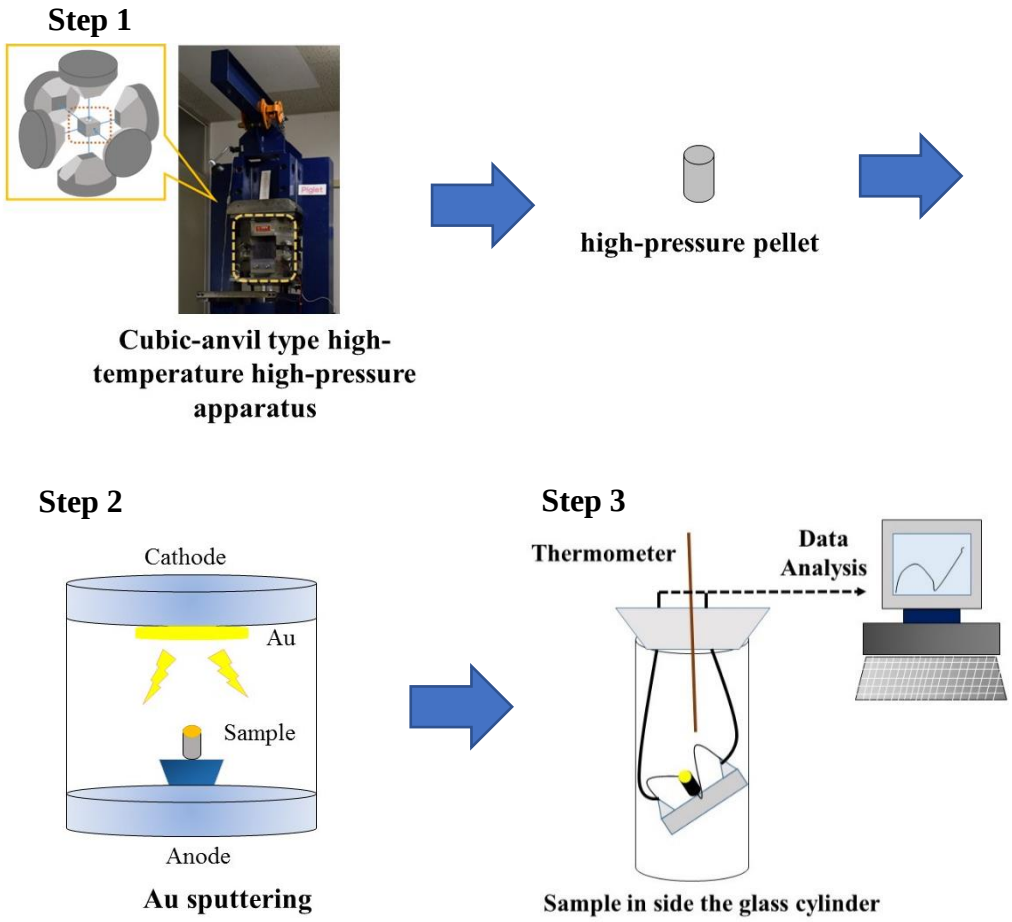

Figure 2.9: Schematic representation of impedance measurement.

As shown in Figure 2.9 the pellets (10mm diameter and 3-4mm thick) of the samples were obtained at the high pressure of 4 GPa (10 min) using a cubic-anvil-type high-temperature high-pressure apparatus. Then the electrodes were sputter-coated with gold on both sides of the pellet and connected with a platinum wire using Ag paste. The total conductivity was determined by AC impedance measurement, as a function of temperature, using an impedance analyzer (SI 1260,

Solartron) over the frequency range of 1 Hz to 10 MHz. These measurements were performed in the temperature range 25-240 °C and the stabilization time before each data point was approximately 30 min. The ZView software was used to analyze the spectra and calculate the ohmic resistance of the pellets[14].

2.3 References:

(1) Hara, T.; Yabashi, M.; Tanaka, T.; Bizen, T.; Goto, S.; Maréchal, X. M.; Seike, T.; Tamasaku, K.; Ishikawa, T.; Kitamura, H. The Brightest X-Ray Source : A Very Long Undulator at SPring-8. *Rev.Sci. Instrum.,* **2002,** 73 (3), 1125-1128 .

(2) Hiromichi, K.; 8 GeV Synchrotron Radiation Facility Project in Japan : JAERI-RIKEN SPring-8 Project. *Nucl. Instr. and Meth.,* **1991**, 303, 421–434.

(3) Takemoto, M.; Osaka, K.; Nishibori, E.; Moriyoshi, C.; Kubota, Y.; Kuroiwa, Y.; Sugimoto, K. High-Throughput Powder Diffraction Measurement System Consisting of Multiple MYTHEN Detectors at Beamline BL02B2 of SPring-8. *Rev. Sci. Instrum.,* **2017**, 88 (8), 85111-1 - 85111-9.

(4) Honma, T.; Oji, H.; Hirayama, S.; Taniguchi, Y.; Ofuchi, H.; Takagaki, M. Full-Automatic XAFS Measurement System of the Engineering Science Research II Beamline BL14B2 at SPring-8. *AIP Conferrence Proceeding.,* **2010**, 13-16.

(5) Bragg, P. W. H.; Bragg, W. L.; The reflection of X-ray by crystals. *Nature,* **1913**, 429–438.

(6) Oatley, C. W. The Early History of the Scanning Electron Microscope. *J. Appl. Phys.,* 1982, 53 (2).

(7) Fadley, C. S. X-Ray Photoelectron Spectroscopy : Progress and Perspectives. *J. Electron Spectrosc. Relat. Phenome.,* **2010**, *178–179*, 2–32.

(8) Oswald, S. X-Ray Photoelectron Spectroscopy in Analysis of Surface., *Encyclopedia of Analytical Chemistry*, **2013**.

(9) Steen, H.; Stig, P.; Knut, R.; High Performance Liquid chromatography. *Introduction to pharmaceutical chemical analysis*, **2012.**

(10) Yanagida, S.; Takei, T.; Moriyoshi, C. Hydrothermal Synthesis , Crystal Structure and Visible-Region Photocatalytic Activity of $BaBi_2O_6$. *Chemistryselect*, **2017**, 2, 4843–4846.

(11) Smetana, A. B.; Klabunde, K. J.; Marchin, G. R.; Sorensen, C. M. Biocidal Activity of Nanocrystalline Silver Powders and Particles. *Langmuir.*, **2008**, *24*(11), 7457–7464.

(12) Zeljko, R; Bojan, J.; Djordje, V.; Suzana, D. ; Vesna, K; Rada, P.; Djordje, J., Antimicrobial Activity and Biocompatibility of Ag^+ -and Cu^{2+} -Doped Biphasic Hydroxyapatite / α -Tricalcium Phosphate Obtained from Hydrothermally Synthesized Ag^+-and Cu^{2+} -Doped Hydroxyapatite., *Appl. Surf. Sci.*, **2014**, *307*, 513–519.

(13) Kakinuma, H.; Ishii, K.; Ishihama, H.; Honda, M.; Toyama, Y.; Matsumoto, M.; Aizawa, M. Antibacterial Polyetheretherketone Implants Immobilized with Silver Ions Based on Chelate-Bonding Ability of Inositol Phosphate : Processing , Material Characterization , Cytotoxicity , and Antibacterial Properties. *J. Biomed. Mater. Res.*, **2014**, 1–8.

(14) Isuru, W.; Withanage, U.; Kumada, N.; Takei, T.; Yanagida, S.; Tadanaga, K.; Miura, A.; Rosero-navarro, N. C.; Azuma, M. Electrical Properties of Pyrochlore-Type Silver Tantalate and Fluorite-Type Silver Niobate. *J. Ceram. Soc. Jpn.*, **2020**, 128 (1), 46–50.

CHAPTER 3

HYDROTHERMAL DOPING OF Ag INTO THREE TYPES OF POTASSIUM NIOBATES

3.1 Introduction

Hydrothermal method is promising and applicable method that can be used for synthesis of various oxide materials which are potential application in daily life. In this research we focused to synthesis of new niobate compounds in K_2O-Nb_2O_5-H_2O system. This system produces potassium niobates with various crystal structures such as pyrochlore-, perovskite-, layered-, or tunnel-type structures depending on the reaction conditions[1-5]. Among the various preparation methods, a hydrothermal reaction is more efficient method to produce highly crystallized fine powders and to control the morphology of the particles[4,6]. Moreover, this hydrothermal system is a promising candidate for lead-free piezomaterials, optical devices, antibacterial materials, photocatalysts, ion-exchangers, etc. These applications are derived from their various properties such as photocatalytic activity[7], ion exchange[8], ionic conductivity[9], and ferroelectricity[10]. Our group were investigating new photocatalysts based on niobates, tantalates and pentavalent bismuthates prepared by hydrothermal reactions[11]. Certain pentavalent bismuthates such as $NaBiO_3$, $LiBiO_3$,

and ABi_2O_6 (A = Sr, Ba) exhibited photocatalytic activity for phenol degradation under visible light irradiation.[12-14].

In this investigation, we attempted Ag doping of potassium niobates under hydrothermal conditions and examined their photocatalytic activities with respect to phenol degradation. Moreover, chemical environment of the Ag atoms were studied by EXAFS analysis.

3.2 Experimental section

3.2.1 Materials and Methods

Silver incorporated potassium niobates such as a pyrochlore-type $(K,H)NbO_3 \cdot nH_2O$, a layered $K_4Nb_6O_{17} \cdot nH_2O$, and a perovskite-type $KNbO_3$, were synthesized via a hydrothermal reaction using niobium pentoxide (Nb_2O_5), potassium hydroxide (KOH), and silver nitrate ($AgNO_3$) as the starting materials. All chemicals were purchased from Kanto Chemical Co. Ltd., Japan and used without further purification. As shown in Figure 3.1, the molar ratios of KOH/Nb_2O_5 = 6, 10, 40, and the reaction temperatures 220, 240, and 260 °C, were respectively changed. The molar ratio of $AgNO_3$/ Nb_2O_5 was 0.01 and Teflon-lined autoclave was

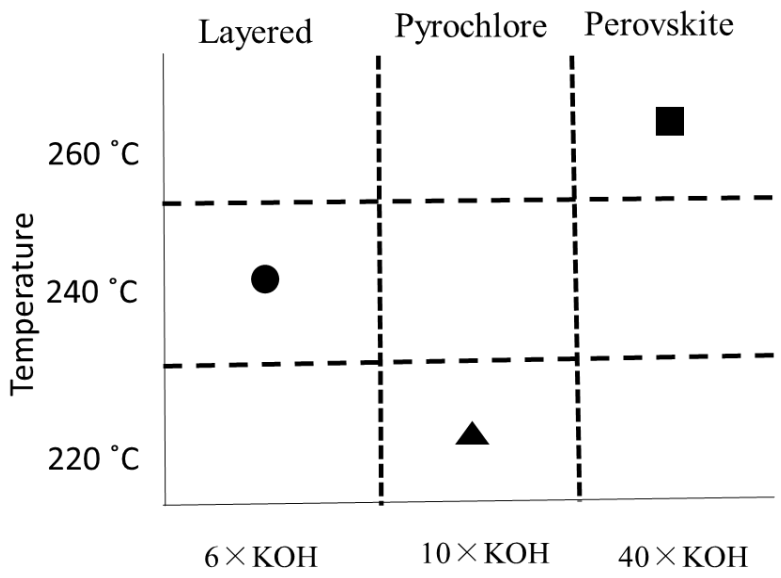

Figure 3.1: K_2O-Nb_2O_5-H_2O hydrothermal system

used for the hydrothermal reaction. After the reaction, the solid product was separated by filtration and washed with distilled water, and dried at 50 °C for 24 h. Figure 3.1 shows, summary of the K_2O-Nb_2O_5-H_2O hydrothermal system.

3.2.2 Morphological and composition Characterization

The final products were identified by X-ray diffraction (XRD), morphology and particle size of the product were observed by scanning electron microscopy (SEM). The chemical compositions were resolved by energy dispersive X-ray spectroscopy (EDX). The optical band gap was estimated using UV-visible diffuse reflectance spectroscopy (UV-Vis, JASCO V-550) and were converted using Kubelka-Munk function. The chemical environment of the doped Ag atom was studied by Extended X-ray Absorbance Fine Structure (EXAFS) measurement in the

beamline BL14B2 at the SPring-8 facility Hyogo, Japan. The photocatalytic activity was analyzed by the decomposition of a 20 ppm phenol solution as describe in chapter 2 section 2.1.1. Then the mixture was irradiated using ultraviolet light from a 300 W Xe lamp (UXR-300DU, Ushio Inc.), without any cutoff filter and phenol concentration was analyzed by HPLC (JASCO HPLC LC-2000).

3.3 Results and Discussion

3.3.1 Hydrothermal synthesis

A layered-type $K_4Nb_6O_{17}\cdot nH_2O$:Ag was prepared at 240 °C using KOH/Nb_2O_5 = 6 molar ratio and which indicates low crystallinity as shown in Figure 3.2a XRD pattern. There have been previous reports of hydrothermal synthesis of a layered-type $K_4Nb_6O_{17}\cdot nH_2O$[15-22] via homogeneous precipitation using urea and their XRD patterns were identical[16]. Previously reported pyrochlore-type $(K_{0.73}H_{0.27})NbO_3\cdot 1.72H_2O$:Ag was prepared at 220 °C using KOH/Nb_2O_5 = 10 and this compound has high crystallinity shown in Figure 3.2b,. Its lattice parameter (a = 10.6497(2) Å) was somewhat larger than that (a = 10.6409(1) Å) of the undoped compound[8]. An orthorhombic perovskite-type $KNbO_3$:Ag (Figure. 3.2c) was prepared at 260 °C using KOH/Nb_2O_5 = 40 as previously reported and their lattice

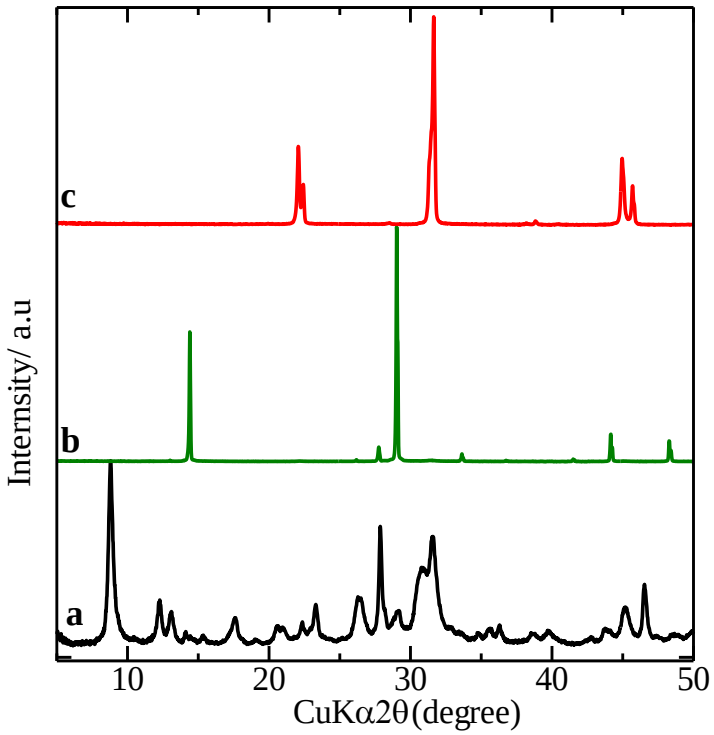

Figure 3.2: XRD patterns of (a) layered-type $K_4Nb_6O_{17}\cdot nH_2O$:Ag (b) pyrochlore-type $(K_{0.73}H_{0.27})NbO_3\cdot 1.72H_2O$: Ag (c) perovskite-type, $KNbO_3$:Ag.

parameters (a = 3.9734(1) Å, b = 5.6947(1) Å, and c = 5.7149(2) Å) agree well with previously reported data[4] (a = 3.976(2) Å, b = 5.695(4) Å, and c = 5.717(3) Å). Silver compounds such as Ag_2O or Ag are not observed in every XRD pattern. The SEM images of the three types of compound are shown in Figure 3.3 and morphology of the layered-type $K_4Nb_6O_{17}\cdot nH_2O$:Ag is an irregular-shaped aggregate of flake-like submicron-sized particles, corresponding to a layered structure. The pyrochlore-type $(K_{0.73}H_{0.27})NbO_3\cdot 1.72H_2O$:Ag has octahedral particles of ~20 μm size, and this shape comes from cubic symmetry. The orthorhombic perovskite-type $KNbO_3$:Ag

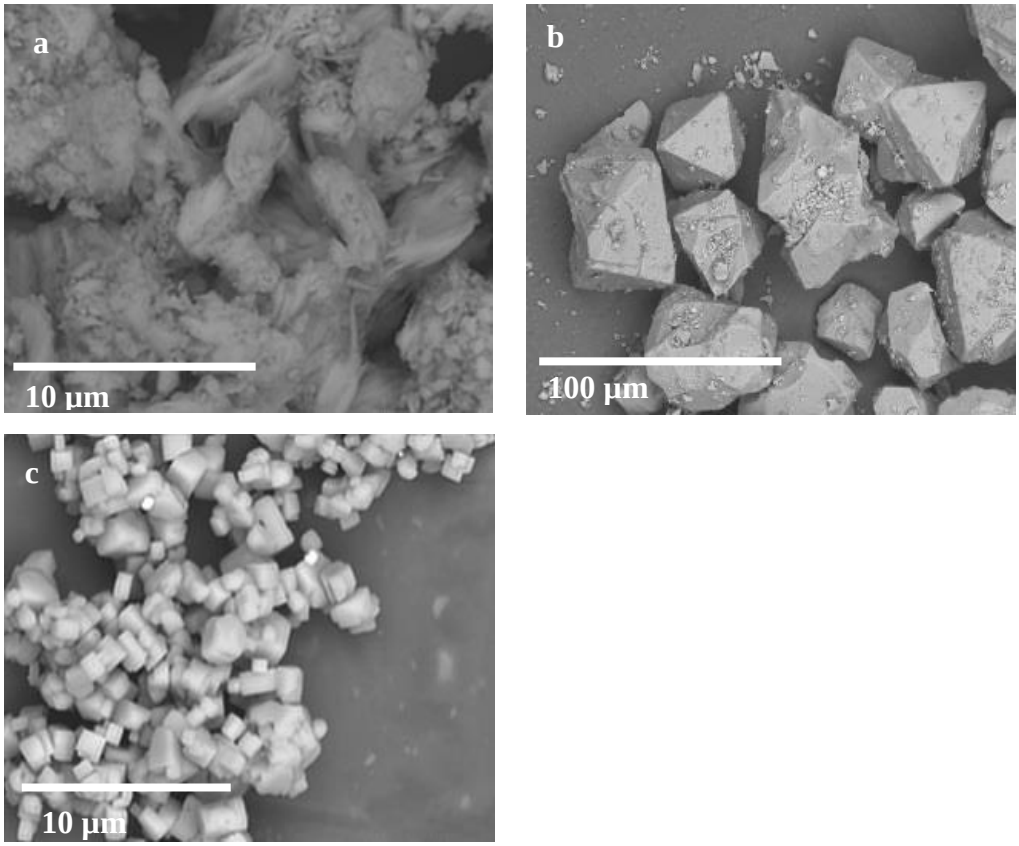

Figure 3.3: SEM images of (a) layered $K_4Nb_6O_{17}\cdot nH_2O$:Ag (b) pyrochlore-type $(K_{0.73}H_{0.27})NbO_3\cdot 1.72H_2O$: Ag (c) perovskite-type, $KNbO_3$:Ag.

has a rectangular shape with submicron-sized particles. The morphology of both the pyrochlore- and perovskite-type compounds was similar to those without doping. The EDX analysis indicated that the Ag contents of the layered-, pyrochlore-, and perovskite-type compounds were 2.7, 0.27 and 0.55 mol %, respectively.

3.3.2 EXAFS analysis

Figures 3.4 and 3.5 show Ag K-edge (XANES) spectra and radial distribution functions (RDF) for hydrothermal products incorporated with Ag, and with Ag_2O

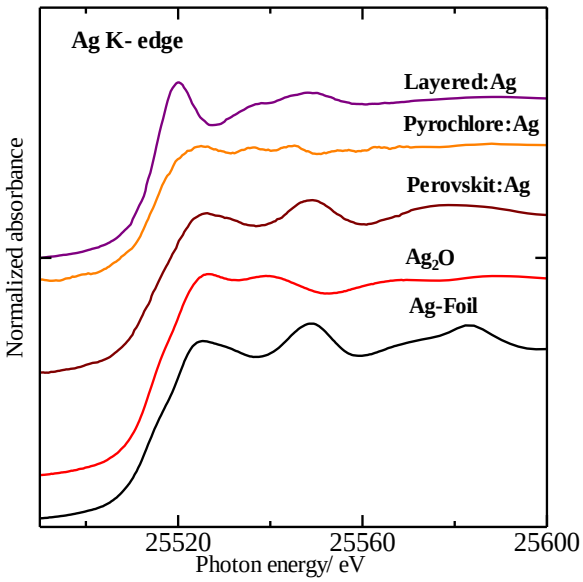

Figure 3.4: Ag K-edge XANE spectra of layered-, pyrochlore-, perovskite samples with reference Ag_2O and Ag-foil

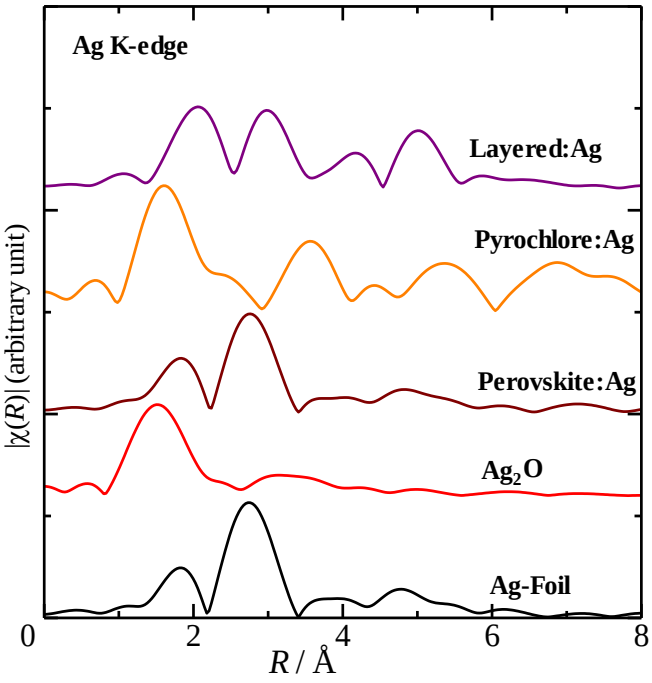

Figure 3.5: Radial distribution function of layered, pyrochlore, and perovskite samples with reference Ag_2O and Ag-foil.

and Ag metal as reference. There are two types of local environments for the Ag atom in a layered-type $K_4Nb_6O_{17}\cdot nH_2O$:Ag, and these are different from those for the reference Ag_2O and Ag metal. The layered sheets are stacked along the b-axis of an orthorhombic unit cell to two types of interlayer regions which are denoted by I and II. These two interlayers have different ion-exchange capabilities in which interlayer I is hydrated and can be exchanged with mono or bivalent cations (Li^+, Ca^{2+}, Na^+, and Ni^{2+}), while interlayer II is not hydrated and only monovalent cations can be exchanged[22]. Both interlayer regions I and II have ion-exchanged capability with monovalent cations. Therefore we suggest that Ag atoms are incorporated in both interlayers during the hydrothermal conditions. The RDF of pyrochlore-type compound shows two peaks with around 1.8 and 3.5 Å and which is suggests that Ag^+ ions do not have a linear coordination like Ag_2O but are sited in the tunnel of the pyrochlore-type structure. The XAFES spectra of the layered- and pyrochlore-type compounds are similar to that of Ag_2O and this result suggests that the silvers in the layered- and pyrochlore-type compounds are monovalent. On the other hand, the XANES spectra and RDF for perovskite-type $KNbO_3$:Ag agree with those of the Ag metal. From this result it is hypothesized that in this compound, Ag atoms exist on the surface as Ag metal. The reason for using the Ag metal for doping the

perovskite-type compounds with Ag atoms may be explained by the hydrothermal condition and the crystal structure. The perovskite-type phase was prepared using a higher KOH concentration and a higher reaction temperature than those of the other phases. Such severe hydrothermal conditions would accelerate the reduction of the Ag^{+} ions. Moreover, there are no ion-exchangeable sites in the perovskite-type structure, while the other crystal structures have ion-exchangeable sites.

3.3.3 Photocatalytic activity

Figure 3.6 shows the UV-vis spectra and a Tauc plot for the Ag-incorporated hydrothermal products on the assumption that indirect transition occurs. The optical band gap energies for layered-, pyrochlore-, and perovskite-type compounds doped with Ag are estimated to be 3.1, 3.0, and 3.1 eV, respectively. Figure 3.7 shows the time dependence of phenol degradation for the Ag-doped and undoped layered-, pyrochlore-, and perovskite-type compounds under UV light irradiation. The photocatalytic activity of the layered-type Ag-doped compound is comparable with that of the perovskite-type compound, and superior to that of the pyrochlore-type compound. Although the photocatalytic activities of the pyrochlore- and perovskite-type compounds are improved by Ag-doping, the degradation rate of the layered-type compound is lower than that of the undoped compound. These results might be

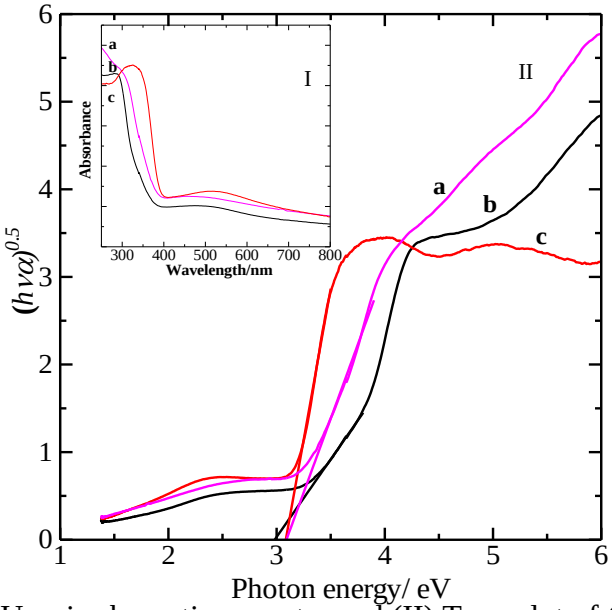

Figure. 3.6: (I) Uv-vis absorption spectra and (II) Tauc plot of (a) layered, (b) pyrochlore and (c) perovskite samples.

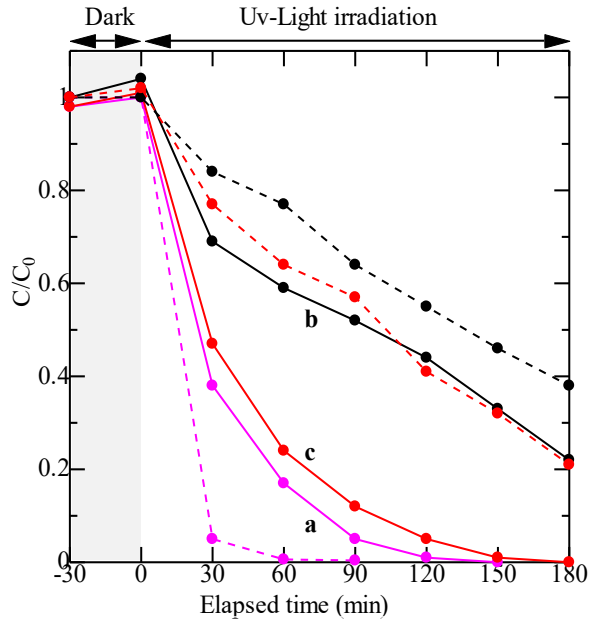

Figure 3.7: Photocatalytic activity of (a, pink) layered, (b, black) pyrochlore and (c, red) perovskite samples. Solid and dash line denoted Ag doped and undoped samples respectively.

explained by the different local environments of the Ag atoms observed by EXAFS analysis. The high photocatalytic activity of perovskite-type compounds is assumed to be caused by the presence of the metals, which acts as a promoter on the surface. In the case of the layered-type compound, the Ag ions are incorporated into both interlayer spaces I and II, which have been reported to work effectively for photocatalytic activity[23]. In this case, however, the interlayered Ag^+ ions may act as electron-hole recombination centers to inhibit photocatalytic activity. The poor photocatalytic activity of the pyrochlore-type compound is consistent with the poor property of the fluorite-type $Ag_{0.41}Nb_{0.59}O_{1.68}$[8]. This could result from the structural similarity between the pyrochlore- and fluorite-type structures. On the other hand, a pyrochlore-type silver tantalate exhibited good photocatalytic activity[8]. The difference in the photocatalytic activity between niobate and tantalate may be clarified by the synthesis of a fluorite-type silver tantalate, which, however, is yet to be achieved.

3.4 Conclusions

Ag incorporation into layered-, pyrochlore-, and perovskite-type potassium niobate was successfully achieved via a hydrothermal reaction. In the layered-type compound, Ag^+ ions were incorporated into both interlayer spaces and which is

confirmed by EXAFS analysis. The pyrochlore-type compound accommodated Ag^+ ions in the tunnel while silver metal was loaded on the surface of the perovskite-type compound during the hydrothermal reaction. Photocatalytic activity of the layered-type and perovskite-type compounds doped with Ag were observed to be superior to that of the pyrochlore-type compound.

3.5 References

(1) A. Magrez.; E. Vasco.; J.W. Seo.; C. Dicker.; N. Setter.; L. Forró, Growth of Single-Crystalline $KNbO_3$ Nanostructures. *J. Phys. Chem. B.*, **2006,** 110**,** 58-61.

(2) Y. Hu.; H. Gu.; Z. Hu.; W. Di.; Y. Yuan.; J. You.; W. Cao.; Y. Wang.; H. L. W. Chan, Controllable Hydrothermal Synthesis of $KTa_{1-x}Nb_xO_3$ Nanostructures with Various Morphologies and Their Growth Mechanisms. *Cryst. Growth Des.*, **2008,** 8, 832–837.

(3) J. Wu.; C. Zhou.; Y. Zhao.; L. Shang.; T. Bian.; L. Shao.; F. Shi.; L.Z. Wu.; C.H Tung.; T. Zhang, One-Pot Hydrothermal Synthesis and Photocatalytic Hydrogen Evolution of Pyrochlore Type $K_2Nb_2O_6$. *Chinese J. Chem.*, **2014**, 32, 485–490.

(4) N. Kumada.; T. Kyoda.; Y. Yonesaki.; T. Takei.; N. Kinimura, Preparation of $KNbO_3$ by Hydrothermal Reaction. *Mater. Res. Bull.*, **2007,** 42, 1856-1862.

(5) O. Smirnova.; N. Kumada.; T. Takei.; Y. Yonesaki.; M. Yashima.; N. Kinomura, Structure and Electrical Properties of the New Pyrochlore-type Protonic Solid Electrolyte $K_{0.88}Nb_2O_{7.58}H_{4.28}$**.** *Acta Crsyt. B.*, **2010**, 66, 594–602.

(6) Y. Wang.; Z. Yi.; Y. Li.; Q. Yang.; D. Wang.; Hydrothermal Synthesis of Potassium Niobate Powders, *Ceram. Int.*, **2007**, 33, 1611–1615.

(7) Q.P. Ding.; Y.-P. Yuan.; X. Xiong.; R.-P. Li.; H.-B. Huang.; Z.-S. Li.; T. Yu.; Z.-G. Zou.; S.-G Yang, Enhanced Photocatalytic Water Splitting Properties of KNbO3 Nanowires Synthesized through Hydrothermal Method. *J. Phys. Chem. C.*, **2008**, 112, 18846–18848 (2008).

(8) I. Withanage.; N. Kumada.; T. Takei.; S. Yanagida.; Y. Kuroiwa.; C. Moriyoshi.; Synthesis and Crystal Structure of pyrochlore-type silver niobate and tantalate. *J. Ceram. Soc. Jpn.*, **2017**, 125, 776–778.

(9) O. Smirnova.; N. Kumada.; Y. Yonesaki.; N. Kinomura, A new solid electrolyte to fill the gap between low temperatures and high temperatures SOFC materials?. *Electrochem. Commun.*, **2008,** 10, 485–487.

(10) S. Pattanayak.; R.N.P. Choudhary.; P.R. Das, Effect of $KNbO_3$ modification on structural, electrical and magnetic properties of $BiFeO_3$, *Electron. Mater. Lett.*, **2014**, 10, 165–172.

(11) N. Kumada, Preparation and crystal structure of new inorganic compounds by hydrothermal reaction. *J. Ceram. Soc. Jpn.*, **2013**, 135–141.

(12) N. Kumada.; T. Takei.; R. Haramoto.; Y. Yonesaki.; Q. Dong.; N. Kinomura.; S. Nishimoto.; Y. Kameshima.; M. Miyake, *Mater. Res. Bull.*, **2011**, 46**,** 962-965.

(13) T. Takei.; R. Haramoto.; Q. Dong.; N. Kumada.; Y. Yonesaki.; N. Kinomura.; T. Mano.; S. Nishimoto.; Y. Kameshima.; M. Miyake, Hydrothermal Synthesis of $NaNbO_3$—morphology Change by Starting Compounds. *J. Solid State Chem.*, **2011**, 184, 2017-2022.

(14) M. Saiduzaman.; S. Yanagida.; T. Takei.; C. Moriyoshi.; Y. Kuroiwa.; N. Kumada, Hydrothermal Synthesis, Crystal Structure, and Visible-Region Photocatalytic Activity of $BaBi_2O_6$. *Chem. Select.*, **2017,** 2, 4843-4846.

(15) S. Uchida.; Y. Inoue.; Y. Fujishiro.; T. Sato, Hydrothermal synthesis of $K_4Nb_6O_{17}$. *J. Mater. Sci.*, **1998,** 33, 5125-5129.

(16) Y. Cao.; L. Jiang.; H. Guo.; Q. Zheng, Nano-layered $K_4Nb_6O_{17}$ as an Efficient Photocatalyst for Methyl Orange Degradation: Influence of Solution pH and Surface-Dispersed Gold Nanoparticles *J. Mol. Catal. A.*, **2014**, 383-384, 209-216.

(17) G. Zhang.; F. He.; X. Zou.; J. Gong.; H. Zhang, Hydrothermal Preparation and Photocatalytic Properties of Sheet-like Nanometer Niobate $K_4Nb_6O_{17}$, *J. Phys. Chem. Solids.*, **2008,** 69**,** 1471-1474.

(18) W. Qu.; F. Chen.; B. Zhao.; J. Zhang, Preparation and Visible Light Photocatalytic Performance of Methylene Blue Intercalated $K_4Nb_6O_{17}$**.** *J. Phys. Chem. Solids.*, **2010,** 71, 35-41.

(19) W. Cui.; H. Wang.; Y. Liang.; L. Liu.; B. Han, Preparation of Ag@AgI-Intercalated $K_4Nb_6O_{17}$ Composite and Enhanced Photocatalytic Degradation of Rhodamine B under visible light**.** *Catal. Commun.,* **2013**, 36, 71-74.

(20) C. Zhou.; G. Chen.; Q. Wang, High Photocatalytic Activity of Porous $K_4Nb_6O_{17}$ Microsphere with Large Surface Area Prepared by Homogeneous Precipitation Using Urea**.** *J. Mol. Catal. A*, **2011,** 339**,** 37-42 (2011).

(21) Q. Deng.; M. Li.; J. Wang.; P. Zhang.; K. Jiang.; J. Zhang.; Z. Hu.; J. Chu, Exploring Optoelectronic Properties and Mechanisms of Layered Ferroelectric $K_4Nb_6O_{17}$ Nanocrystalline Films and Nanolaminas**.** *Sci. Rep.,* **2017**, 1883, 1-13.

(22) N. Kinomura.; N. Kumada.; F. Muto, Ion exchange of $K_4Nb_6O_{17}\cdot 3H_2O$. *J. Chem. Soc. Dalt. Trans.*, **1985,** 2349–2351 .

(23) K. Domen.; A. Kudo.; M. Shibata.; A. Tanaka.; K.-I. Maruya.; T. Onishi, Novel Photocatalysts, Ion-Exchanged $K_4Nb_6O_{17}$, with a Layer Structure**.** *J. Chem. Soc. Chem. Commun*., 1986, 1706-1707.

CHAPTER 4

SYNTHESIS, CRYSTAL STRUCTURE AND ELECTRICAL PROPERTIES OF PYROCHLORE-TYPE SILVER TANTALATE AND FLUORITE-TYPE SILVER NIOBATE

4.1 Introduction

Chapter 3 discussed the K_2O-Nb_2O_5-H_2O system and synthesis condition for pyrochlore-, perovskite- and layered-type structures. Figure 4.1 shows the synthesis condition of the niobate in hydrothermal system. Moreover, chapter 3 discussed about the improvement of the catalytic activity of silver ion incorporation towards the phenol degradation experiments. It was shown that the silver ion doped into pyrochlore structure could be tuned the structure of the niobate phase. This chapter outlines the improvement of the photocatalytic activity of the pyrochlore-

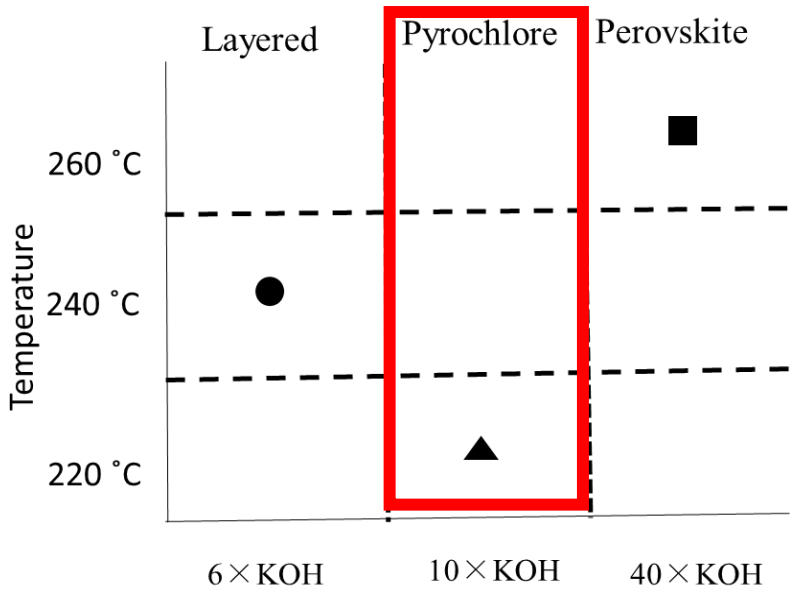

Figure 4.1: K_2O-Nb_2O_5-H_2O hydrothermal system

type niobate and tantalate phase by ion-exchanged with excess $AgNO_3$ and investigated the electrical properties of the ion-exchanged samples.

Pyrochlore-type compound shows various chemical and physical properties such as ferroelectricity, ion-exchange, ionic conductivity, antibacterial, optical devices and photocatalytic properties[1,2]. This pyrochlore group can be categorized in several structural groups; (i) AB_2O_6, with cation A in 8b sites; (ii) classic $A_2B_2O_7$, (iii) defect $A_2B_2O_6$, and (iv) hydrated $A_2B_2O_6$. nH_2O, here A atom is generally alkaline metals, alkaline earth metals or rare earth metals, and B atom is transition metals[3]. The cubic crystal structure has to the space group of *Fd*-3*m* with $z = 8$ and two distinct oxygen atoms are found in different sites. The oxygen atoms on the 48f sites, are bounded tetrahedrally to two A (16*d* site) and two B (16*c* site) ions and the oxygen atoms on 8a sites are bounded tetrahedrally to four A ions[4]. The discovery of photocatalytic activity in layered $K_4Nb_6O_{17}\cdot nH_2O$ was initiated the research in photocatalytic water splitting while pyrochlore-type $K_2Nb_2O_6$ was the first example of the photocatalytic activity for pyrochlore-type niobates[5–8]. Our group has prepared a variety of pyrochlore-type compounds by a hydrothermal reaction, alkaline niobate[1] and tantalate[9], alkaline earth bismuthates and sodium bismuth titanate[3]. In this chapter we will describe the ion-exchange reaction of pyrochlore-type

$(A.H)MO_3 \cdot nH_2O$ with Ag^+ ion and photocatalytic activity were investigated by phenol degradation experiments. Moreover silver ion exchanged samples were used for investigate the ionic conductivity by AC impedance measurements as a function of temperature.

4.2 Experimental Section

4.2.1 Materials and Methods

Pyrochlore-type $(K_{0.73}H_{0.27})NbO_3 \cdot 1.72H_2O$ and $(K_{0.56}H_{0.44})\ TaO_3 \cdot 1.14H_2O$ were synthesized by hydrothermal reaction. The 5 g of Nb_2O_5 was put in to Teflon lined autoclave with 30 ml 4 M KOH solution and autoclave was heated up to 220 ^oC for 2 days. In the case of $(K_{0.56}H_{0.44})TaO_3 \cdot 1.14H_2O$, amorphous Ta_2O_5 was used as starting material and reacted with 20 ml of 4 M KOH at 200 ^oC for 2 days. The final product was filtered and washed with distilled water. The successfully prepared samples were dried at 60 ^oC for 24 h. In order to performed ion-exchanged reactions, both niobate and tantalate compounds were mixed with excess amount of $AgNO_3$ and the mixtures were heated at 300 ^oC for 6 h. The final products were filtered and washed certain times with distilled water and dried 60 ^oC for 24 h.

4.2.2 Morphological and composition Characterization

The products were identified by powder X-ray diffractometer (RINT-2000, Rigaku) with Cu Kα radiation. The crystal structure was refined by Rietveld method using SPring-8 (beamline; BL02B2) synchrotron X-ray powder diffraction data with wavelength λ = 0.496071 Å (1 Å = 0.1 nm), and the samples were loaded in a quartz capillary with a 0.2 mm diameter. The RIETAN-FP[10] computer program was used for crystal structure refinement and structures were drown by VESTA software package[11]. The chemical compositions of the samples were examined by Energy Dispersive X-ray spectroscopy (EDX) and UV-Vis diffuse reflection spectra (UV-Vis) (JASCO V-550) were recorded and converted to reflection to absorbance by the Kubelka-Munk method. Thermal stability of the samples was determined by TG-DTA and morphology of the samples were observed by a scanning electron microscopy (SEM). The photocatalytic activities were analyzed by decomposition of a 20 ppm phenol solution, under UV light irradiation as explain in chapter 2 section 2.1.1 and time dependent phenol concentration was examined by liquid chromatography (JASCO LC-2000). To measure the total conductivity, pellets (10 mm diameter and 3-4 mm thick) of the pyrochlore and fluorite compounds were obtained at the high pressure of 4 GPa (10 min) using a cubic-anvil-type high-

temperature high-pressure apparatus. The total conductivity was determined by AC impedance measurement, as a function of temperature, using an impedance analyzer (SI 1260, Solartron) over the frequency range of 1 Hz to 10 MHz as explain in chapter 2 section 2.2.3. The ZView software was used to analyze the spectra and calculate the ohmic resistance of the pellets.

4.3 Results and Discussion.

4.3.1 Material characterization.

Single phase pyrochlore-type $(K_{0.73}H_{0.27})NbO_3 \cdot 1.72H_2O$ and $(K_{0.56}H_{0.44})TaO_3 \cdot 1.14H_2O$ were obtained by hydrothermal reaction with the space group *Fd*-3*m*. The crystal structure refinements were successful and the *R*-factors were R_{wp}=5.27% , R_p=2.44% for niobate and R_{wp}=4.74%, R_p=3.71% for tantalate respectively. The lattice parameters were determined to be 10.6409(2) Å for niobate and a=10.571(2) Å for tantalate. The chemical compositions of $(K_{0.73}H_{0.27})NbO_3 \cdot 1.72H_2O$ and $(K_{0.56}H_{0.44})TaO_3 \cdot 1.14H_2O$ were determined by EDX and the weight loss of TG curve. Both parent compounds have octahedral shape as shown in SEM photographs (Figure. 4.2a and 4.2c) and the size of octahedral particle of niobate is larger than that of tantalate. The reaction of $(K_{0.73}H_{0.27})NbO_3 \cdot 1.72H_2O$ with excess amount of $AgNO_3$ yielded a fluorite-type compound in which the molar

ratio of Ag/Nb was 0.69 : 1.0 and the amount of K^+ ion was less than 0.02. The crystal structure refinement of this fluorite-type with the assumption of the space group Fm-3m (#225) led to reasonable *R*-factors values, R_{wp} = 5.18% and R_p = 3.34% and the lattice parameter was 5.286(3) Å. Figure 4.3a shows the Rietveld refinement profile and crystal structure of the fluorite-type $Ag_{0.41}Nb_{0.59}O_{1.68}$ (AN). The crystal data and structural parameters are listed in Table 4.1. In this structure the O atom is statistically distributed at the 8g position and those positions are intermediate space.

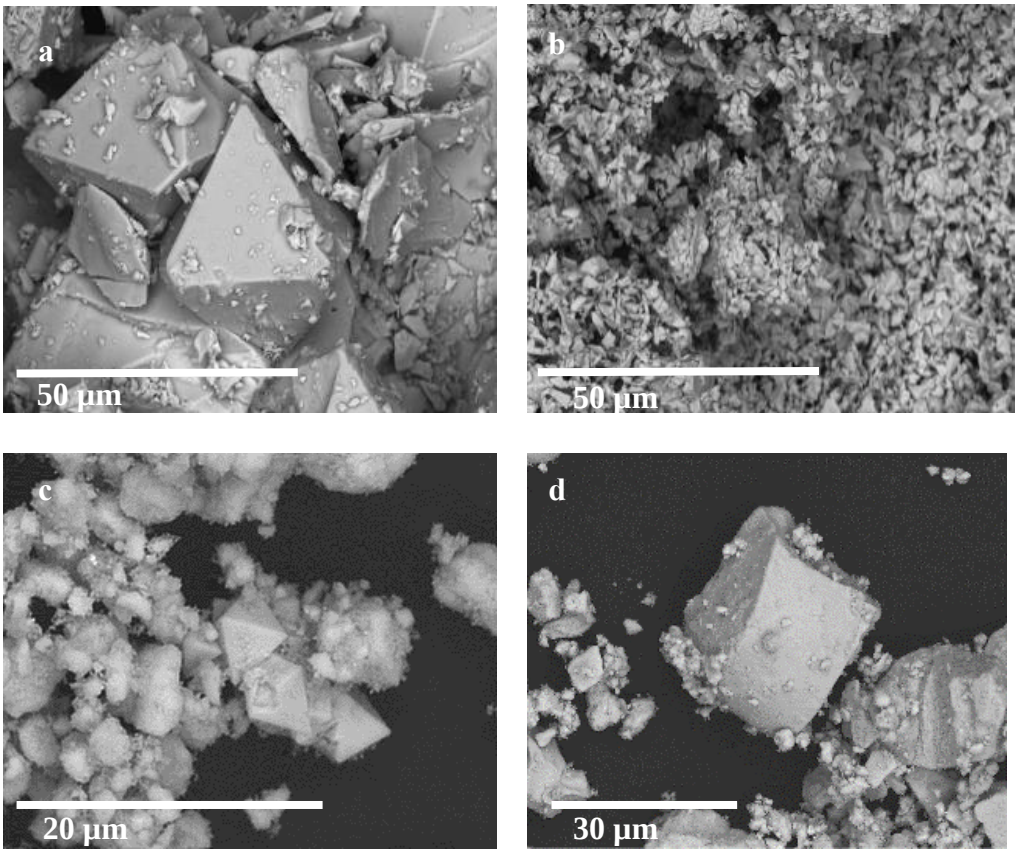

Figure 4.2: SEM photograph of (a) $(K_{0.73}H_{0.27})NbO_3 \cdot 0.83H_2O$, (b) $Ag_{0.41}Nb_{0.59}O_{1.68}$ (c) $(K_{0.56}H_{0.44})TaO_3 \cdot 1.14H_2O$ and (d) $Ag_{0.93}TaO_{2.97} \cdot 0.94H_2O$.

The uniform fine particle (1-5 µm) of this compound is observed as shown in Figure 4.2b and the morphology of the parent compound was drastically changed. The structural and morphological change from pyrochlore to fluorite-type suggests that this reaction is not an ion-exchange reaction. The pyrochlore-type structure forms a link between the defect fluorite-type structures and this means that the pyrochlore-

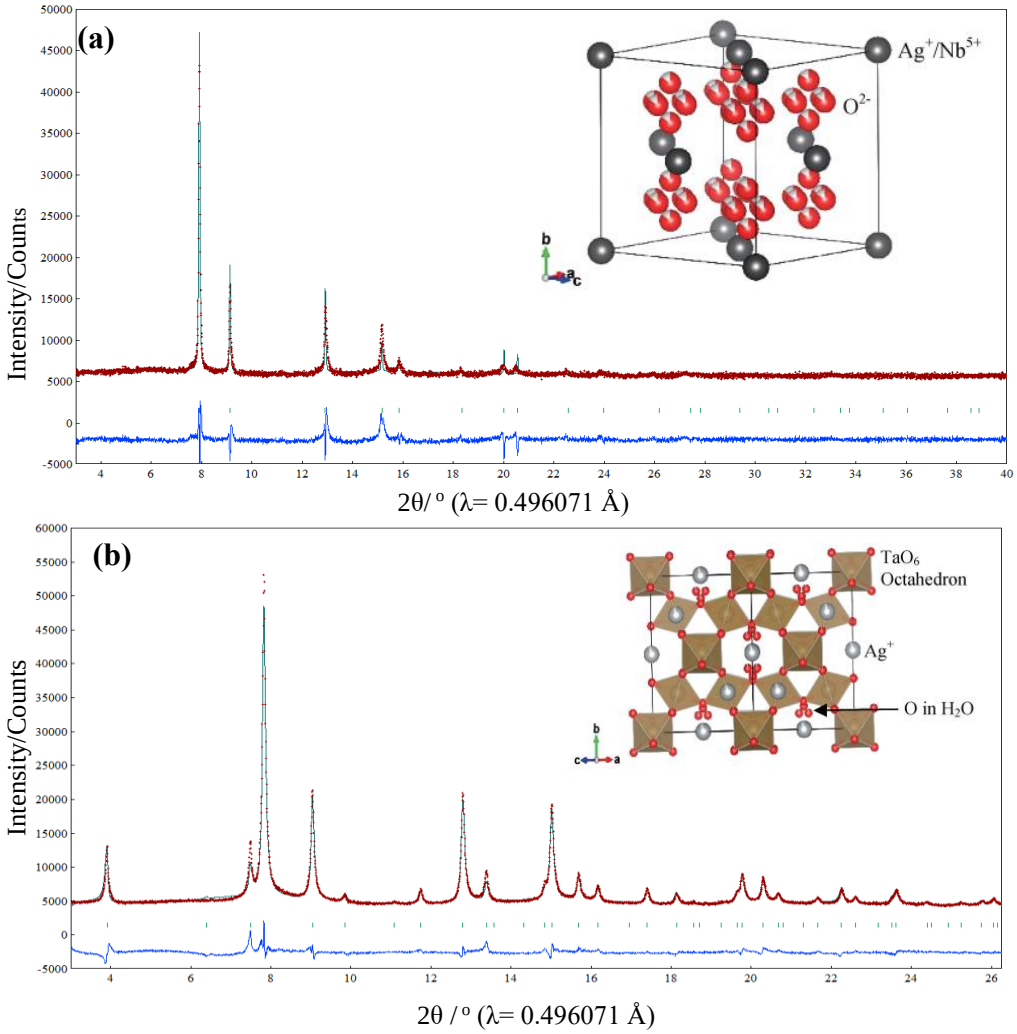

Figure 4.3: Rietveld refinement pattern of the synchrotron powder diffraction data for (a) $Ag_{0.41}Nb_{0.59}O_{1.68}$ and (b) $Ag_{0.93}TaO_{2.97}\cdot 0.94H_2O$

type structure is easily changed to the fluorite-type one. Previous studies also shown that, ordered pyrochlore structure ($A_2B_2O_7$) can be transformed into the disordered fluorite structure by changing the radius ratio (r_A/r_B) and relative stability range of pyrochlore structure from 1.46 to 1.78 (r_{K+} = 1.64 Å, r_{Ag+} = 1.28 Å, r_{Nb5+} = 0.64 Å r_{Ta5+} = 0.64 Å)[12,13]. The fluorite-type compound has transformed to the perovskite-type structure at 550°C, indicating the exothermic peak in the DTA curve.

In the case of a tantalate a single phase of a pyrochlore-type compound was yielded, and the chemical formula was found to be $Ag_{0.93}TaO_{2.97}\cdot 0.94H_2O$ (AT) from EDX and the weight loss of TG curve. The Ag/Ta molar ratio was found to be as 0.93 : 1 and the amount of K^+ was lower than 0.03. The Rietveld refinement of this compound shows to reasonable *R*-factors values, R_{wp} = 4.53% and R_p = 3.37% and the lattice parameter was 10.4509 (3) Å. Figure 4.3b shows the Rietveld refinement profile and crystal structure of the pyrochlore-type $Ag_{0.93}TaO_{2.97}\cdot 0.94H_2O$. The structural parameters and crystal data are listed in Table 4.2. The octahedral shape of parent compound is maintained during ion-exchange reaction as shown in Figure. 4.2d. The absence of a morphology change propose that this reaction is an ion-exchange

reaction. This pyrochlore-type compounds change to the perovskite-type structure at 600 °C like the case of niobate.

Table 4.1: Crystallographic data and atomic parameters of $Ag_{0.41}Nb_{0.59}O_{1.68}$ (AN).

			$Ag_{0.41}Nb_{0.59}O_{1.68}$			
Space group			*Fm*-3*m* (#225)			
a (Å)			5.286(3)			
Cell Volume (Å^3)			147.7(1)			
z			4			
R-factors			R_{wp}=5.18% R_p=3.34%			
Atomic parameters						
Atom	Site	g	x	y	z	*B* (Å^2)
Ag/Nb	4a	1	0	0	0	5.3(1)
O	48g	0.805	0.352(1)	1/4	1/4	1.5*

Table 4.2: Crystallographic data and atomic parameters of $Ag_{0.93}TaO_{2.96}\cdot 0.94H_2O$ (AT).

			$Ag_{0.93}TaO_{2.97}\cdot 0.94H_2O$			
Space group			*Fd*-3*m* (#227)			
a (Å)			10.4500(3)			
Cell Volume (Å^3)			1141.17(6)			
z			16			
R-factor			R_{wp}=4.11% R_p=2.94%			
Atomic parameters						
Atom	Site	g	x	y	z	*B* (Å^2)
Ta	16c	1.000	0	0	0	1.1(1)
Ag	16d	0.920	1/2	1/2	1/2	6.0(2)
O1	48f	0.988	0.331(1)	1/8	1/8	1.5*
O2	32e	0.940	0.352(1)	= x	= x	1.0(4)

*: Fixed parameter

4.3.2 Photocatalytic activity

Figure. 4.4a shows optical adsorption of parent compounds and reacted compounds. The band-gap energy was estimated from the dependence of $(h\upsilon\alpha)^{0.5}$ vs energy ($h\upsilon$) on a Tauc plot, on the assumption of indirect transitions.

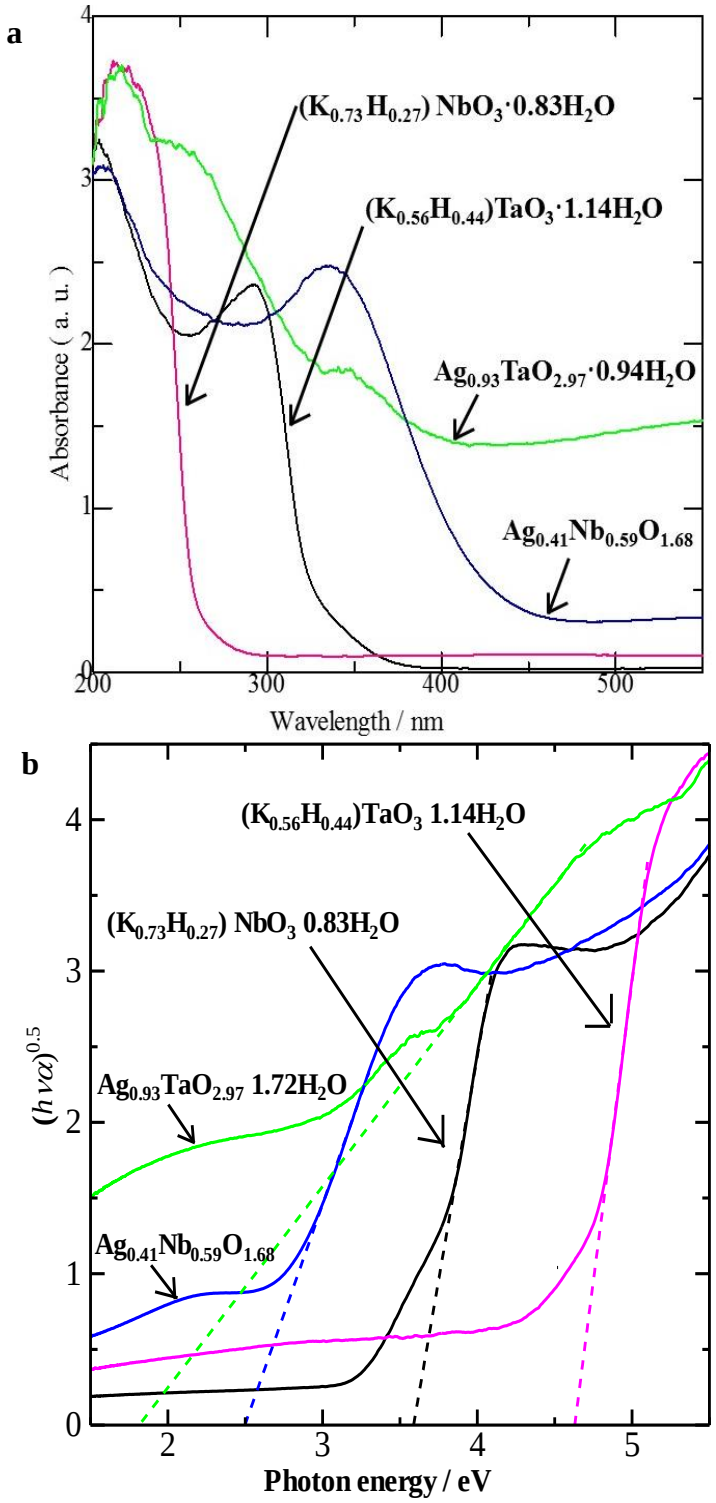

Figure 4.4: Uv-vis absorption spectra (a) and Tauc plot for the estimation (b) for $(K_{0.73}\ H_{0.27})\ NbO_3{\cdot}0.83H_2O$, $(K_{0.56}H_{0.44})TaO_3{\cdot}1.14H_2O$, $Ag_{0.41}Nb_{0.59}O_{1.68}$, and $(K_{0.73}\,H_{0.27})\ NbO_3{\cdot}0.83H_2O$

The band- gap energy of these compounds are shown in Figure 4.4b. Incorporation of Ag^{+} ion decreases band gap energy from 3.6 to 2.5 eV for a niobate and from 4.6 to 1.8 eV for tantalate. Among these samples, only the pyrochlore-type $Ag_{0.93}TaO_{2.97}\cdot 0.94H_2O$ exhibited photocatalytic activity of phenol degradation under UV light irradiation as shown in Figure 4.5. However, under visible light irradiation no compounds indicated photocatalytic activity of phenol degradation. Although Wu *et al.* reported photocatalytic activity of $K_2Nb_2O_6$ with pyrochlore-type structure, the pyrochlore-type $(K_{0.73}H_{0.27})NbO_3\cdot 0.83H_2O$ did not show good photocatalytic

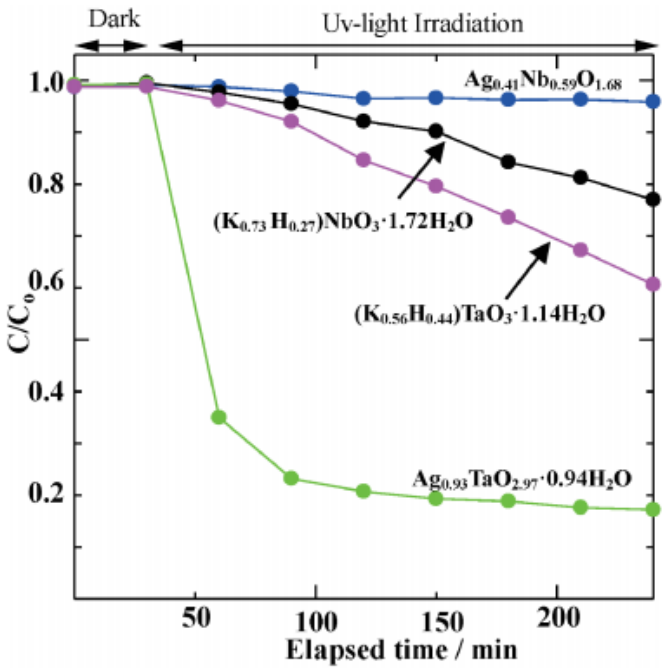

Figure 4.5: Photocatalytic activity of $(K_{0.73}H_{0.27})NbO_3\cdot 1.72H_2O$, $(K_{0.56}H_{0.44})TaO_3\cdot 1.14H_2O$, $Ag_{0.41}Nb_{0.59}O_{1.68}$, and $Ag_{0.93}TaO_{2.97}\cdot 0.94H_2O$

activity. This difference might be due to the difference of the chemical compositions.

4.4 Total conductivity of silver tanatalate (AT) and silver niobate (AN)

After the finding of the superionic conductivity of AgI-containing solid electrolytes, the ionic conductivities of Ag-based compounds have been extensively investigated[14]. AgI shows temperature-dependent structural transitions; at low temperatures (147 °C) β/γ-AgI transform to α-AgI, owing to the fast-ion conductivity[15]. However, its application as a solid electrolyte is restricted by its low ionic conductivity at room temperature. To ensure its technical applicability, a solid electrolyte must show high ion-mobility at low temperatures. The tunnel type structure of the pyrochlore compound and the related fluorite structure provide the possibility of diffusion pathways for the silver ions

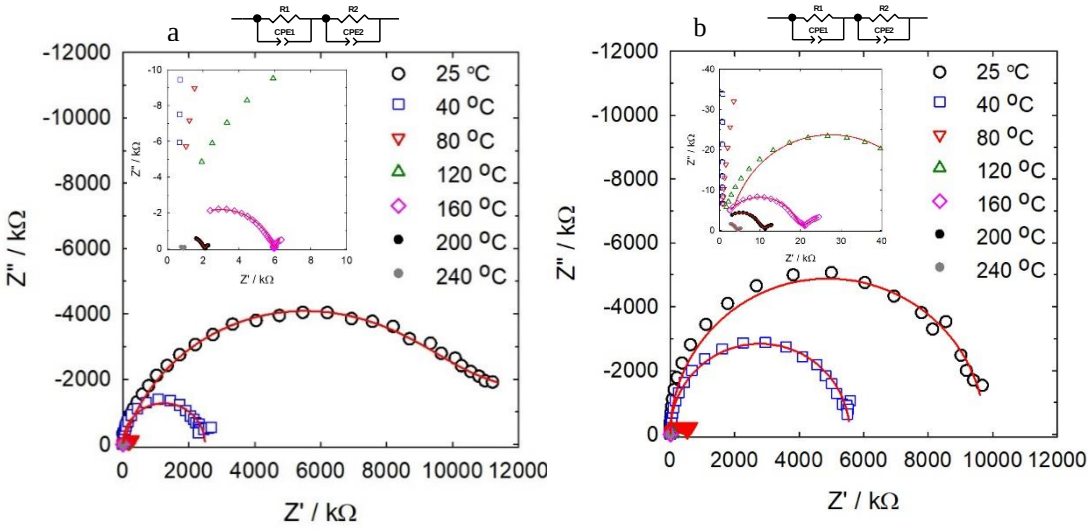

Figure 4.6: Nyquist plot of (a) AT (b) AN

migration, facilitating the ionic conductivity. Therefore, ionic conductivity of the samples were investigated by AC impedance mesurements. Impedance spectra give, primarily, the AC impedance of the sample. Charge accumulation can take place within the interfaces or at the bulk, in grain boundaries. Therefore, these crystalline samples are generally analogous to a series of two RC-parallel circuits. The overall representation of the AC impedance of AT and AN is provided from grains and grain-boundaries, as prposed by the Nyquist plot shown in Figure 4.6. The first semi-circle shows the total conductivity of the sample and intercept of the first semicircle with the real axis gives the total contributed resistance (R). Here we consider the total resistance as the present from grains and grain-boundaries. The total conductivities of AT and AN reached 4.00×10^{-3} and 9.03×10^{-4} S/cm, respectively, at 240 °C. As shown in Figure 4.7, the activation energy of AT was 0.61 eV and AN showed nonlinear behavior with activation energies of 0.52 eV at temperatures lower than 120°C and 0.33 eV at temperatures lager than 120°C. The AN structure refinement shows the change in the atomic displacement parameter (B- 3.4 to 3.7 $Å^2$) for Ag ions in the range of 80 - 120°C and this atomic displacement facilitates the movability of the silver ions and thus it may increase the total conductivity,

reducing the activation energy. The Rietveld refinement of AN indicated that the oxygen atom was statistically distributed in the 8c site, and Nb and Ag atoms randomly distributed in the 4a site. The bond valence sum (BVS) of Ag/Nb was 3.00 and this value was close to calculated 3.36 from the ratio of Ag/Nb. The B value of oxygen atom was high and this proposed that oxygen atom contributes to total conductivity.

In the case of AT silver ions were distributed in the tunnel in 16d site of the pyrochlore-type compounds and its B value was large. The oxygen atom

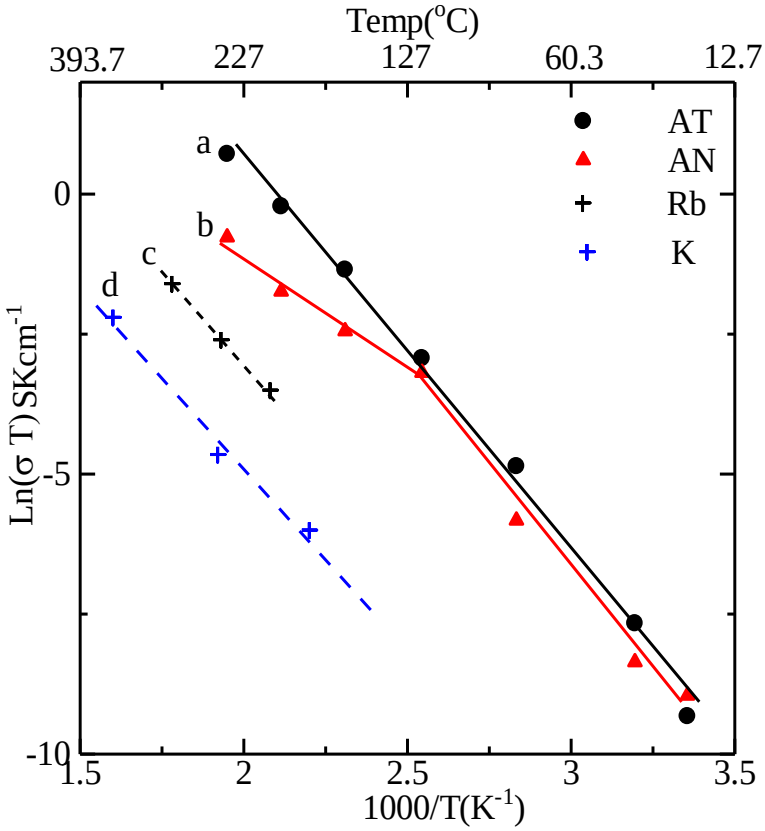

Figure 4.7: Arrhenius plot of (a) AT (b) AN (c) Rb^+ in pyrochlore structure and (d) K^+ in pyrochlore structure.

in the 8b site was in the tunnel of pyrochlore and this oxygen was thought to belong to water molecule because weight loss was detected in the TG curve and the B value of oxygen (8b) was very large. The BVS of Ta was 5.26 and Ag was 1.04 respectively which were close to 1 and 5, the real values respectively. Moreover, the corner shared TaO_6 octahedral form a rigid structure of AT tunnel compounds, after the complete removal of water molecules from the crystal structure, it provides possible migration pathways for Ag-ions moving which was previously reported by Grins *et al*[16], the K ion migration in pyrochlore type $K_{1+x}Ta_{1+x}W_{1-x}O_6 \cdot nH_2O$ compound. The activation energy of AT obtained was 0.61 eV which is almost similar with 0.65 eV to the data reported in Grins *et al.* (Fig.6). To compare with previously reported data we believe that the total conductivity of AT and AN is mainly correlated with migration of Ag^+ ions as well as protons or oxygen ions of the water molecules in the pyrochlore compounds.

4.4 Conclusions

Cubic pyrochlore-type $(K_{0.73}H_{0.27})NbO_3.0.83H_2O$ and $(K_{0.56}H_{0.44})TaO_3 \cdot 1.14H_2O$ has prepared successfully by environmental friendly hydrothermal method. Reaction of $(K_{0.73}H_{0.27})NbO_3.0.83H_2O$ with excess $AgNO_3$ produced fluorite-type structure. This fluorite type structure

was changed to perovskite at about 550 ^{o}C. $(K_{0.56}H_{0.44})TaO_3 \cdot 1.14H_2O$ was successfully ion exchanged and yield pyrochlore-type $Ag_{0.93}TaO_{2.97} \cdot 0.94H_2O$ and band gap changed from 4.6 to 1.8 eV by Ag^+ substitution.

The impedance measurement of bulk ionic conductivity at 240 °C reached the order of 10^{-3} S/cm and 10^{-4} S/cm for tantalate and niobate, respectively. The calculated activation energy of AT was 0.61 eV. The AN showed non-linear behavior with activation energies of 0.52 eV at temperatures lower than 120 °C and 0.33 eV at temperatures lager than 120 °C. The AN structure refinement reveal the change in the atomic displacement parameter B- 3.4 to 3.7 $Å^2$ for silver, in the range of 80–120 °C; this atomic displacement facilitates the mobility of silver ions and, consequently, it may increase the ionic conductivity, reducing the activation energy.

4.5 References

(1) Smirnova, O.; Kumada, N.; Yonesaki, Y.; Kinomura, N. A New Solid Electrolyte to Fill the Gap between Low Temperatures and High Temperatures SOFC Materials?. *Electroche. Commun.*, **2008**, *10* (3), 485–487.

(2) Krukowska, A.; Jerzy, M.; Strychalska-nowak, J.; Klimczuk, T.; Lisowski, W.; Mikolajczyk, A.; Pinto, H. P.; Puzyn, T.; Grzyb, T.; Zaleska-medynska, A. Environmental Rare Earth Ions Doped $K_2Ta_2O_6$ Photocatalysts with Enhanced UV – Vis Light Activity. *Appl. Catal. B.,* **2018**, *224*, 451–468.

(3) Dong, Q.; Jiang, H.; Kumada, N.; Yonesaki, Y.; Takei, T.; Kinomura, N. Preparation of a New Pyrochlore-Type Compound $Na_{0.32}Bi_{1.68}Ti_2O_{6.46}(OH)_{0.44}$ by Hydrothermal Reaction. *J. Solid State Chem.*, **2011**, *184* (7), 1899–1902.

(4) Shlyakhtina, A. V; Belov, D. A.; Pigalskiy, K. S.; Shchegolikhin, A. N.; Kolbanev, I. V; Karyagina, O. K. Synthesis , Properties and Phase Transitions of Pyrochlore- and Fluorite-like Ln_2RMO_7 (Ln = Sm, Ho ; R = Lu, Sc ; M = Nb, Ta). *Mater. Res. Bull.*, **2014**, *49*, 625–632.

(5) Lin, H. Y.; Lee, T. H.; Sie, C. Y. Photocatalytic Hydrogen Production with Nickel Oxide Intercalated $K_4Nb_6O_{17}$ under Visible Light Irradiation. *Int. J. Hydrog. Energy.*, **2008**, *33* (15), 4055–4063.

(6) Zhang, G.; He, F.; Zou, X.; Gong, J.; Zhang, H. Hydrothermal Preparation and Photocatalytic Properties of Sheet-like Nanometer Niobate $K_4Nb_6O_{17}$. *J. Phys Chem. Solids.*, **2008**, *69* (5–6), 1471–1474.

(7) Ahmed, S.; Rasul, M. G.; Martens, W. N.; Brown, R.; Hashib, M. A. Heterogeneous Photocatalytic Degradation of Phenols in Wastewater: A Review on Current Status and Developments. *Desalination.*, **2010**, *261* (1–2), 3–18.

(8) Wu, J.; Zhou, C.; Zhao, Y.; Shang, L.; Bian, T.; Shao, L.; Shi, F.; Wu, L. Z.; Tung, C. H.; Zhang, T. One-Pot Hydrothermal Synthesis and Photocatalytic Hydrogen Evolution of Pyrochlore Type $K_2Nb_2O_6$. *Chin. J. Chem.*, **2014**, *32* (6), 485–490.

(9) N. Kumada.; N. Ozawa.; N. Kinomura.; F. Muto, Preparation of pyrochlores. $A_{1-x}H_xTaO_3 \cdot nH_2O$ (A=Na, K)**.** *Mat Res Bull.*, **1985**, *20*, 583–589.

(10) H. M. Rietveld, A Profile Refinement Method for Nuclear and Magnetic Structures. *J. Appl. Crystallogr.*, **1969**, 2,65-71.

(11) Momma, K.; Izumi, F. VESTA : A Three-Dimensional Visualization System for Electronic and Structural Analysis. *J. Appl. Crystallogr*., **2008**, 653–658.

(12) Norberg, S. T.; Hull, S.; Eriksson, S. G.; Ahmed, I.; Kinyanjui, F.; Biendicho, J. J. Pyrochlore to Fluorite Transition : The $Y_2(Ti_{1-X}Zr_X)_2O_7$ ($0.0 \leq X \leq 1.0$) System. *Che. Mater.,* **2012**, 24, 22, 4294-4300.

(13) Payne, J. L.; Tucker, M. G.; Radosavljevi, I. From Fl Uorite to Pyrochlore : Characterisation of Local and Average Structure of Neodymium Zirconate , $Nd_2Zr_2O_7$. *J. Solid State Chem.,* **2013**, *205*, 29–34.

(14) Makiura, R.; Yonemura, T.; Yamada, T.; Yamauchi, M.; Ikeda, R.; Kitagawa, H.; Kato, K.; Takata, M. Size-Controlled Stabilization of the Superionic Phase to Room Temperature in Polymer-Coated AgInanoparticles. *Nat. Mater.,* **2009**, *8* (6), 476–480.

(15) Tatsumisago, M.; Shinkuma, Y.; Minami, T. Stabilization of Superionic α-Agl at Room Temperature in a Glass Matrix. *Nature.,* **1991**, *354* (6350), 217–218.

(16) Grins, J.; Nygren, M. Studies on composition, structure and ionic conductivity of the pyrochlore type system $K_{1-x}Ta_{1+x}W_{1-x}O_6$. nH_2O, $0<x<1$., *Mat.Res. Bull.,* **1980**, *15*, 53–61.

CHAPTER 5

ANTIBACTERIAL PROPERTIES OF SILVER NIOBATES AND TANTALATES

5.1 Introduction

The synthesis method of pyrochlore–type silver niobate and tantalate was described in chapter 3 and 4. This chapter, brings forward research that was focused on ion-exchanged with the different silver ions molar ratios and gradually increasing to obtain completely ion exchanged samples. This modified niobate and tantalate ion-exchanged samples could be an efficient antibacterial material which can killed the wide range of harmful bacteria.

Bacteria are a type of biological cell. As shown in Figure 5.1, they constitute a large domain of prokaryotic microorganisms which is consist of capsule, cell wall, plasma membrane, cytoplasm, ribosomes and nucleoid. A wide range of microorganisms coexists in the human body and natural environments, but a rapid and uncontrolled growth of microbes can lead some serious issues, such as diseases related to human health, increasing the rate of environmental pollution, making food rotting and making waterborne diseases like typhoid fever, dysentery, cholera, and

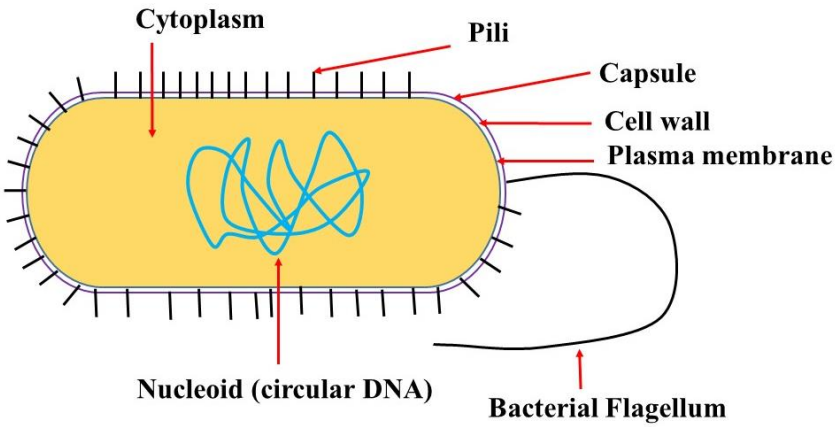

Figure 5.1: Schematic diagram of the bacterial cell

diarrhea[1]. For this reason, a new path is necessary to develop effective antimicrobial materials[2]. Thus, realization of new materials with favorable safety and strong antibacterial properties is importent[3–5]. Recently, variety of antibacterial materials, such as carbon based nanomaterials, cationic polymers, antibacterial peptides and inorganic materials have been extensively studied[6–9]. Among these studies, inorganic materials with antibacterial properties are important due to their wide range of applications including building materials, electrical appliances, medical materials, fabrics and cosmetics[10]. Furthermore these antibacterial agents have received great attention owing to their safety, good stability, wide range of antibacterial activity and longtime activity compared to organic antibacterial agents[11]. Even though several metal ions (Ag^+, Cu^+, Zn^{2+} etc.) have been used in antimicrobial ceramics, silver containing materials have gain great attention due to their strong antibacterial activity and low toxicity against mammalian cells[12–15]. The controlling of bacterial

growth in these ceramic materials can lead to a variety of other applications such as, implantable orthopedic biomaterials, bone replacements and treatment of burn wounds[17,18]. Moreover, a variety of techniques are used to synthesize Ag containing antibacterial materials, such as wet chemical methods, sol-gel method, thermal or cold spraying techniques, ion-exchange method and doping or loading method[19–21]. However, ion-exchange method has been proved to be simple way to regulate the amount of silver content to the KT and KN structures.

In this chapter, our aim was to obtain controllable antibacterial properties from these different ion-exchanged compounds and compare the killing efficiency against *E.coli* and *S. aureus* by the colony count method and inhibition zone method.

5.2 Experimental section

5.2.1 Material and characterization

Pyrochlore-type potassium niobate (KN) and potassium tantalate (KT) were synthesized by a hydrothermal reaction using niobium pentoxide (Nb_2O_5), tantalum pentoxide (Ta_2O_5) and potassium hydroxide (KOH) as starting materials according to a method described in chapter 3[22]. All chemicals were purchased from Kanto Chemical Co. Ltd (Tokyo, Japan). The silver ions were doped into the KN and KT by an ion exchange process using small molar ratios and gradually increasing to

obtain completely ion exchanged samples. In order to do achieve this, the parent compounds [KN, KT] were mixed with different molar ratios of $AgNO_3$ and the mixtures were heated at 300 °C for 6 h where the ion-exchanged molar ratio of $AgNO_3$/ KN or KT were 0.1, 0.5 and 5. The products were filtered and centrifuge with several times and dried at 60 °C for 24 h. The final products were KAN1, KAN2, KAN3, for KN ion exchanged and KAT1, KAT2, KAT3 for KT ion exchanged respectively.

The products were identified by XRD (MiniFlex 600, RigakuCo.,Tokyo,Japan) with CuKα radiation [λ= 0.15418 nm]. The particle size, chemical composition and morphology of the samples were determined by scanning electron microscopy (SEM, JEOL F65) and energy dispersive X-ray spectroscopy (EDX). The optical band gaps were estimated using UV-visible diffuse reflectance spectra (UV-Vis, JASCO V-550) and were converted by the Kubelka-Munk function. The chemical environment of the ion-exchanged silver was studied by X-ray photoelectron spectroscopy (XPS) (Axis-Ultra-DLD, Shimadzu). The amount of Ag^+ ions released from the powder samples were determined by an inductive coupled plasma atomic emission spectroscopy (ICP, Hitachi SPS3520UV-DD).

Primary, antimicrobial tests were evaluated by colony count method using *E. coil* and *S. aureus.* Furthermore, the area of the inhibition zone was studied to calculate the antibacterial efficiency and to compare the activity among the different samples. This experimental procedures thoroughly explain in chapter 2 section 2.2.2.

5.3 Results and discussion

5.3.1 Structure

In this work, three different ion exchanged molar ratios of niobate and tantalate were used to prepare the six samples with silver doped as well as complete ion

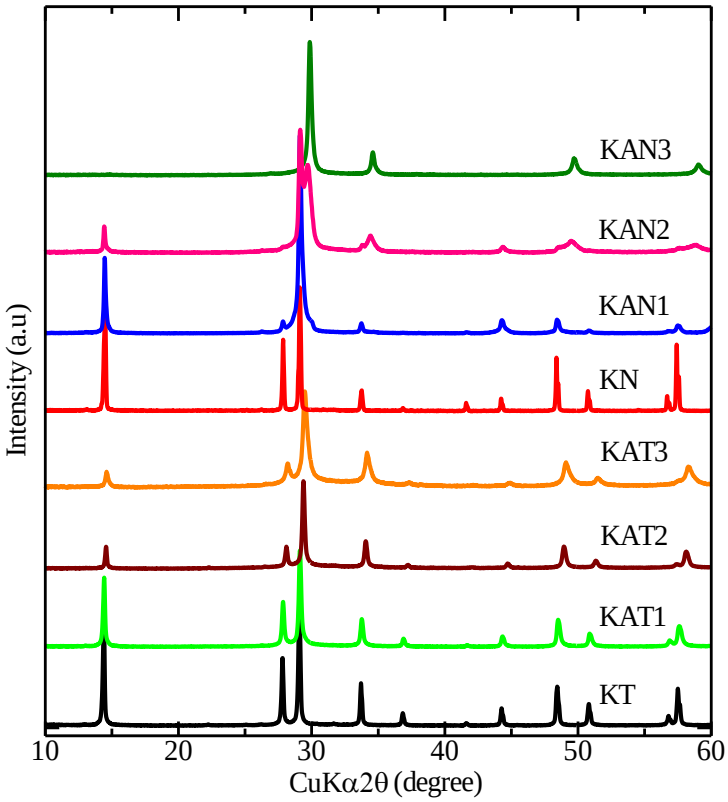

Figure 5.2: XRD pattern of parent and silver ion-exchange niobate and tantalate compounds

exchanged samples. As shown in Figure 5.2, the single-phase pyrochlore-type KT and KN were observed by hydrothermal method, (space group *Fd-3m*, #227) which is similar to the results of our previous studies explain in chapter 3[22]. The XRD pattern of silver ion doped to KN and KT structures by ion exchanged methods were indicate in KAT1, KAT2, KAN1 and KAN2 respectively. The KAT3 and KAN3 sample were observed by complete ion exchanged parent compounds using excess molten $AgNO_3$. Although, sample labelled KAN2 showed peaks associated with pyrochlore and fluorite mixed structures, KAN3 sample yielded a fluorite-type structure with space group *Fm-3m* (#225) whereas this was not observed in KAT3 sample. Previous studies have shown that, ordered pyrochlore structure ($A_2B_2O_7$) can be transformed into the disordered fluorite structure by changing the radius ratio (r_A/r_B) and relative stability range of pyrochlore structure from 1.46 to 1.78 (r_{K+} = 1.64 Å, r_{Ag+} = 1.28 Å, r_{Nb5+} = 0.64 Å r_{Ta5+} = 0.64 Å)[23,24]. Thus, KAN3 structure has been changed to fluorite type structure (r_A/r_B = 2) while unchanged structure of KAT3 was under investigation. The carefully comparison of the XRD pattern suggest that peak position shifting to some degree toward higher 2θ value (Figure 5.1) with silver ion-exchanged. These changes are due to the larger K ion replacing

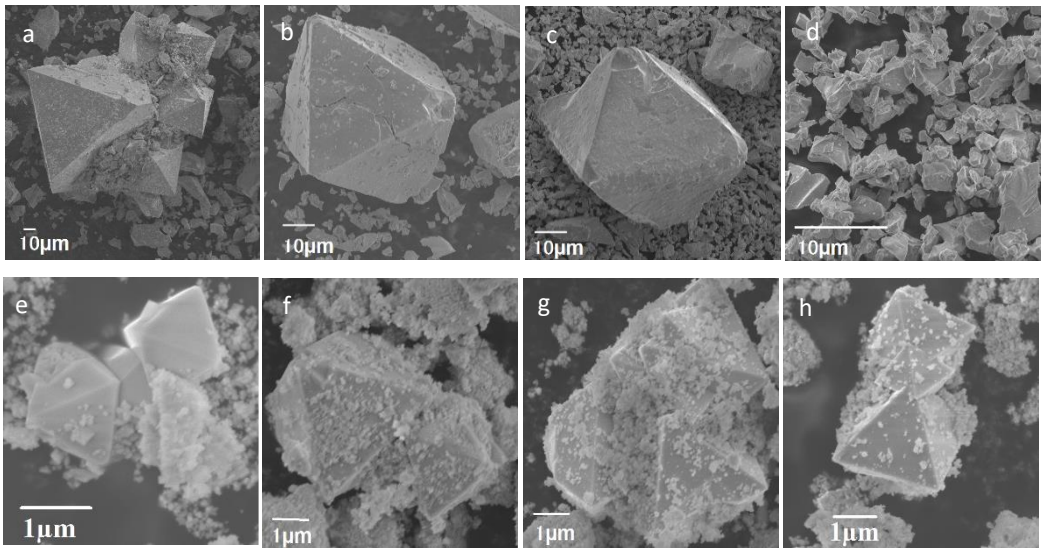

Figure 5.3: SEM image of (a)KN, (b)KAN1, (c)KAN2, (d)KAN3, (e)KT, (f) KAT1, (g)KAT2 and (h)KAT3

by small Ag ions (r_{K+} = 1.64 Å, r_{Ag+} = 1.28 Å) and which is further confirmed that the ion-exchanged reactions were successful. The SEM image [Figure 5.3 (a), (b) and (c)] showed KN and its silver ion-exchanged products with octahedral morphology and the particles size were ~50 μm. The fully ion exchanged product of KAN3 [Figure 5.3 (d)] showed irregular particle shape with practical size was approximately 1-5 μm. In the case of KT [Figure 5.3: (e), (f), (g), (h)] and octahedral morphology is preserved while ion exchange occurred and the particle sizes were approximately 1-5μm.

5.3.2 UV –Vis spectra and XPS analysis

The white pristine color of KN and KT samples color changed with the exchange of ions and turned yellowish for KN and gray for KT samples. As shown in

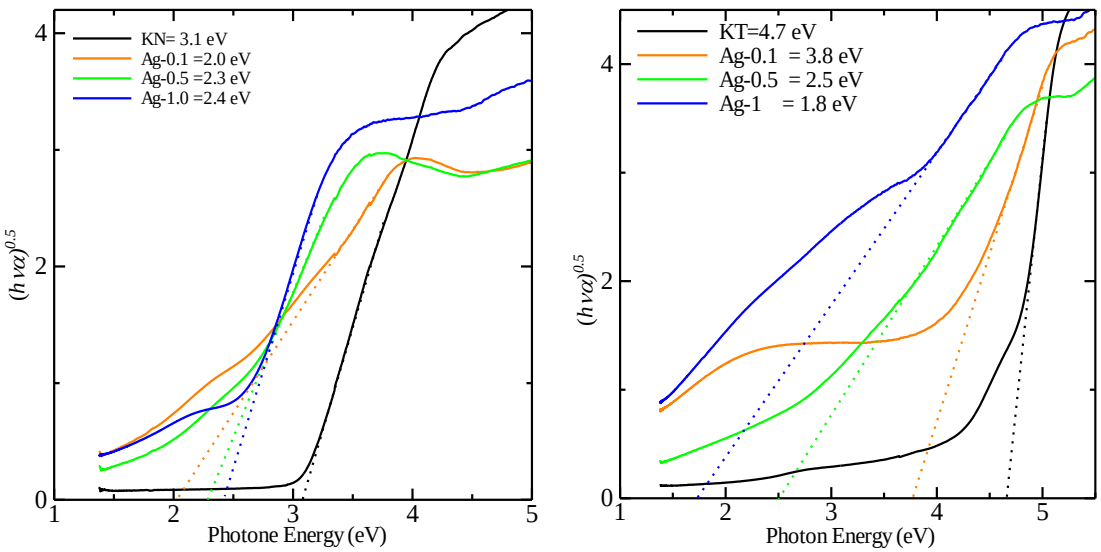

Figure 5.4: Tauc plot of (a) KN and its ion exchanged products and (b) KT and its ion exchanged products

Figure 5.4, the band gaps deceased from 3.1 eV to 2.4 eV for KN and 3.8 eV to 1.8 eV for KT respectively with the addition of the silver ions in these structures. These band gap fluctuation between the samples can be attributed to the Ag d orbital association in the hybridized energy levels[25]. Furthermore, this bandgap shifting suggests that the Ag atoms have substituted into the KN and KT compounds which is further confirmed by the X-ray photoelectron spectroscopy (XPS) data. The XPS analysis confirmed the element content of Ag, Nb, Ta, and O in the ion exchanged samples. The Ag 3d region of niobate and tantalate exhibit two binding energy peak at 367.5 - 368 and 373.6 – 374.1 eV range (Figure 5.5), which should be corresponds

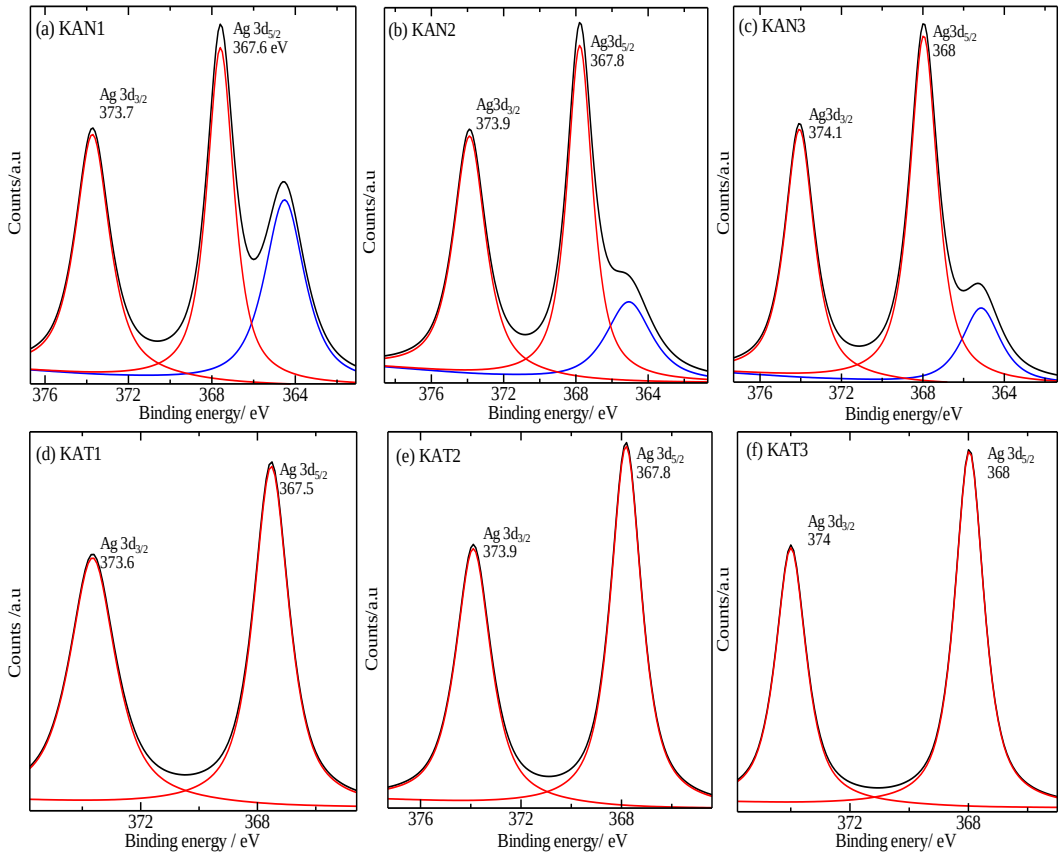

Figure 5.5: XPS spectra of the silver ion-exchanged niobate and tantalate (a-f) Ag 3d region.

to the Ag $3d_{5/2}$ and $3d_{3/2}$ respectively. Generally, the oxidation state of Ag (I) and Ag (0) peaks ($3d_{5/2}$) were always in the range of 367.5-367.8 eV and 368.0-368.4 eV respectively[26]. Therefore, lowest amount of silver ion-exchanged samples (Figure 5.5a,b,d,e) mainly exist as Ag^{+} in the crystal structure. As the ion-exchanged stoichiometric ratio of Ag vs Nb or Ta increase, Ag $3d_{5/2}$ shows a binding energy shifting with formation of metallic Ag on the surface of the structure (Figure 5.5c,f).

5.3.3 Antimicrobial properties

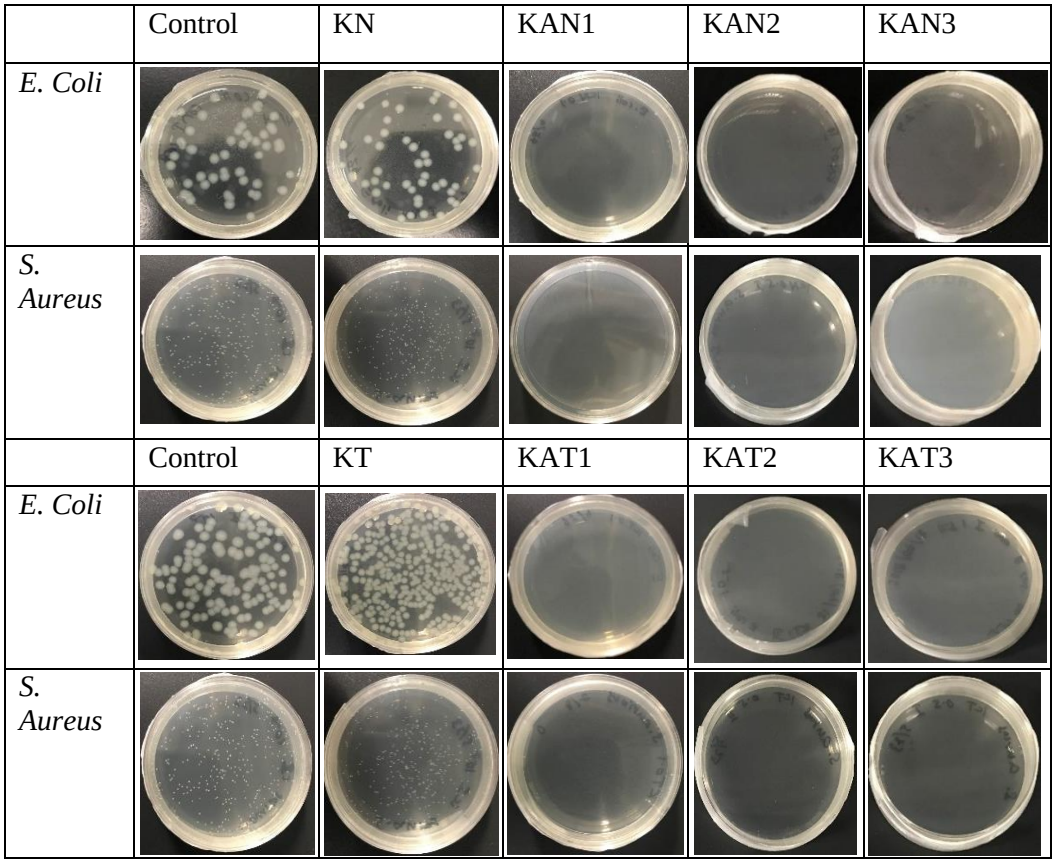

Figure 5.6: Qualitative antibacterial evaluation of control, KN, KT and silver ion-exchange samples against (a) *Escherichia coli* (b) *Staphylococcus aureus* after 24 h incubation

The antibacterial activity of Ag ion-exchanged and parent sample was evaluated by colony count method and further compared by area of inhibition zone in disk diffusion tests. The activities evaluated by colony counting method are shown Figure 5.6, and summarized in Table 1. In this study, almost 100% antibacterial activity observed by silver ions-exchanged KAN1, KAN2, KAN3, KAT1, KAT2 and KAT3 compounds compare with parent KN and KT compounds. The parent compounds shows relatively low antibacterial activity for gram positive *S. aureus* which was 5.6

% and 22 % respectively (Table 1). Although gram negative *E. coli* doesn't show any antibacterial activity for both KN and KT. This may be due to the differences in bacterial cell walls of the gram-negative and gram-positive bacteria. The gram negative bacteria like *E. coli* cell wall is slightly thinner cell wall compare with gram-positive *S. aureus*. The previous study proposed several antibacterial mechanism such as metal ions antibacterial, nanoparticle antibacterial and photocatalytic antibacterial[27]. In this experiment, antibacterial test was carried out in dark conditions, thus there is no correlation between photocatalytic ROS production by the sample and antibacterial activities. Therefore continuous release of silver ions and silver nanoparticle could show bactericidal activity and also Ag^+ ions are well

Table 5.1: Colony forming units of antibacterial test on niobate and tantalate

Sample	*E.coli*		*S. aureus*	
	No. of colonies	R (%)	No. of colonies	R (%)
Control	4.48×10^{11}		2.83×10^{12}	
KN	6.05×10^{11}	NA	2.67×10^{12}	5.6
KAN1	0	100	0	100
KAN2	0	100	0	100
KAN3	0	100	0	100
Control	2.03×10^{11}		1.99×10^{12}	
KT	2.39×10^{12}	NA	1.54×10^{12}	22
KAT1	0	100	0	100
KAT2	0	100	0	100
KAT3	0	100	0	100
*NA – No Activity				

	KN	KAN1	KAN2	KAN3
E. coli	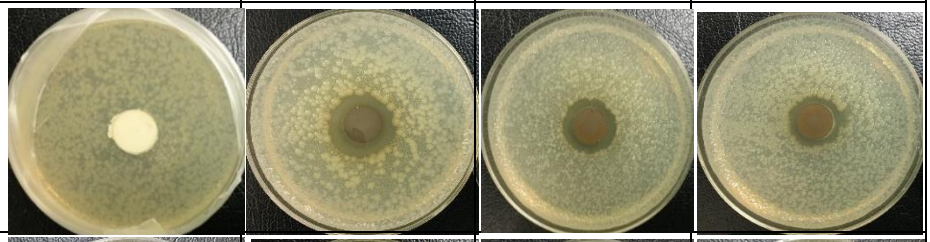			
S. aureus	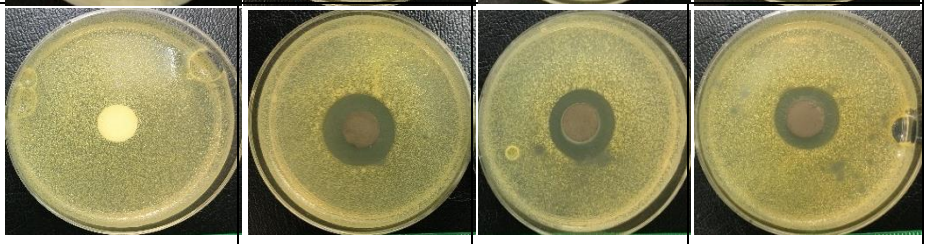			
	KT	KAT1	KAT2	KAT3
E. coli	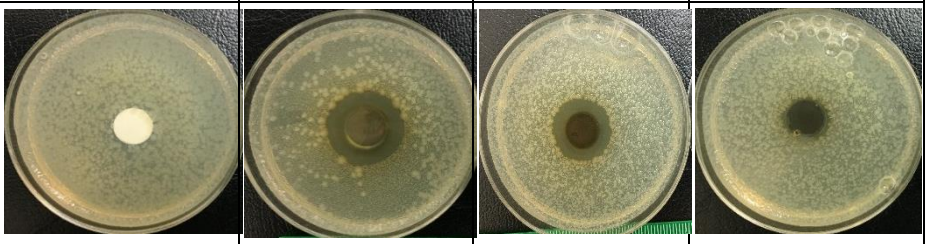			
S. aureus	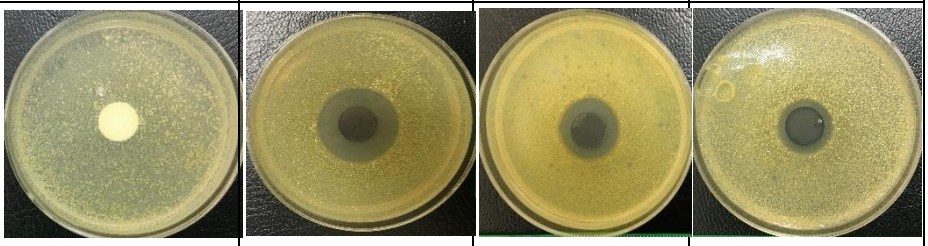			

Figure 5.7: Comparison of the inhibition zone between KN, KT silver ion-exchange samples against (a) *Escherichia coli* (b) *Staphylococcus aureus* after 48 h incubation.

known antibacterial material against a wide range of microorganism[28–30]. The Ag^{+} ion released can attach to the negatively charged bacteria cell wall by coulombic interactions and this will cause an imbalance on the surface charge around the cell. This electrostatic force and unstable surface charge leads to a disruption of the cell

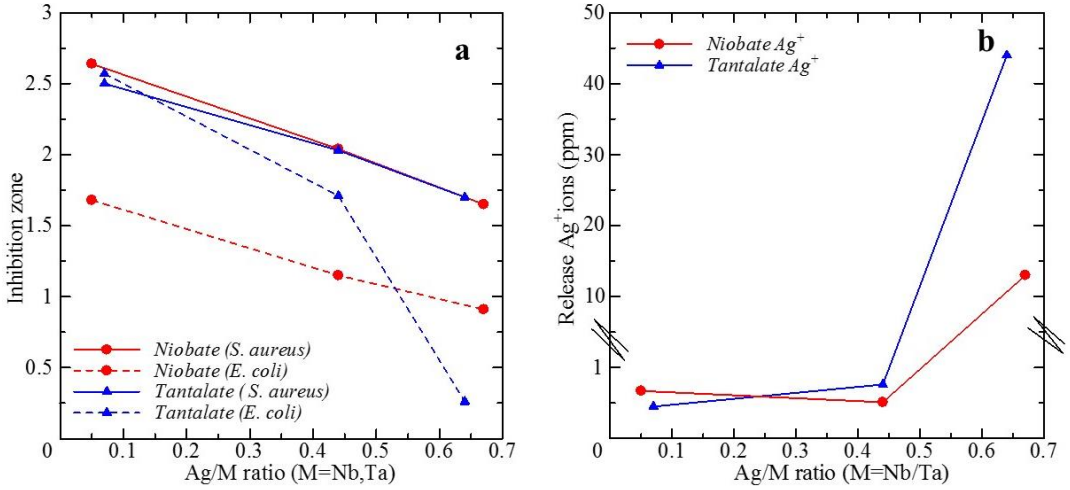

Figure 5.8: (a) The relative inhibition zone of each samples against *Escherichia coli* and *Staphylococcus aureus* after 48 h incubation (b) Release Ag^+ and K^+ ion from niobate and tantalate samples pellet after 48 hours

wall and plasma membrane, causing cell lysis and death[31]. Moreover, metal ions uptake into cell by channels of the bacterial cell membrane can cause intracellular depletion and disruption of DNA replication. Other than metal ions, silver nanoparticles with higher surface area also lead to bacteria death by easily pits and coat the bacterial surface preventing normal metabolism with external[32–34]. Therefore, almost 100% of the bacterial cells are killed by Antibacterial capability of the samples further compared by inhibition zone method (Figure 5.7). The Figure 5.8a illustrates the inhibition zones and comparisum of them aginst silver mole ratio of the samples. The all silver ion-exchange samples shows the inhibition zones against *E. coli* and *S. aureus* respectively and the parent KN and KT samples does

not show any antibacterial activities. The Ag^+ ions released to the liquid medium from each sample were shown in Figure 5.8b. The Figure 5.8a, clearly depicts the inhibition zones around the silver ion-exchanged samples were dependent on the Ag^+ discharged concentration, which mean the sizes of the inhibition zone decrease with the increase of Ag content. The tantalum phase with pyrochlore structure discharged highest amount of Ag^+ ions which is about 44.74 ppm (KAT3) and niobate phase with fluorite structure (KAN3) discharged silver content is about 13.57 ppm. These discharged silver ions are located in the tunnel (16d site) of the pyrochlore-type structure and 4a site in the fluorite-type structure[35]. As shown in Figure 5.9, tunnel structure in pyrochlore provides possible silver ion migration pathways from the

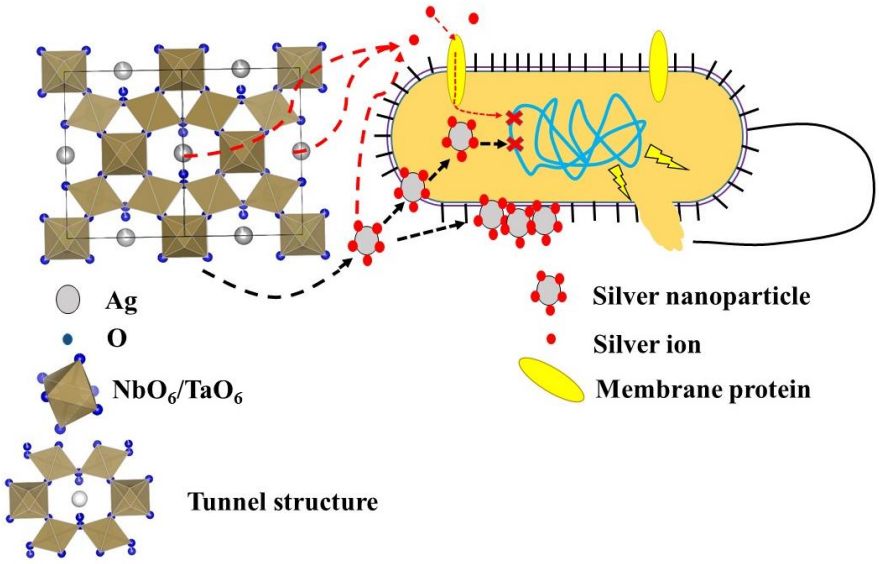

Figure 5.9: Schematic representation of antibacterial mechanism by pyrochlore type structure

powdered sample to the liquid solution. However, in the fluorite-type structure also Ag, Nb both cation are dominated in the 4a site. Even though these KAT3 and KAN3 sample discharge highest amount of silver ions, their relative antibacterial activities was lower than the other ion exchanged samples. This result particulate the silver nanoparticle (AgNP) agglomeration phenomena. The AgNPs discharged to the solution tend to minimize the surface energy by aggregation and which lead to decline in the antibacterial properties of the samples. Moreover reduction and aggregation of Ag^{+} into metal clusters also lead to the formation of AgNPs[36].

In order to investigate the AgNPs and Ag^{+} behavior during the antibacterial experiment, Surface Plasmon Resonance (SPR) measurement were implement by Uv-vis spectra. Here we can observed (Figure 5.10), AgNPs formation of KAT3 and KAN3 samples induced extra light absorbance peak around 400 nm to 425 nm and SPR band intensity decrease with other samples (KAT2, KAN2, KAT1,KAN1) respectively. Thus KAT1 and KAN1 samples show the lowest amount of silver ion discharged to the medium, they managed to minimized the AgNP agglomeration and which increasing antibacterial activities. This tunable property of niobate and tantalate compounds enables the optimization of Ag^{+} discharged for various applications, including clinical uses such as in drug delivery applications,

antibacterial resistant bacteria as well as other biomedical industries. The *S. aureus* shows the highest antibacterial capability compared to *E. coli* and this is due to the differences in bacterial cell walls of the gram-negative and gram-positive bacteria. However, Honda *et al.*[17] reported the antibacterial capability of silver containing hydroxyapatites against *S. aureus* which shows the highest inhibition zone of about 1.6. Compared to these results we see that KAN1 and KAT1 with the best antibacterial ability to have inhibition zone values of ~ 2.6 and 2.5 respectively.

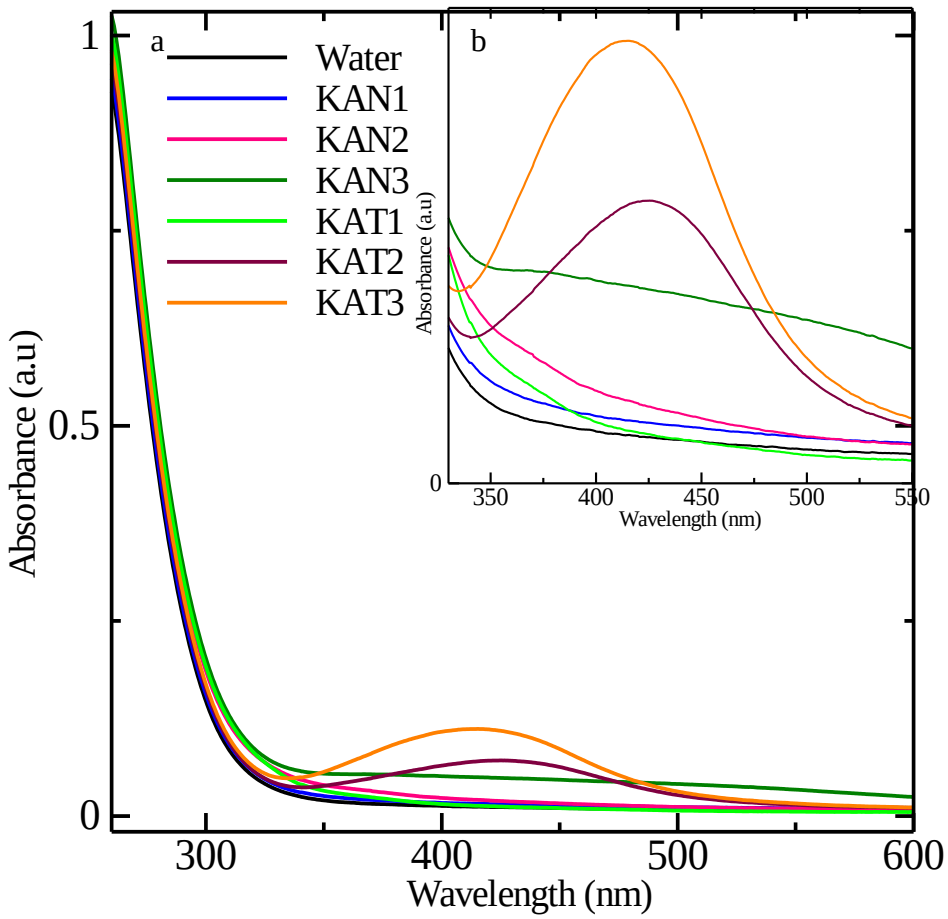

Figure 5.10: (a) UV-Vis absorbance spectra of Ag^{+} released solution after 48 hours and (b) magnified graph.

5.4 Conclusions

In this study, we have successfully developed a new powerful antibacterial materials by using pyrochlore-type $K_{0.65}H_{0.35}NbO_3 \cdot 0.29H_2O$ (KN) and $K_{0.62}H_{0.38}TaO_3 \cdot 0.53H_2O$ (KT) compounds. The silver ion-exchanged samples exhibited superior antibacterial properties to their corresponding parent compounds. The antibacterial results indicate that discharged amount of Ag^+ ions and minimizing of AgNPs aggregations are the crucial factor in the antibacterial activity. The KAN3 and KAT3 samples showed lowest relative antibacterial activity due to their discharged AgNPs agglomeration while KAN1 and KAT1 showed relatively good antibacterial activity. This controllable bactericidal effect showed due to their distinct structure where pyrochlore type structures have been consider as hosts for Ag^+ and capable in regulating their release through their tunneled structure. This study showed that silver ion exchanged samples, play a major role in enhancing antibacterial activity towards *E.coli* and *S.aureus.* Moreover, this is a new pathway to design pyrochlore-type niobates and tantalates to efficient antibacterial materials. Therefore this pyrochlore-type compounds might be a potential and powerful candidates for combating bacteria-induced infection and other various bioengineering applications.

5.5 References

(1) Dastjerdi, R.; Montazer, M. A Review on the Application of Inorganic Nano-Structured Materials in the Modification of Textiles: Focus on Anti-Microbial Properties. *Collods. Surf. B.*, **2010**, *79* (1), 5–18.

(2) Lin, H.; Lin, H. Visible-Light Photocatalytic Inactivation of Escherichia Coli by $K_4Nb_6O_{17}$ and Ag/Cu Modified $K_4Nb_6O_{17}$., *J. Hazard. Mater.*, **2012**, *217–218*, 231–237.

(3) Padhi, D. K.; Panigrahi, T. K.; Parida, K.; Singh, S. K.; Mishra, P. M. Green Synthesis of Fe_3O_4 /RGO Nanocomposite with Enhanced Photocatalytic Performance for Cr(VI) Reduction, Phenol Degradation, and Antibacterial Activity., *ACS Sustain. Chem. Eng*., **2017**, 5, 11, 10551–10562.

(4) Withanage, W. I. U.; Sayaka Y.; Takahiro T.; Nobuhiro K.; Hydrothermal Doping of Ag into Three Types of Potassium Niobates. *J.Ceram. Soc. Jpn.*, **2018**, 126 (10), 784–788.

(5) Yamamoto, Y.; Withanage, W.I.U.; Takei, T.; Sayaka Y.; Nobuhiro K.; Hisanori Y.; Hydrothermal Reaction of $NaBiO_3 \cdot nH_2O$ with Transition-Metal (Co, Ni, Cu) Salts. *J.Ceram. Soc. Jpn.*, **2018**, 126, (12), 1005-10012.

(6) Shao, W.; Liu, X.; Min, H.; Dong, G.; Feng, Q.; Zuo, S. Preparation, Characterization, and Antibacterial Activity of Silver Nanoparticle-Decorated Graphene Oxide Nanocomposite., *ACS. Appl. Mater. Interfaces.*, **2015**, 7, 12, 6966-6973.

(7) Xu, Z.; Li, M.; Li, X.; Liu, X.; Ma, F.; Wu, S.; Yeung, K. W. K.; Han, Y.; Chu, P. K. Antibacterial Activity of Silver Doped Titanate Nanowires on Ti Implants. *ACS. Appl. Mater. Interfaces.*, **2016**, 8, 26, 16584-16594.

(8) Huang, F.; Gao, Y.; Zhang, Y.; Cheng, T.; Ou, H.; Yang, L.; Liu, J.; Shi, L.; Liu, J. Silver-Decorated Polymeric Micelles Combined with Curcumin for Enhanced Antibacterial Activity. *ACS Appl. Mater. Interfaces.*, **2017**,9, 20, 16880-16889.

(9) Liu, L.; Xu, K.; Wang, H.; K, J. T. P.; Fan, W.; Venkatraman, S. S. Self-Assembled Cationic Peptide Nanoparticles as an Efficient Antimicrobial Agent. *Nat. Nanotechnol.*, **2009**, 4 , 457–463.

(10) Ewald, A.; Hösel, D.; Patel, S.; Grover, L. M.; Barralet, J. E.; Gbureck, U. Silver-Doped Calcium Phosphate Cements with Antimicrobial Activity. *Acta Biomater.*, **2011**, *7* (11), 4064–4070.

(11) Hou, Y.; Yuan, H.; Chen, H.; Ding, Y.; Li, L. Enhanced Antibacterial Activities of La/Zn-Doped $BiNbO_4$ Nanocomposites. *Chem. Res. Chin. Univ.*, **2017**, *33* (6), 917–923.

(12) Medici, S.; Peana, M.; Crisponi, G.; Nurchi, V. M.; Lachowicz, J. I.; Remelli, M.; Antonietta, M. Silver Coordination Compounds : A New Horizon in Medicine. *Coord. Chem. Rev.*, **1940**, *327–328*, 349–359.

(13) Klasen, H. J. A Historical Review of the Use of Silver in the Treatment of Burns . II . Renewed Interest for Silver., *Burns*., **2000**, *26*, 2, 131-138.

(14) Raj, H.; Pant, B.; Kumar, R.; Amarjargal, A.; Joo, H.; Hee, C.; Tijing, L. D.; Sang, C. Antibacterial and Photocatalytic Properties of $Ag/TiO_2/ZnO$ Nano-Flowers Prepared by Facile One-Pot Hydrothermal Process. *Ceram. Int.*, **2013**, *39* (2), 1503–1510.

(15) Abeyrathna, S. S.; Abeyrathna, N. S.; Thai, N. K.; Sarkar, P.; Arcy, S. D.; Meloni, G. IroT/MavN Is a Legionella Transmembrane Fe(II) Transporter: Metal Selectivity and Translocation Kinetics Revealed by in Vitro Real-Time Transport., *Biochemistry.*, **2019**, 58,43, 4337-4342.

(16) Kim, J. S.; Kuk, E.; Yu, N.; Kim, J.; Park, S. J.; Lee, J.; Kim, H.; Park, Y. K.; Park, H.; Hwang, C.; et al. Antimicrobial Effects of Silver Nanoparticles., *Nanomedicine.*, **2007**, *3*, 95–101.

(17) Honda, M.; Kawanobe, Y.; Ishii, K.; Konishi, T.; Mizumoto, M.; Kanzawa, N.; Matsumoto, M.; Aizawa, M. In Vitro and in Vivo Antimicrobial Properties of Silver-Containing Hydroxyapatite Prepared via Ultrasonic Spray Pyrolysis Route. *Mater. Sci. Eng. C.*, **2013**, *33* (8), 5008–5018.

(18) Catauro, M.; Raucci, M. G.; Gaetano, F. D. E.; Marotta, A. Antibacterial and Bioactive Silver-Containing $Na_2O \cdot CaO_2 \cdot SiO_2$ Glass Prepared by Sol-Gel Method., *J. Mater. Sci-Mater. M.*, **2004**, *5*, 831–837.

(19) Basu, B.; Gupta, R. In Vitro Biocompatibility and Antimicrobial Activity of Wet Chemically Prepared. *Mater. Sci. Eng. C* **2011**, *31* (7), 1320–1329.

(20) Noda, I.; Miyaji, F.; Ando, Y.; Miyamoto, H.; Shimazaki, T.; Yonekura, Y.; Miyazaki, M.; Mawatari, M.; Hotokebuchi, T. Development of Novel Thermal Sprayed Antibacterial Coating and Evaluation of Release Properties of Silver Ions., *J. Biomed. Mater. Res. B. Appl. Biomater.,* **2008**, 456–465.

(21) Lee, I.; Whang, C.; Oh, K.; Park, J. Formation of Silver Incorporated Calcium Phosphate Film. *Nucl. Instrum. Methods Phys. Res. B.*, **2006**, *242*, 45–47.

(22) Withanage, I.; Kumada, N.; Takei, T.; Yanagida, S.; Kuroiwa, Y.; Moriyoshi, C. Synthesis and Crystal Structure of Pyrochlore-Type Silver Niobate and Tantalate.,*J. Ceram. Soc. Jpn.*, **2017**, *125* (10), 776–778.

(23) Thampi, D. S. V.; Rao, P. P.; Renju, U. A. Studies on Order – Disorder Transition , Lattice Expansion and Ionic Conductivity in Aliovalent Cation Substituted $Sm_2Zr_2O_7$ System. *J. Solid State Chem.*, **2017**, *255*, 121–128.

(24) Payne, J. L.; Tucker, M. G.; Radosavljevi, I. Journal of Solid State Chemistry From Fl Uorite to Pyrochlore : Characterisation of Local and Average Structure of Neodymium Zirconate , $Nd_2Zr_2O_7$. *J. Solid State Chem.*, **2013**, *205*, 29–34.

(25) Dutta, D. P.; Ramakrishnan, M.; Roy, M.; Kumar, A. Journal of Photochemistry and Photobiology A : Chemistry Effect of Transition Metal Doping on the Photocatalytic Properties of $FeVO_4$ Nanoparticles. *J. Photochem. Photobiol. A.,* **2017**, *335*, 102–111.

(26) Fu, F.; Gu, J.; Cao, J.; Shen, R.; Liu, H.; Zhang, Y.; Liu, X.; Zhou, J. Reduction of Silver Ions Using an Alkaline Cellulose Dope: Straightforward Access to Ag/ZnO Decorated Cellulose Nanocomposite Film with Enhanced Antibacterial Activities. *ACS Sustainable Chem. Eng.*, **2018**, 6, 1, 738-748.

(27) Wyszogrodzka, G.; Marszałek, B.; Gil, B.; Dorozyński, P. Metal-Organic Frameworks: Mechanisms of Antibacterial Action and Potential Applications. *Drug Discov. Today.*, **2016**, *21* (6), 1009–1018.

(28) Jung, W. K.; Koo, H. C.; Kim, K. W.; Shin, S.; Kim, S. H.; Park, Y. H. Antibacterial Activity and Mechanism of Action of the Silver Ion in Staphylococcus Aureus and Escherichia Coli. *Appl. Environ. Microbiol.*, **2008**, 74 (7), 2171–2178.

(29) Kakinuma, H.; Ishii, K.; Ishihama, H.; Honda, M.; Toyama, Y.; Matsumoto, M.; Aizawa, M. Antibacterial Polyetheretherketone Implants Immobilized with Silver Ions Based on Chelate-Bonding Ability of Inositol Phosphate : Processing , Material Characterization , Cytotoxicity , and Antibacterial Properties. *J. biomat. Res.* **2014**, 1–8.

(30) Dutta, D. P.; Singh, A.; Tyagi, A. K. Journal of Environmental Chemical Engineering Ag Doped and Ag Dispersed Nano $ZnTiO_3$:Improved Photocatalytic Organic Pollutant Degradation under Solar Irradiation and Antibacterial Activity. *Biochem. Pharmacol.*, **2014**, 2 (4), 2177–2187.

(31) Ruparelia, J. P.; Kumar, A.; Duttagupta, S. P. Strain Specificity in Antimicrobial Activity of Silver and Copper Nanoparticles. *Acta Biomater.*, **2008**, *4*, 707–716.

(32) Liu, Y.; Wang, X.; Yang, F.; Yang, X. Excellent Antimicrobial Properties of Mesoporous Anatase $TiO_2$and Ag/TiO_2composite Films. *Micropor. Mesopor. Mat.*, **2008**, 114 (1–3), 431–439.

(33) Sirelkhatim, A.; Mahmud, S.; Seeni, A.; Kaus, N. H. M.; Ann, L. C.; Bakhori, S. K. M.; Hasan, H.; Mohamad, D. Review on Zinc Oxide Nanoparticles: Antibacterial Activity and Toxicity Mechanism. *Nanomicro Lett.*, **2015**, *7* (3), 219–242.

(34) Cho, K.; Park, J.; Osaka, T.; Park, S. The Study of Antimicrobial Activity and Preservative Effects of Nanosilver Ingredient. *Electrochim. Acta.*, **2005**, *51*, 956–960.

(35) Isuru, W.; Withanage, U.; Kumada, N.; Takei, T.; Yanagida, S.; Tadanaga, K.; Miura, A.; Rosero-navarro, N. C.; Azuma, M. Electrical Properties of Pyrochlore-Type Silver Tantalate and Fluorite-Type Silver Niobate. *J. Ceram. Soc. Jpn.*, **2020**, 128 (1), 46–50.

(36) Kapoor, S.; Lawless, D.; Kennepohl, P.; Meisel, D. Reduction and Aggregation of Silver Ions in Aqueous Gelatin Solutions Reduction and Aggregation of Silver Ions in Aqueous Gelatin Solutions. *Langmuir.*, **1994**, 10, 9, 3018-3022.

CHAPTER 6

ANTIMICROBIAL PROPERTIES OF PEROVSKITE TYPE Ag/$KNbO_3$ PREPARED BY ONE-POT HYDROTHERMAL PROCESS

6.1 Introduction

Synthesis method of silver loaded perovskite-type niobates were detailed in chapter 3 (Figure 6.1). This chapter is focused on the different silver ion loaded perovskite structure and its antibacterial activity. Even though metal cation loaded perovskite $KNbO_3$ structure is famous for photocatalytic materials, there are no report about antibacterial activity about it. In this study we are attempted to investigate the antibacterial properties of the perovskite structure.

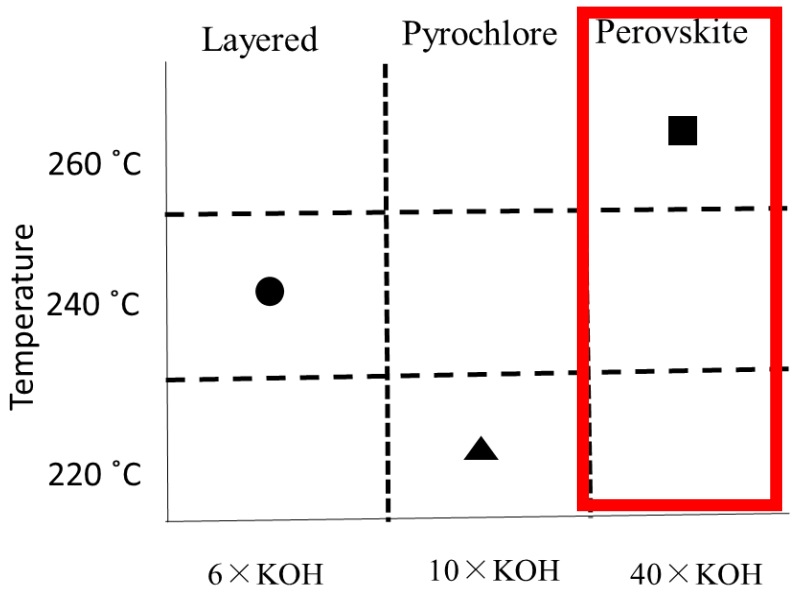

Figure 6.1: K_2O-Nb_2O_5-H_2O hydrothermal system

After discovery of Fujishima-Honda effect in 1972, semiconductor-based heterogeneous photocatalytic materials opened the wide range of application areas such as hydrogen generation, self-cleaning applications, organic pollutant degradation and antibacterial activity for waste water treatment[1–4]. These findings showed us to new path for water purification method which could be decompose organic contaminate in waste water as well as microorganism like bacteria, fungi, parasites and viruses. Other than the water purification, biocompatible ceramic materials with antibacterial activity are important for implantation, bone replacements and treatment of burn wounds [5–7]. Furthermore, there has been lots of research progresses for development of antibacterial materials for fight microbial resistant. Therefore it is important to develop and test new kinds of antibacterial agents which are environmental friendly and safe.

Among the various types of materials, perovskite-type oxides with general formula ABO_3 have attracted due to its unique structure and diverse applications[8]. Here A atom is generally larger than B atom in the well-defined structure, which physicochemical properties can be controlled by metal cation doping or loading[9–11]. Furthermore perovskite-type $KNbO_3$-based ceramics materials are very important, because they are promising candidatures for preparation of led free piezoelectric

materials, photocatalyst and optical devices [12,13]. The potassium niobate and metal cation loaded potassium niobate (M/$KNbO_3$) structure was reported as one of good photocatalyst for hydrogen generation[14,15], some other properties such as antibacterial capability has not been investigated yet. Although, Zhang *et.al*[16] and Withanage *et.al*[17] were reported organic pollutant decomposition by Ag/$KNbO_3$, to the best of our realization there have been no reports about antibacterial properties for Ag/$KNbO_3$. In this study, we attempted to load silver into potassium niobate structure by one pot hydrothermal reaction and examine their antibacterial activity by inhibition zone method using *E.coli* and *S. aureus* in the dark conditions.

6.2 Experimental section

6.2.1 Material and characterization

$KNbO_3$ and its silver loaded powder samples were prepared by hydrothermal method. The Niobium pentoxide (Nb_2O_5), potassium hydroxide (KOH), and silver nitrate ($AgNO_3$) were used as the starting materials. All chemicals were purchased from Kanto Chemical Co. Ltd (Tokyo, Japan) and used without further purification. The molar ratio of KOH/ Nb_2O_5 was 40 and the reaction temperature was 260 °C for 48h. The mole ratio of $AgNO_3/Nb_2O_5$ was changed to 0, 0.05, 0.1, 0.5 and hydrothermal reaction was carried out in a Teflon-lined autoclave. After that,

products were filtered, washed by several times with distilled water and dried at 60 °C for 24 h. The products were identified by X-ray powder diffraction (XRD) (MiniFlex 600, RigakuCo.,Tokyo,Japan) with Cu$K\alpha$ radiation ((λ= 0.15418 nm) and crystal structures were refined by the Rietveld method using synchrotron powder X-ray diffraction data (SPXRD) (beamline BL02B2). The structures were refined by RIETAN-FP program and were constructed using VESTA software. The morphology and particle size of the product were observed by Field Emission Scanning Electron Microscopy (FESEM) system (JEOL Model JSM-6500F). The released Ag ion content from the samples were determined by inductive coupled plasma atomic emission spectroscopy (ICP, Hitachi SPS3520UV-DD) and chemical compositions were determined by energy dispersive X-ray spectroscopy (EDX). The optical band gap was estimated using UV-visible diffuse reflectance spectroscopy (UV-Vis, JASCO V-550) wavelength range 200 to 800 nm and were converted by Kubelka-Munk function. The chemical environment of the surface silver was studied by X-ray photoelectron spectroscopy (XPS) (JEOL-F6500). The antimicrobial activity of silver load and parent samples were evaluated by inhibition zone method using Gram-negative *E. coil* and the Gram-positive *S. aureus* bacteria.

6.3 Results and discussion

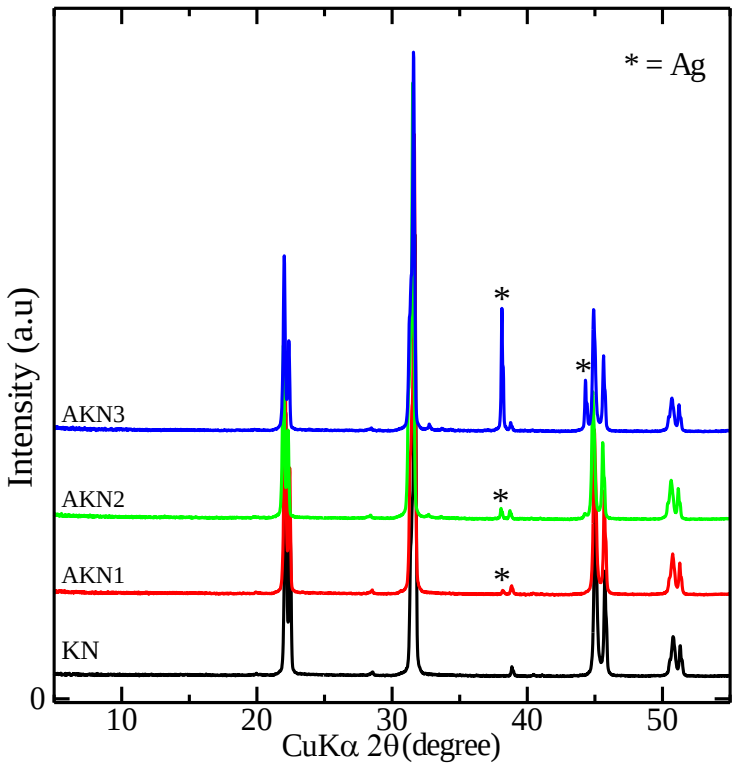

Figure 6.2: XRD pattern of parent and silver loaded samples

Hydrothermal reaction yielded single phase perovskite-type $KNbO_3$ (KN) while silver incorporated samples showed silver loaded ($Ag@KNbO_3$) structure. The final products with three different Ag/Nb mole ratio were denoted as 0.008 (AKN1), 0.01 (AKN2) and 0.06 (AKN3). The XRD pattern of the pristine KN and its silver loaded samples are shown in Figure 6.2. The face-centered cubic (fcc) silver crystal attributed 111 and 200 peaks were easily detected in XRD pattern and peak intensity increase with increasing silver content. The crystal structure of the initial KN compound was refined by Rietveld method using SPXRD data (Fig. 6.3). This

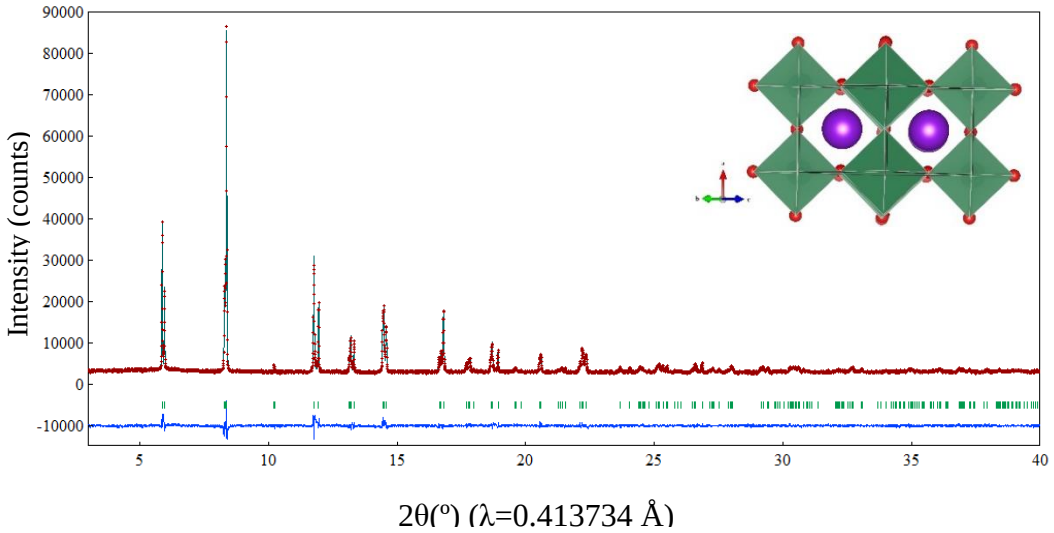

Figure 6.3: Rietveld refinement pattern and structure of the $KNbO_3$

is showed that orthorhombic crystal symmetry with space group *Amm2* and lattice parameters were a= 3.9724(8) Å, b= 5.6914(1) Å, c= 5.7162(1) Å and R- factors were R_{wp} = 5.62% and R_p = 4.13%. This orthorhombic perovskite structure was previously reported by Kumada *et.al* [18]and lattice parameters [a = 3.976(2) Å, b = 5.695(4) Å, and c = 5.717(3) Å] were well agreed with the present data. Moreover, refined unit cell parameters of silver loaded sample (AKN1) shows negligible difference with parent compound which is clearly indicate that crystal structure was maintained during the hydrothermal reaction. The most of the reported research used extra processes like silver deposition by $AgNO_3$ solution after parent compound prepared. But this one pot synthesis method is one-step method to prepare silver nanoparticle (NP) decorated KN powder samples. The image of the pristine and NP

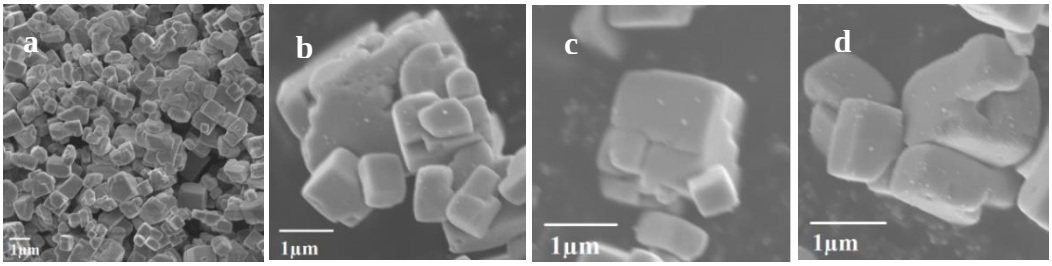

Figure 6.4: SEM image of (a)KN, (b) AKN1, (c) AKN2, (d) AKN3

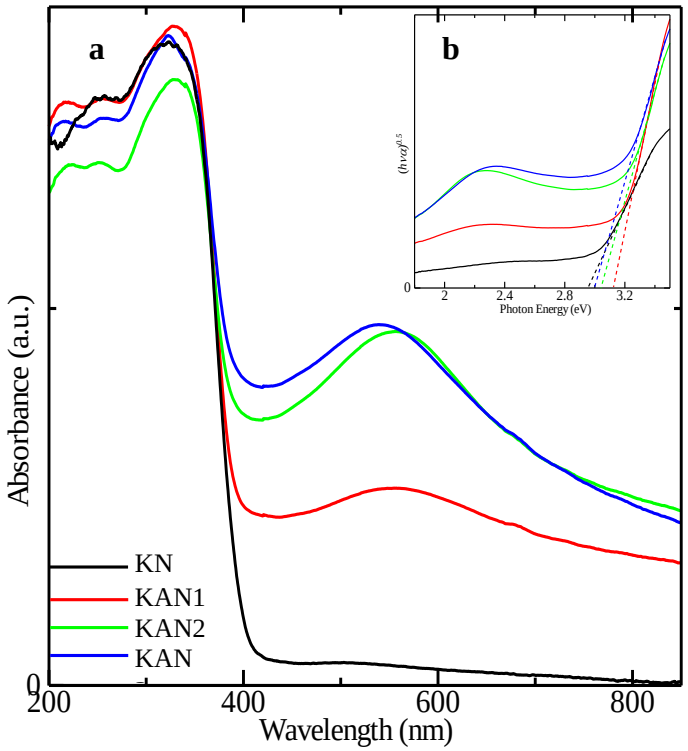

Figure 6.5: (a) Uv-Vis DR spectra of KN, KAN1, KAN2 and KAN3; the insert is band gap calculation by (b) Tauc plot

dispersed samples examine under FESEM shown in Figure 6.4. This is clearly showed that morphology and surface microstructure of the samples. The morphology of the samples were rectangular shape with practical size was approximately 1-3 µm and silver NP were decorated on the surface of samples (white dots) shown in Figure 6.3 (b),(c),(d). The optical properties of the $KNbO_3$ and $Ag@KNbO_3$ samples

were evaluated by UV-vis diffuse reflectance spectra (DRS) as shown in Figure 6.5. The KN powder sample show absorption when wavelength less than 400 nm while silver loaded samples shows Localized Surface Plasmon Resonance (LSPR) derived absorption at about 550 nm (Fig 6.5)[16,19]. Furthermore, the LSPR absorption peak notably intensified with Ag/Nb stoichiometric ratio increased. This peak exhibits in visible region, which is caused to noticeable color change of the silver loaded samples white pristine color ($KNbO_3$) to pink color ($Ag@KNbO_3$). This results suggest that the silver nanoparticles play an important role to enhance the visible light absorption. The band gap energies of the sample calculated by Kubelka-Munk function were estimated to 2.9 - 3.1 eV, as shown in Figure 6.5b. This results is moderately agree with previously reported results[20,21].

To affirm the surface chemistry and the elemental composition of the $Ag@KNbO_3$ samples were further characterized by XPS analysis and results are shown in Figure 6.6. The XPS spectra were calibrated by C1s peak at 285 eV of the surface adventitious carbon and confirmed the element content of K, Ag, Nb, O and C. The high resolution XPS spectra of the Ag 3d region of $Ag@KNbO_3$ exhibited two different silver states, contributing peak at 368 eV and 374 eV corresponds to the metallic state of the Ag $3d_{5/2}$ and Ag $3d_{3/2}$ respectively. These results indicate

that some unreacted silver ions are reduce as a metallic Ag in $KNbO_3$ surface during the hydrothermal process.

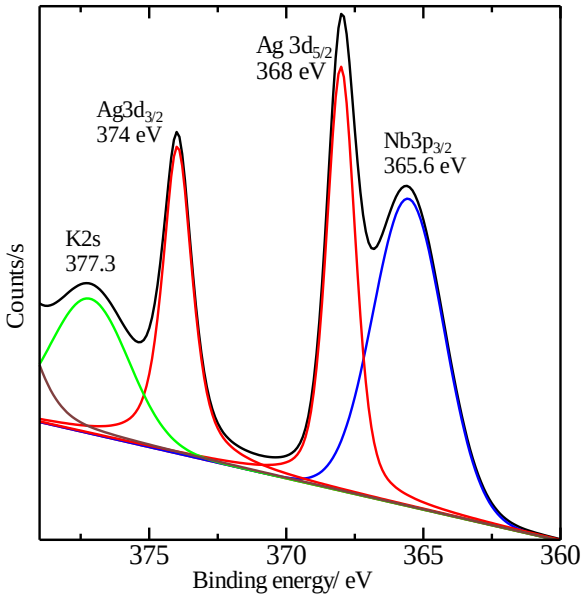

Figure 6.6: XPS spectra of the KAN3 Ag 3d region

6.3.1 Antibacterial properties

The antibacterial activity of pure KN and Ag nanoparticles loaded KN were tested against *Staphylococcus aureus* (*S. aureus*, gram-positive) and *Escherichia coli* (*E. coli*, gram-negative). The inhibition zone of the samples showed in Figure 6.7 and it could be seen that silver loaded AKN3 sample have grate antibacterial activity against both gram-positive and negative bacteria compare with KN, AKN1and AKN2. The relative inhibition zone was 0.67 for *E. coli* and 0.32 for *S. aureus*

respectively for AKN3. This results clearly show that antibacterial activity was depend on the concentration of the silver

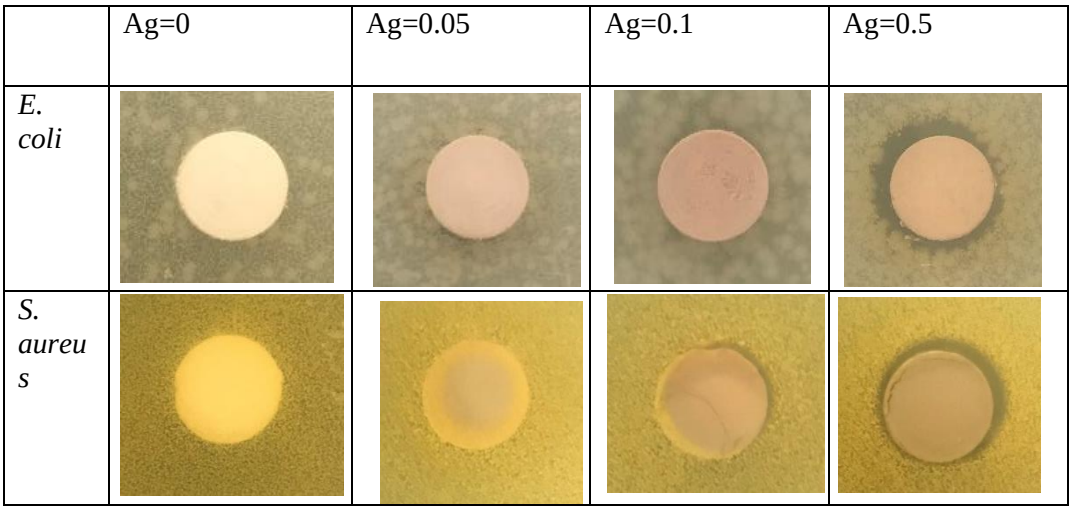

Figure 6.7: Comparison of the inhibition zone between perovskite-type Ag@$KNbO_3$ samples against (a) *Escherichia coli* (b) *Staphylococcus aureus* after 48 h incubation.

nanoparticles disperse on the crystal surface and activity was stated about Ag/Nb = 0.06 (AKN3) which is calculated by EDX. There are several types of antibacterial mechanisms explain in literature such as nanoparticle antibacterial, photocatalytic antibacterial and metal ion antibacterial[22]. In this experiment, all experimental testing were carried out in dark condition therefore no relationship between ROS generation and photocatalytic antibacterial mechanism. Therefore antibacterial mechanism mainly driven by silver nanoparticles. However, literature show that, antibacterial mechanism by silver nanoparticles has not been fully understood yet[23,24]. But some authors are accepted that, silver nanoparticle with higher surface

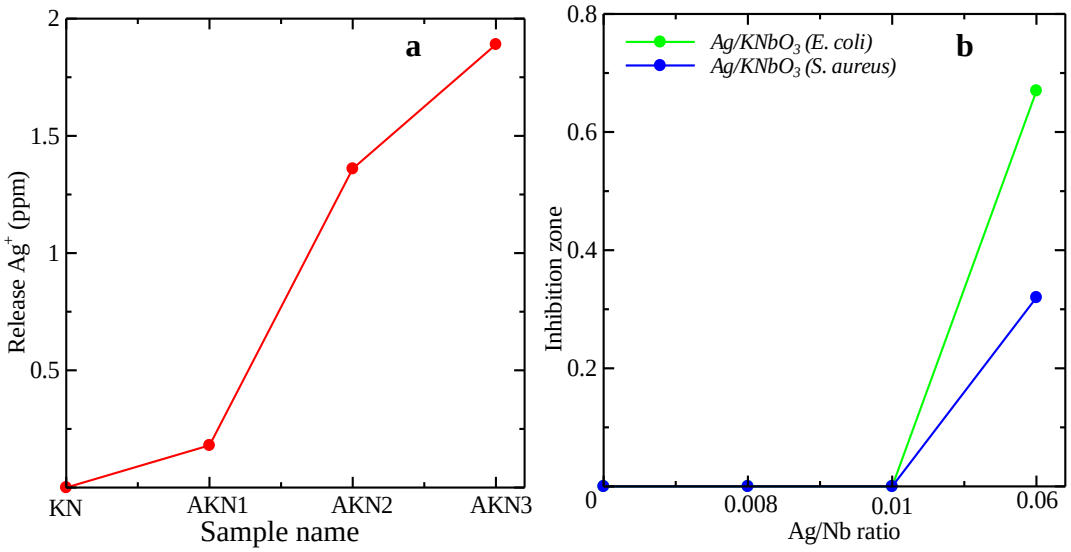

Figure 6.8: (a) Release Ag^+ ion from $Ag@KNbO_3$ samples after 48 hours and (b) relative inhibition zone of the samples against *Escherichia coli* and *Staphylococcus aureus*

area can attached and coat the surface of cell membrane which disturb the normal metabolism with external cause to cell lysis[26][26]. Further reported that, the silver nanoparticle in aqueous solution released silver ions (Ag^+) which can be attached to negatively charge bacterial cell wall membrane and damage lead to bacteria death[27]. The Figure 6.8 shows, released silver ions calculated by ICP analysis after 48h and it is clearly showed that amount of AgNP conversation to Ag^+ in the aqueous solution. The AKN3 showed highest amount of released silver after 48h which is about 1.89 ppm. The AKN1 and AKN2 released 0.18 and 1.36 ppm respectively.

6.4 Conclusions

The one pot hydrothermal synthesis has been successfully used for prepare silver nanoparticle decorated $KNbO_3$ powder samples. The obtained results show that AKN3 sample show good antibacterial properties with relative inhibition was 0.67 for *E. coli* and 0.32 for *S. aureus* respectively. The silver nanoparticles were decorated on the $KNbO_3$ surface play an important role for inhibition of bacteria which is started at Ag/Nb = 0.06 (AKN3). Silver loaded samples shows LSPR derived absorption at about 550 nm, which is caused the noticeable color change of silver loaded samples white pristine color ($KNbO_3$) to pink color ($Ag@KNbO_3$). This $Ag@KNbO_3$ sample was believed to be a good application for antibacterial ceramic material as well as photocatalytic agent for organic compound degradation for water purification industries.

6.5 Reference

(1) Hashimoto, K.; Irie, H.; Fujishima, A., TiO_2 Photocatalysis : A Historical Overview and Future Prospects., *Jpn. J. Appl. Phys.*, 44, 8269.

(2) Fujishima, A.; Honda, K.;Molecular Electrochemical Photolysis of Water at a Semiconductor Electrode One and Two-Dimensional Structure of Alpha-Helix and Beta-Sheet Forms of Poly (L-Alanine) Shown by Specific Heat Measurements at Low Temperatures (1.5-20 K). *Nature.*, **1972**, 238, 37–38.

(3) Kato, H.; Kudo, A. Highly Efficient Decomposition of Pure Water into H_2 and O_2 over $NaTaO_3$ Photocatalysts., Chem. Lett., **1999**, 28, 11, 1207–1208.

(4) Tsuji, I.; Kato, H.; Kobayashi, H.; Kudo, A. Photocatalytic H_2 Evolution Reaction from Aqueous Solutions over Band Structure-Controlled (Agln)x$Zn_{2(1-x)}S_2$ Solid Solution Photocatalysts with Visible-Light Response and Their Surface Nanostructures. *J. Am. Chem. Soc.*, **2004**, *126* (41), 13406–13413.

(5) Yao, T.; Chen, J.; Wang, Z.; Zhai, J.; Li, Y. Colloids and Surfaces B : Biointerfaces The Antibacterial E Ff Ect of Potassium-Sodium Niobate Ceramics Based on Controlling Piezoelectric Properties. *Colloids. Surf. B.*, **2019**, 175, 463–468.

(6) Kakinuma, H.; Ishii, K.; Ishihama, H.; Honda, M.; Toyama, Y.; Matsumoto, M.; Aizawa, M. Antibacterial Polyetheretherketone Implants Immobilized with Silver Ions Based on Chelate-Bonding Ability of Inositol Phosphate : Processing , Material Characterization , Cytotoxicity , and Antibacterial Properties. *J. Biomed. Mater. Res.*, **2014**, 1–8.

(7) Honda, M.; Kawanobe, Y.; Ishii, K.; Konishi, T.; Mizumoto, M.; Kanzawa, N.; Matsumoto, M.; Aizawa, M. In Vitro and in Vivo Antimicrobial Properties of Silver-Containing Hydroxyapatite Prepared via Ultrasonic Spray Pyrolysis Route. *Mater. Sci. Eng. C.*, **2013**, *33* (8), 5008–5018.

(8) Kanhere, P.; Chen, Z. A Review on Visible Light Active Perovskite-Based Photocatalysts., *Molecules.*, **2014**, 19995–20022.

(9) Wang, S.; Huang, K.; Zheng, B.; Zhang, J.; Feng, S. Mild Hydrothermal Synthesis and Physical Property of Perovskite Sr Doped $LaCrO_3$. *Mater. Lett.*, **2013**, *101*, 86–89.

(10) An, L.; Onishi, H. Electron−Hole Recombination Controlled by Metal Doping Sites in $NaTaO_3$ phoocatalyst. *ACS Catal*., **2015,** 5, 6, 3196-3206.

(11) Zhou, X.; Shi, J.; Li, C. Effect of Metal Doping on Electronic Structure and Visible Light Absorption of $SrTiO_3$ and $NaTaO_3$ (Metal = Mn, Fe, and Co). *J. Phys. Chem. C.*, **2011**, 3, 8305–8311.

(12) Jung, J. H.; Chen, C.; Yun, B. K.; Lee, N. Lead-Free $KNbO_3$ Ferroelectric Nanorod Based Flexible Nanogenerators and Capacitors.*Nanotechnology.*, 23, 37.

(13) Fujii, I.; Shimizu, S.; Yamashita, K.; Nakashima, K.; Kumada, N.; Fujii, I.; Shimizu, S.; Yamashita, K.; Nakashima, K. Enhanced Piezoelectric

Response of $BaTiO_3$–$KNbO_3$ Composites. *Appl. Phys. Lett.*, **2011**, 99, 202902..

(14) Zhang, T.; Zhao, K.; Yu, J.; Jin, J.; Qi, Y.; Li, H.; Hou, X.; Liu, G. Photocatalytic Water Splitting for Hydrogen Generation on Cubic, Orthorhombic, and Tetragonal $KNbO_3$ microcubes. *Nanoscale.*, **2013**, *5* (18), 8375–8383.

(15) Choi, J.; Ryu, Y.; Balcerski, W.; Lee, T. K.; Hoffmann, M. R. Photocatalytic Production of Hydrogen on Ni/NiO/$KNbO_3$/CdS Nanocomposites Using Visible Light. *J. Mater. Chem.*, **2008**, 2371–2378.

(16) Zhang, T.; Lei, W.; Liu, P.; Rodriguez, J. A.; Yu, J.; Qi, Y.; Liu, G.; Liu, M. Organic Pollutant Photodecomposition by Ag/$KNbO_3$ Nanocomposites: A Combined Experimental and Theoretical Study. *J. Phys. Chem. C.*, **2016**, *120* (5), 2777–2786.

(17) Withanage, W. I. U.; Sayaka Y.; Takahiro T.; Nobuhiro K.; Hydrothermal Doping of Ag into Three Types of Potassium Niobates. *J.Ceram. Soc. Jpn.*, **2018**, 126 (10), 784–788.

(18) Kumada, N.; Kyoda, T.; Yonesaki, Y.; Takei, T.; Kinomura, N. Preparation of $KNbO_3$ by Hydrothermal Reaction. *Mater. Res. Bull.*, **2007**, *42* (10), 1856–1862.

(19) Yu, Z.; Zhan, B.; Ge, B.; Zhu, Y.; Dai, Y.; Zhou, G.; Yu, F. Applied Surface Science Synthesis of High E Ffi Cient and Stable Plasmonic Photocatalyst Ag/$AgNbO_3$ with Specific Exposed Crystal-Facets and Intimate Heterogeneous Interface via Combustion Route. *Appl. Surf. Sci.*, **2019**, 488, 485–493.

(20) Shi, H.; Zou, Z. Journal of Physics and Chemistry of Solids Photophysical and Photocatalytic Properties of $ANbO_3$ (A = Na, K) Photocatalysts. *J. Phys. Chem. Solids*., **2012**, 73, 788–792.

(21) Liu, J. W.; Chen, G.; Li, Z. H.; Zhang, Z. G. Hydrothermal Synthesis and Photocatalytic Properties of $ATaO_3$ and $ANbO_3$ (A = Na and K). *Int. J. Hydrog. Energy.*, **2007**, *32*, 2269–2272.

(22) Wyszogrodzka, G.; Marszałek, B.; Gil, B.; Dorozyński, P. Metal-Organic Frameworks: Mechanisms of Antibacterial Action and Potential Applications. *Drug Discov. Today.*, **2016**, *21* (6), 1009–1018.

(23) Chen, X.; Schluesener, H. J. Nanosilver : A Nanoproduct in Medical Application. **2008**, *176*, 1–12.

(24) Roguska, A.; Belcarz, A.; Piersiak, T.; Pisarek, M. Evaluation of the Antibacterial Activity of Ag-Loaded TiO_2 Nanotubes. *Toxicol. Lett.*, **2012**, 176, 1, 1–12.

(25) Liu, Y.; Wang, X.; Yang, F.; Yang, X. Excellent Antimicrobial Properties of Mesoporous Anatase TiO2and Ag/TiO2composite Films. *Micropor. Mesopor. Mat.* **2008**, 114 (1–3), 431–439.

(26) Dutta, D. P.; Singh, A.; Tyagi, A. K. Journal of Environmental Chemical Engineering Ag Doped and Ag Dispersed Nano $ZnTiO_3$: Improved Photocatalytic Organic Pollutant Degradation under Solar Irradiation and Antibacterial Activity. *Biochem. Pharmacol.* **2014**, 2 (4), 2177–2187.

(27) Hou, Y.; Feng, J.; Wang, Y.; Li, L. Enhanced Antibacterial Activity of Ag-Doped ZnO / Polyaniline Nanocomposites. *J. Mater. Sci: Mater. Electron.* **2016**, *27* (7), 6615–6622.

CHAPTER 7

BRIEF SUMMARY AND RESEARCH IMPACT

Research detailed in this thesis integrates experimental observations with state-of-the-art to understand on the molecular level ingredients that underlie on the photocatalytic phenol degradation on niobate, tantalate and its ion-exchanged compounds. With regard to the niobate and tantalate investigations research showed how 1) the successfully synthesis of pyrochlore, perovskite and layered-type structures by hydrothermal reaction, 2) the engineering of the pyrochlore material to enhance the photocatalytic, antibacterial and ionic conductivity applications. Chapter 3 presented research to show how the synthesis of pyrochlore, perovskite and layered type niobate compounds are tuned for their photocatalytic properties by intercalating, loading, doping with silver metals to the crystal structures. As our expectation that the silver metal incorporated samples would have the biggest positive impact on photocatalytic activity, the experimental results showed pyrochlore and perovskite-type silver incorporated samples with higher photocatalytic activity than their parent samples leading to a better photocatalytic materials. The broad impact of this study is, these photocatalytic materials can oxidized organic compounds to harmless product of CO_2 and H_2O, which could be

a promising method for environmental friendly waste water treatment. As compared with traditional water purification methods such as active carbon adsorption, chlorination, membrane filtration, iodination, chemical coagulation, ion-exchanged and ozone treatment, photocatalytic materials get great attention due to its low coast, safety, long effectivity and good stability. Moreover, other than the water purification, these photocatalytic materials can be used for water splitting and it can lead to other application such as hydrogen generation. Hydrogen can be used as a clean source of fuel to power transportation, power industrial, generate fertilizers in agricultural industry and also to power the domestic appliances. This can create energy security based on a hydrogen based economy.

Chapter 4 investigated the possibility in developing of photocatalytic activity in pyrochlore-type niobate and tantalate structures by silver metal cation ion-exchange. This ion-exchange reaction with excess molten $AgNO_3$ has proved to be a useful technique to change the physical properties of niobate and tantalate structures. The incorporation of the Ag^+ ion decreases the band gap energy from UV region to visible region with both niobate and tantalate compounds. Moreover, investigated the ionic conductivity of fluorite-type silver niobate and pyrochlore-type silver tantalate compounds. These two materials are new materials that were not

studied before for ionic conductivity. The impedance measurement of total conductivity, at 240 °C reached the order of 10^{-3} and 10^{-4} S/cm for tantalate and niobate, respectively. Moreover, ionic condouctiviy of solid electrolytes have gained a lot of attention recently due to their aplications in solid oxides fuel cell (SOFC), gas sensors, oxygen separation membrane, batteries and catalyst.

Research presented in chapter 5 and chapter 6 showed a novel way to tune the pyrochlore-type and perovskite-type structure to investigate the antibacterial activity. It is felt that this particular research may have a high future scientific impact. Over the last decade of antibacterial research, there have been no reports of antibacterial activity in pyrochlore-type niobate and tantalate compounds. To accomplish the antibacterial activity for the first time, a previous ion-exchanged method was used and silver ions were doped into the niobate and tantalate by small molar ratios and gradually increasing to obtain completely ion exchanged samples. These silver ion-exchanged samples exhibited remarkable antibacterial properties with respect to the parent compounds. The broad impact of this study is, these inorganic antibacterial materials have good safety, good stability, wide range of antibacterial activity and longtime activity compared to organic antibacterial agents. Therefore, these materials lead to a variety of applications such as, implantable

orthopedic biomaterials, bone replacements, building materials, cosmetics and treatment of burn wounds. Moreover, tunneled structure of pyrochlore-type materials given them controllable antibacterial capability and it can lead to further development of antimicrobial bioengineering applications.

In this thesis work three applications were mainly focused on; improving the photocatalytic activity of pyrochlore structure by incorporating silver ions, preparation of controllable antibacterial materials and preparation of ion conduction solid electrolyte. The engineering challenges to employ niobate and tantalate compounds as photocatalytic and antibacterial materials has to be evaluated and addressed. Thus, progressive approaches in the development of photocatalytic technologies can help enable water purification, energy production and storage by the energy harnessed by intermittent renewable energy resources such as solar. Lowering the cost of these technologies is of paramount importance and hydrothermal method would be a promising method for synthesis these samples. In this context pyrochlore-type niobate and tantalate catalysts can play a crucial role as a photocatalytic and antibacterial material.

CHAPTER 8

BUSINESS SENSE AND SOCIAL AWARENESS

Recycling of wastewater is recognized to be a sustainable way in water management to minimize water pollution. Most developing countries in the world face problems with water toxicity which can directly effect to the health of nature and present a threat to humans through contamination of drinking water supplies (e.g., surface and ground water). As a result, the polluted water contains bacteria, parasites and viruses which can cause life-threatening diseases like diarrhea, cholera and typhoid.

During my time as an undergraduate (University of Peradeniya, Sri Lanka) we were required to carry out a literature survey on the level and causes of pollution in a lake close to our University. In this survey I learned that microorganisms are on a rise due to the pollution in the water ways that feed the lake, moreover, the microbial activity had a long lasting impact on human and animal life around the lake. We also learned that the water that is supplied to the city comes from the lake we studied. Thus, the microbial activity in the lake was one of the major issues faced by the authorities when supplying consumable water. Moreover, chronic kidney disease with unusual characteristic spared around the north central and north eastern

boarder of the Sri Lanka due to the poor drinking water facility[1]. These water related problem influenced me to identify that there is so much more opportunity in the field of water purification that can be expanded in terms of ridding water of microorganisms to obtain purified drinking water. We made several proposals based on chemical principles to purify water, such as using antimicrobial agents to filter water that are made of cheap and earth abundant materials. Though this was just a proposal I always had the idea of working further at a research setting to develop materials with antimicrobial properties to help mitigate issues caused by microorganisms.

Thus, I have taken the Green Energy Conversion Science and Technology program. Here, I investigated the preparation of new oxide semiconductor materials

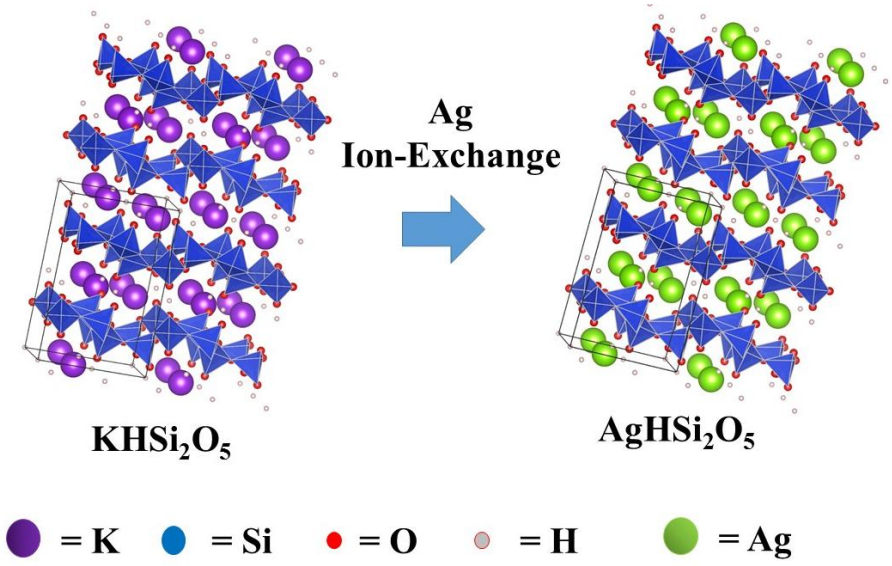

Figure 8.1: Crystal structure of $KHSi_2O_5$ and its ion-exchanged product $AgHSi_2O_5$

for water purification which suited my research interest. As I have explain in chapters 3, 4 and 5, I have used a hydrothermal preparation method to prepare niobate and tantalate compounds with various crystal structures such as pyrochlore-, perovskite-, layered-, or tunnel- type. I believe that the advance knowledge that I gained in my research work in water purification field, has laid a very good foundation for me to develop new techniques for my country. Thus, I have an idea to innovate filter papers

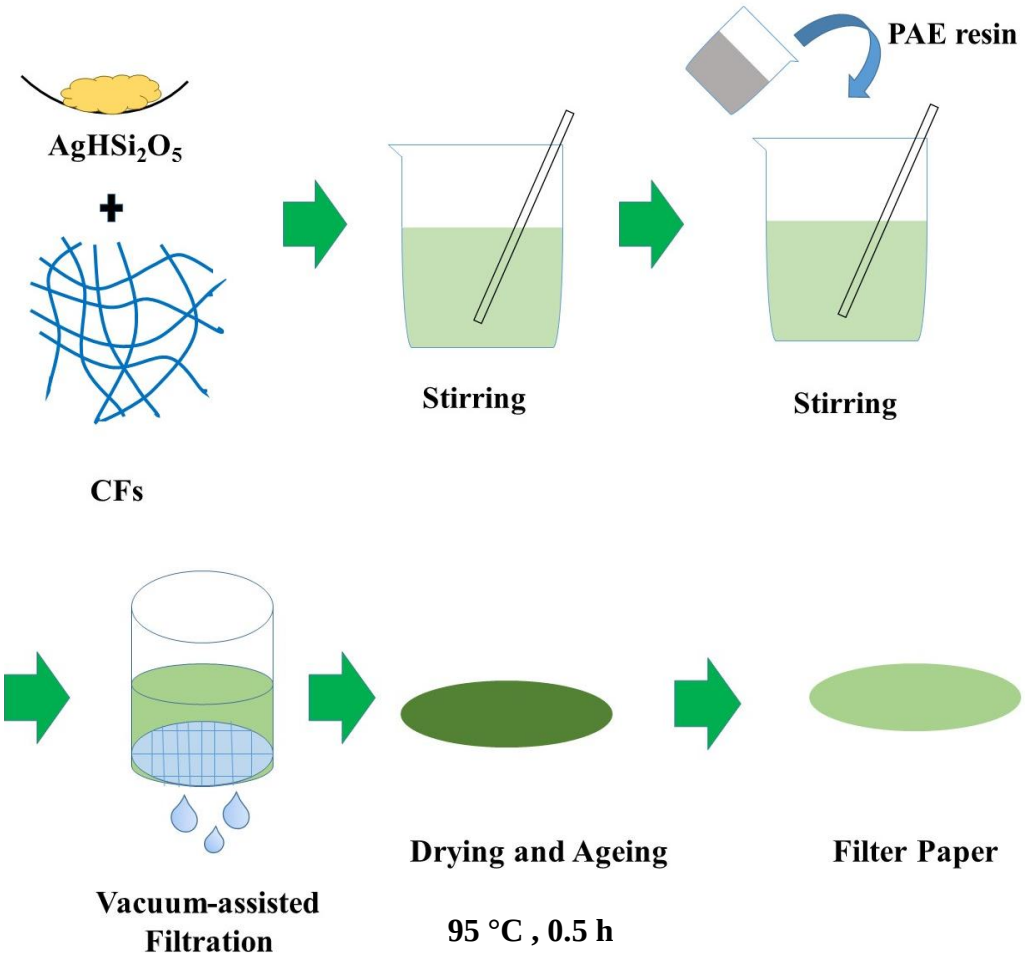

Figure 8.2: Schematic illustration of $AgHSi_2O_5$ / CF filter paper preparation.

for water purification which could be easily utilized for both rural villages and urban cities in Sri Lanka.

The niobate and tantalates compounds that I used in my research are quite expensive to be employed as low cost filter papers in developing countries. Thus, I hope to use potassium hydrogen silicate ($KHSi_2O_5$) as an alternative material, which has alkali metal-layered silicate structure that is somewhat similar with layered niobate structures. This orthorhombic $KHSi_2O_5$ which is incorporated with metals cations, will exhibits some important properties such as acidic, catalytic and oxidation properties of hydrocarbons. This compound can be easily synthesized using low temperature hydrothermal reactions and K^+ can be easily ion-exchanged or removed[2]. Therefore, in this situation, $KHSi_2O_5$ compound by will be obtained using a hydrothermal reaction and silver ions will be intercalated into layered hydro silicate structure by the ion-exchange method (Figure 8.1). Silicates are naturally occurring, abundant reserve in the environment which are ideal materials for preparation of low cost, high strength and highly efficient filter papers. Moreover, silver ion-exchanged into the layered silicate is toxic for bacterial cell and it's toxicity seems to be quite low for humans. Thus, low toxicity against mammalian cells is one of silver's greatest advantages over other medicinally relevant metals.

The plant cellulose fibers (CFs) is a great candidate for the preparation of environmentally friendly filter papers for water treatment since they have advantages such as low cost, high strength, biodegradability, sustainability and biocompatibility[3]. Therefore, I hope to design and fabricate silver hydrogen silicate/ cellulose fiber ($AgHSi_2O_5$ /CF) filter paper sheets with different silver weight ratio. This new $AgHSi_2O_5$/CF filter paper will be environmental friendly and cheap, specially suited for water purification applications. This process is capable of scaling-up production, which is promising for commercialization.

Figure 8.2 illustrates the process for the preparation of $AgHSi_2O_5$ /CF filter paper. First $AgHSi_2O_5$ powder and CFs will be uniformly mixed to obtain a stable aqueous pulp. Then the polyamidoamine-epichlorohydrin (PAE) resin will be use to increase the dry and wet strength of the filter paper. After vacuum filtration, aging will be performed at 95 °C for 0.5 hours to remove residual water from the filter paper. Cellulose fiber are the key raw material for paper manufacturing and wet strength agent such as PAE resin is a common additive in paper industry. Compared with other wet strength additives PAE has advantages such as small addition amount, nontoxicity, wide range of application and superior reinforcing effects[4].

To evaluate the water purification capability TiO_2 nanoparticle (250 ppm) with average partial size 40 nm will be used for filtration experiments for 4 hours. The rejection rate of the TiO_2 nanoparticle during the experimental period will be evaluate by the high performance liquid chromatography (HPLC). To further investigation filter paper will be used for the bacteria rejection experiments. In this experiment number of bacteria colonies trap on the surface of filter paper will be evaluated by colony counting method. To the further clarification adsorption performance of the filter paper will be evaluated by methyl blue filtration experiments. As shown in Figure 8.3 $AgHSi_2O_5$ / CF filter paper has porous structure with cellulose fiber. This porosity and $AgHSi_2O_5$ increase the water purification trapping particles and bacteria in water.

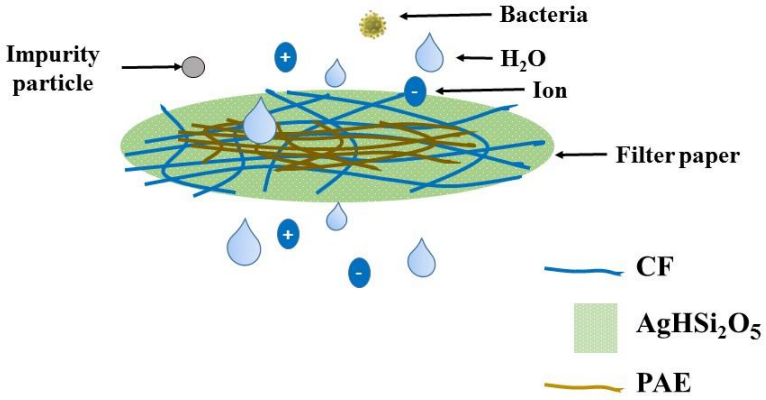

Figure 8.3: Schematic illustration of structure and filtration process of the prepared $AgHSi_2O_5$/CF filter paper.

The simple calculation can be used to estimate the total cost and lifetime of a filter paper. If a filter paper prepared by initial raw materials of KOH, Si_2O_5, $AgNO_3$, PAE and CF, the material and preparation cost assume to be 1084 Yen. Assuming the filter paper could be filtrate 100 L volume of water each day and thus would only cost 10.84 Yen per liter of treated water. The compare with current retail price of 1 L water in japan (200 Yen), making this is the least expensive water purification method on the market. The current estimated price of the filter paper can be reduce with the mass production. The filter papers are easy to transport because

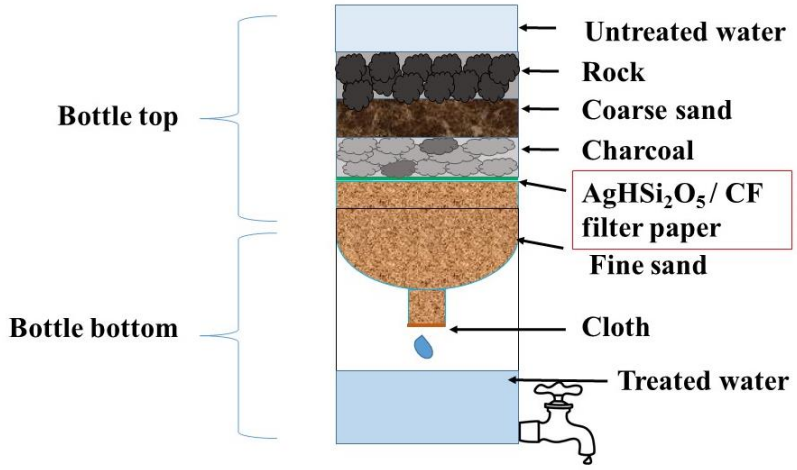

Figure 8.4: Schematic illustration of home-made filtration device

of their small size and durability, which we believe will make them more engaging to local and rural area. Furthermore, using this filter paper villagers can build home-made water purification and filtration device as shown in Figure 8.4. This filter paper

will be shown to efficiently remove all type of pathogens, dyes and impurity particles. Therefore, this could reduce several societal problems in the access to safe drinking water in Sri Lanka and other areas with high population densities and poor access to pure water. Moreover, this innovation can be extended to create ceramic tablets, when drop into house hold water storage containers, can control or disinfect microbial pathogens. Finally, I believe this new innovation shows great potential to provide safe drinking water for developing countries such as Sri Lanka.

8.1 References

(1) Jayasumana, C.; Paranagama, P.; Agampodi, S.; Wijewardane, C.; Gunatilake, S. Drinking Well Water and Occupational Exposure to Herbicides Is Associated with Chronic Kidney Disease, in Padavi-Sripura , Sri Lanka. *Environ. Health.*, **2015**, 14, 1–10.

(2) Schmidmari, D.; Kahlenberg, V.; Perfler, L, A. Structural , Spectroscopic and Computational Studies on the Monoclinic Polymorph (Form I) of Potassium Hydrogen disilicates ($KHSi_2O_5$). *Mineral. Mag.*, **2014**, 78, 609–622.

(3) Jain, S.; Bhanjana, G.; Heydarifard, S.; Dilbaghi, N.; Nazhad, M. M. Enhanced Antibacterial pro Fi Le of Nanoparticle Impregnated Cellulose Foam Fi Lter Paper for Drinking Water Fi Ltration. *Carbohydr. Polym.*, **2018**, *202*, 219–226.

(4) Zhang, Q.; Zhu, Y.; Wu, J.; Shao, Y.; Cai, A. Ultralong Hydroxyapatite Nanowire-Based Filter Paper for High- Performance Water Purification., *ACS Appl. Mater. Interfaces.*, **2019**, 11, 4288-4301.

List of Publications

Papers

1. "Synthesis and crystal structure of pyrochlore-type silver niobate and tantalate", **Isuru Withanage,** Nobuhiro Kumada, Takahiro Takei, Sayaka Yanagida, Yoshihiro Kuroiwa and Chikako Moriyoshi, *J. Ceram. Soc. Jpn.* 125 [10], 776-778, 2017.

2. "Hydrothermal doping of Ag into three types of potassium niobates", **W.I.U Withanage**, Sayaka Yanagida, Takahiro Takei and Nobuhiro Kumada, *J. Ceram. Soc. Jpn.* 126 [10], 784-788, 2018.

3. "Hydrothermal reaction of $NaBiO_3 \cdot nH_2O$ with transition-metal (Co,Ni,Cu) salts", Yo Yamamoto, **W.I.U. Withanage**, Takahiro Takei, Sayaka Yanagida, Nobuhiro Kumada and Hisanori Yamane, *J. Ceram. Soc. Jpn.* 126 [12], 1005-1012, 2018.

4. "Electrical properties of pyrochlore-type silver tantalate and fluorite-type silver niobate", **W.I.U Withanage,** Nobuhiro Kumada, Takahiro Takei, Sayaka Yanagida, Kiyoharu Tadanaga, Akira Miura, N. C. R. Navarro, Masaki Azuma, *J. Ceram. Soc. Jpn.* 128 [1], 46-50, 2020.

List of Conference Presentations

Oral presentation

1. "Preparation and characterization of pyrochlore-type $AgMO_3$ (M=Nb, Ta)", **Isuru Withanage**, Nobuhiro Kumada, Takahiro Takei, Sayaka Yanagida, The 55th Ceramic basic science conference, January 13th 2017, Okayama, Japan.

2. "Transition metal doping into potassium niobate and tantalates by hydrothermal reaction". **Isuru Withanage**, N. Kumada, S. Yanagida, T. Takei, The 56th Symposium on basic science of ceramics, January 11th -12th, 2018, International conference hall, Tsukuba, Japan.

3. "Hydrothermal incorporation of silver into three types of potassium niobates and their photocatalytic properties". **I. Withanage**, N. Kumada, T. Takei, S.

Yanagida, The 7th international seminar for special doctoral program "Green energy conversion science and technology", August 22, 2018, University of Yamanashi, Kofu, Japan.

Poster presentations

4. "Preparation and crystal structure analysis of pyrochlore-type oxides", **Isuru Withanage**, Nobuhiro Kumada, Takahiro Takei, Sayaka Yanagida, The 5th international seminar for special doctoral program "Green energy conversion science and technology", August 31st 2016, Koumi-Nagano, Japan.

5. "Synthesis and crystal structure of pyrochlore-type silver niobate and tantalate", **Isuru Withanage**, Nobuhiro Kumada, Takahiro Takei, Sayaka Yanagida, The 6th JACI/GSC Symposium, July 3rd-4th, 2017, Tokyo international forum, Tokyo, Japan.

6. "Preparation and photocatalytic properties of pyrochlore-type $AgMO_3$ (M=Nb, Ta)", **Isuru Withanage**, Nobuhiro Kumada, Sayaka Yanagida, Takahiro Takei, 15th Conference and exhibition of the European ceramic society, July 9th -13th, 2017, Budapest, Hungary.

7. "Preparation and photocatalytic activity of new pyrochlore and perovskite-type structure", **Isuru Withanage**, Nobuhiro Kumada, Takahiro Takei, Sayaka Yanagida The 6th international seminar for special doctoral program "Green energy conversion science and technology", September 13th, 2017, Koumi-Nagano,Japan.

8. "Synthesis and crystal structure of pyrochlore-type silver niobate and tantalate", **Isuru Withanage**, Nobuhiro Kumada, Takahiro Takei, Sayaka Yanagida, The 10th International conference on the science and technology for advanced ceramics (STAC-10), August 1st -3rd, 2017, Mielparque-Yokohama, Japan.

9. "Hydrothermal doping of transition metals into potassium niobate", **Isuru Withanage,** Nobuhiro Kumada, Takahiro Takei, Sayaka Yanagida, The 30th fall symposium of the ceramics society of japan, September 20th 2017, Kobe University, Japan

10. "Transition metal doping into potassium niobate by hydrothermal reaction" **Isuru Withanage**, Nobuhiro Kumada, Sayaka Yanagida, Takahiro Takei, 6th

International solvothermal and hydrothermal association conference (ISHA), August 8th -12th , 2018, Tohoku University, Sendai, Japan.

11. "Preparation and photocatalytic properties of potassium niobates". **Isuru Withanage**, Nobuhiro Kumada, Sayaka Yanagida, Takahiro Takei, 7th International conference on ion exchange (ICIE), September 10th -13th, 2018, University of Gadjah Mada, Yogyakarta, Indonesia.

12. "Hydrothermal Incorporation of Silver into Three Type of Potassium Niobate". **W.I.U Withanage**, Nobuhiro Kumada, Sayaka Yanagida, Takahiro Takei, MRS fall meeting, November 25th-30th, 2018, Boston Massachusetts, USA.

13. "Antibacterial properties of silver niobates and silver tantalate"**, I. Withanage,** N. Kumada, T. Takei, S. Yanagida, M. Ueda, A. Mamoru, The 8th international seminar for special doctoral program "Green energy conversion science and technology", October 24th, 2019, University of Yamanashi, Kofu, Japan.

14. "Antibacterial and photocatalytic properties of silver niobate and silver tantalate", **I. Withanage**, N. Kumada, T. Takei, S. Yanagida, M. Ueda, A. Mamoru, The 13th Pacific Rim conference of ceramic society (PACRIM13), November 27th, 2019, Okinawa, Japan.

15. "Antibacterial properties silver ion-exchanged niobate, tantalate and silicate", **I. Withanage**, N. Kumada, T. Takei, S. Yanagida, M. Ueda, A. Mamoru, The 9th JACI/GSC Symposium, September, 10th, 2020, Online.